



**Calhoun: The NPS Institutional Archive**  
**DSpace Repository**

---

Theses and Dissertations

1. Thesis and Dissertation Collection, all items

---

2022-12

# UNSCENTED GUIDANCE FOR POINT-TO-POINT REACTION WHEEL MANEUVERS

Magallanes, Lara C.

Monterey, CA; Naval Postgraduate School

---

<https://hdl.handle.net/10945/71501>

---

This publication is a work of the U.S. Government as defined in Title 17, United States Code, Section 101. Copyright protection is not available for this work in the United States.

*Downloaded from NPS Archive: Calhoun*



<http://www.nps.edu/library>

Calhoun is the Naval Postgraduate School's public access digital repository for research materials and institutional publications created by the NPS community. Calhoun is named for Professor of Mathematics Guy K. Calhoun, NPS's first appointed -- and published -- scholarly author.

**Dudley Knox Library / Naval Postgraduate School**  
**411 Dyer Road / 1 University Circle**  
**Monterey, California USA 93943**



# NAVAL POSTGRADUATE SCHOOL

MONTEREY, CALIFORNIA

## DISSERTATION

### UNSCENTED GUIDANCE FOR POINT-TO-POINT REACTION WHEEL MANEUVERS

by

Lara C. Magallanes

December 2022

Dissertation Supervisor:

Mark Karpenko

**Approved for public release. Distribution is unlimited.**

THIS PAGE INTENTIONALLY LEFT BLANK

|  |   |  |   |  |
|--|---|--|---|--|
| <b>REPORT DOCUMENTATION PAGE</b>   |   |  | <i>Form Approved OMB<br/>No. 0704-0188</i>                      |  |
| Public reporting burden for this collection of information is estimated to average 1 hour per response, including the time for reviewing instruction, searching existing data sources, gathering and maintaining the data needed, and completing and reviewing the collection of information. Send comments regarding this burden estimate or any other aspect of this collection of information, including suggestions for reducing this burden, to Washington headquarters Services, Directorate for Information Operations and Reports, 1215 Jefferson Davis Highway, Suite 1204, Arlington, VA 22202-4302, and to the Office of Management and Budget, Paperwork Reduction Project (0704-0188) Washington, DC 20503.   |   |  |   |  |
| <b>1. AGENCY USE ONLY<br/>(Leave blank)</b>  |   | <b>2. REPORT DATE</b><br>December 2022                                 | <b>3. REPORT TYPE AND DATES COVERED</b><br>Dissertation         |  |
| <b>4. TITLE AND SUBTITLE</b><br>UNSCENTED GUIDANCE FOR POINT-TO-POINT<br>REACTION WHEEL MANEUVERS  |   |  | <b>5. FUNDING NUMBERS</b><br><br>RMMY7; RMMY6                   |  |
| <b>6. AUTHOR(S)</b> Lara C. Magallanes   |   |  |   |  |
| <b>7. PERFORMING ORGANIZATION NAME(S) AND ADDRESS(ES)</b><br>Naval Postgraduate School<br>Monterey, CA 93943-5000  |   |  | <b>8. PERFORMING<br/>ORGANIZATION REPORT<br/>NUMBER</b>         |  |
| <b>9. SPONSORING / MONITORING AGENCY NAME(S) AND<br/>ADDRESS(ES)</b><br>DOD Space, Chantilly, VA 20151   |   |  | <b>10. SPONSORING /<br/>MONITORING AGENCY<br/>REPORT NUMBER</b> |  |
| <b>11. SUPPLEMENTARY NOTES</b> The views expressed in this thesis are those of the author and do not reflect the official policy or position of the Department of Defense or the U.S. Government.  |   |  |   |  |
| <b>12a. DISTRIBUTION / AVAILABILITY STATEMENT</b><br>Approved for public release. Distribution is unlimited.   |   |  | <b>12b. DISTRIBUTION CODE</b><br>A                              |  |
| <b>13. ABSTRACT (maximum 200 words)</b><br><br>Attitude control system failures are often mission ending even when the mission payload remains operational. In this dissertation, the concept of unscented guidance is applied to reorient a reaction wheel satellite in the absence of feedback from star trackers or an inertial measurement unit (IMU). It is shown that an open-loop maneuver, properly designed using optimal control theory, can be used to achieve terminal attitude errors that are comparable with closed-loop control in the presence of uncertainty in the satellite inertia tensor. Typically, coarse closed-loop control is used to achieve < 1 degree pointing accuracy before more accurate pointing is done using fine guidance sensors to close the loop for science acquisition. It is shown that reaction wheel maneuvers designed using unscented guidance can also achieve sub-degree pointing accuracy of the spacecraft, making control hand-off to a functioning fine pointing control mode possible. The approach presented here enables large angle attitude control to be recovered so that mission operations may be continued despite IMU or star tracker failures. |   |  |   |  |
| <b>14. SUBJECT TERMS</b><br>unscented guidance, optimal control, zero-feedback slew, open-loop control, optimum momentum bias, terminal pointing error minimization, large angle zero-feedback slew maneuver   |   |  | <b>15. NUMBER OF<br/>PAGES</b><br>189                           |  |
|  |   |  | <b>16. PRICE CODE</b>   |  |
| <b>17. SECURITY<br/>CLASSIFICATION OF<br/>REPORT</b><br>Unclassified   | <b>18. SECURITY<br/>CLASSIFICATION OF THIS<br/>PAGE</b><br>Unclassified | <b>19. SECURITY<br/>CLASSIFICATION OF<br/>ABSTRACT</b><br>Unclassified | <b>20. LIMITATION OF<br/>ABSTRACT</b><br><br>UU                 |  |

NSN 7540-01-280-5500

Standard Form 298 (Rev. 2-89)  
Prescribed by ANSI Std. Z39-18



THIS PAGE INTENTIONALLY LEFT BLANK

**Approved for public release. Distribution is unlimited.**

**UNSCENTED GUIDANCE FOR POINT-TO-POINT REACTION WHEEL  
MANEUVERS**

Lara C. Magallanes  
Civilian, Department of the Navy  
BS, University of Colorado, Boulder, 1996  
MS, University of Colorado, Boulder, 1998

Submitted in partial fulfillment of the  
requirements for the degree of

**DOCTOR OF PHILOSOPHY IN ASTRONAUTICAL ENGINEERING**

from the

**NAVAL POSTGRADUATE SCHOOL  
December 2022**

|              |  |   |
|--------------|--|---|
| Approved by: | Isaac M. Ross<br>Department of Mechanical and<br>Aerospace Engineering<br>Dissertation Chair | Mark Karpenko<br>Department of Mechanical and<br>Aerospace Engineering<br>Dissertation Supervisor |
|              | Francis X. Giraldo<br>Department of<br>Applied Mathematics                                   | Isaac I. Kaminer<br>Department of Mechanical and<br>Aerospace Engineering                         |
|              | James H. Newman<br>Space Systems Academic Group  |   |
| Approved by: | Brian S. Bingham<br>Chair, Department of Mechanical and Aerospace Engineering                |   |
|              | Joseph P. Hooper<br>Vice Provost of Academic Affairs   |   |

THIS PAGE INTENTIONALLY LEFT BLANK

## ABSTRACT

Attitude control system failures are often mission ending even when the mission payload remains operational. In this dissertation, the concept of unscented guidance is applied to reorient a reaction wheel satellite in the absence of feedback from star trackers or an inertial measurement unit (IMU). It is shown that an open-loop maneuver, properly designed using optimal control theory, can be used to achieve terminal attitude errors that are comparable with closed-loop control in the presence of uncertainty in the satellite inertia tensor. Typically, coarse closed-loop control is used to achieve  $< 1$  degree pointing accuracy before more accurate pointing is done using fine guidance sensors to close the loop for science acquisition. It is shown that reaction wheel maneuvers designed using unscented guidance can also achieve sub-degree pointing accuracy of the spacecraft, making control hand-off to a functioning fine pointing control mode possible. The approach presented here enables large angle attitude control to be recovered so that mission operations may be continued despite IMU or star tracker failures.

THIS PAGE INTENTIONALLY LEFT BLANK

# TABLE OF CONTENTS

|             |   |           |
|-------------|---|-----------|
| <b>I.</b>   | <b>INTRODUCTION.....</b>  | <b>1</b>  |
| <b>A.</b>   | <b>MOTIVATION .....</b>   | <b>1</b>  |
| <b>B.</b>   | <b>BACKGROUND .....</b>   | <b>3</b>  |
|             | 1. Attitude Control .....   | 4         |
|             | 2. Momentum Storage .....   | 6         |
|             | 3. Representative Spacecraft.....   | 7         |
|             | 4. ADCS Components .....  | 10        |
|             | 5. Representative Problem .....   | 11        |
|             | 6. Gyroless Attitude Control: Closed-Loop .....                               | 13        |
|             | 7. Gyroless Attitude Control: Open-Loop .....                                 | 19        |
| <b>C.</b>   | <b>CONTRIBUTIONS OF THIS DISSERTATION .....</b>                               | <b>21</b> |
| <b>D.</b>   | <b>DISSERTATION OUTLINE .....</b>   | <b>22</b> |
| <b>II.</b>  | <b>OPTIMAL CONTROL BACKGROUND.....</b>  | <b>25</b> |
| <b>A.</b>   | <b>DETERMINISTIC ZERMELO MINIMUM-TIME PROBLEM.....</b>                        | <b>27</b> |
| <b>B.</b>   | <b>OPTIMAL CONTROL WITH UNCERTAIN PARAMETERS.....</b>                         | <b>39</b> |
|             | 1. Introduction to Optimal Control with Parameter<br>Uncertainty .....        | 40        |
|             | 2. Semi-Discrete Lebesgue-Stieltjes .....                                     | 42        |
|             | 3. Monte Carlo Sampling .....   | 43        |
|             | 4. Multidimensional Approximation Sampling.....                               | 44        |
|             | 5. Unscented Sampling.....  | 45        |
|             | 6. A Semi-Discrete Lebesgue-Stieltjes Zermelo Problem.....                    | 46        |
|             | 7. Dissertation Use of Unscented Guidance Method.....                         | 66        |
| <b>C.</b>   | <b>CHAPTER SUMMARY.....</b>   | <b>66</b> |
| <b>III.</b> | <b>CONVENTIONAL REACTION-WHEEL ATTITUDE CONTROL .....</b>                     | <b>69</b> |
| <b>A.</b>   | <b>REPRESENTATIVE SPACECRAFT .....</b>  | <b>69</b> |
| <b>B.</b>   | <b>SPACECRAFT ATTITUDE KINEMATICS.....</b>                                    | <b>70</b> |
| <b>C.</b>   | <b>CLOSED-LOOP EQUATIONS OF MOTION.....</b>                                   | <b>71</b> |
|             | 1. Satellite Equations of Motion.....   | 71        |
|             | 2. Quaternion Error Feedback .....  | 74        |
| <b>D.</b>   | <b>EXAMPLE CLOSED-LOOP MANEUVER.....</b>                                      | <b>77</b> |
| <b>E.</b>   | <b>OPEN-LOOP KINEMATIC MANEUVER PROFILE .....</b>                             | <b>79</b> |
| <b>F.</b>   | <b>OPEN-LOOP KINEMATIC MANEUVER: SINGLE-AXIS<br/>INERTIA UNCERTAINTY.....</b> | <b>82</b> |

|     |  |     |
|-----|--|-----|
| G.  | OPEN-LOOP KINEMATIC MANEUVER: THREE-AXIS<br>INERTIA UNCERTAINTY..... | 85  |
| H.  | CHAPTER SUMMARY.....   | 88  |
| IV. | FORMULATION OF UNSCENTED REACTION WHEEL<br>MANEUVER PROBLEM.....     | 91  |
| A.  | COST FUNCTIONAL DEFINITION.....                                      | 91  |
| B.  | UNSCENTED REACTION WHEEL MANEUVER COST<br>FUNCTIONAL.....            | 92  |
| C.  | NECESSARY CONDITIONS FOR ARBITRARY<br>MOMENTUM BIAS.....             | 95  |
| D.  | NECESSARY CONDITIONS FOR OPTIMUM MOMENTUM<br>BIAS .....              | 106 |
| E.  | CHAPTER SUMMARY.....   | 112 |
| V.  | UNSCENTED REACTION WHEEL ATTITUDE MANEUVERS .....                    | 115 |
| A.  | ARBITRARY MOMENTUM BIAS SOLUTIONS .....                              | 115 |
| 1.  | Single-Axis Inertia Uncertainty .....                                | 115 |
| 2.  | Three-Axis Inertia Uncertainty .....                                 | 124 |
| B.  | OPTIMUM MOMENTUM BIAS SOLUTIONS .....                                | 128 |
| 1.  | Single-Axis Inertia Uncertainty .....                                | 128 |
| 2.  | Three-Axis Inertia Uncertainty .....                                 | 134 |
| C.  | SUMMARY OF RESULTS .....   | 139 |
| D.  | CHAPTER SUMMARY.....   | 140 |
| VI. | CONCLUSIONS AND FUTURE WORK.....                                     | 143 |
|     | LIST OF REFERENCES .....   | 145 |
|     | INITIAL DISTRIBUTION LIST .....                                      | 167 |

## LIST OF FIGURES

|            |  |    |
|------------|--|----|
| Figure 1.  | Solution of the Deterministic Zermelo Problem: Optimal Control Versus Time .....                                     | 34 |
| Figure 2.  | Solution of the Deterministic Zermelo Problem: Optimal Position $y$ Versus $x$ .....                                 | 35 |
| Figure 3.  | Solution of the Deterministic Zermelo Problem: Optimal Hamiltonian Versus Time .....                                 | 36 |
| Figure 4.  | Solution of the Deterministic Zermelo Problem: Optimal Control $u_1$ and Co-State $\lambda_x$ Pair Versus Time ..... | 37 |
| Figure 5.  | Solution of the Deterministic Zermelo Problem: Optimal Control $u_2$ and Co-State $\lambda_y$ Pair Versus Time ..... | 37 |
| Figure 6.  | Solution of the Deterministic Zermelo Problem: Optimal Path Co-Vector Versus Time .....                              | 38 |
| Figure 7.  | Solution of the Deterministic Zermelo Problem: Constraint Path Versus Time .....                                     | 38 |
| Figure 8.  | Solution of the Deterministic Zermelo Problem: Propagation Test $y$ Versus $x$ .....                                 | 39 |
| Figure 9.  | Solution of the Uncertain Zermelo Problem: Optimal Control Versus Time .....   | 60 |
| Figure 10. | Solution of the Uncertain Zermelo Problem: Optimal Position $y$ Versus $x$ .....                                     | 60 |
| Figure 11. | Solution of the Uncertain Zermelo Problem: Optimal Hamiltonian Versus Time .....                                     | 61 |
| Figure 12. | Solution of the Uncertain Zermelo Problem: Optimal Control $u_1$ and Co-States $\lambda_x$ Pair Versus Time .....    | 62 |
| Figure 13. | Solution of the Uncertain Zermelo Problem: Optimal Control $u_2$ and Co-States $\lambda_y$ Pair Versus Time .....    | 62 |
| Figure 14. | Solution of the Uncertain Zermelo Problem: Optimal Path Co-Vector Versus Time .....                                  | 63 |
| Figure 15. | Solution of the Uncertain Zermelo Problem: Constraint Path Versus Time .....   | 63 |



|            |  |    |
|------------|--|----|
| Figure 16. | Solution of the Uncertain Zermelo Problem: Propagation Test $y$ Versus $x$ Using $N=10$ Monte Carlo Runs ..... | 64 |
| Figure 17. | Solution of the Uncertain Zermelo problem: $N=1000$ Monte Carlo Simulation of Target Error Distribution .....  | 65 |
| Figure 18. | Block Diagram of Closed-loop Quaternion Error Feedback Attitude Control System.....                            | 74 |
| Figure 19. | Simulation of Closed-Loop Maneuver Angle Error .....   | 78 |
| Figure 20. | Simulation of Closed-Loop Maneuver Angular Rate in the Body-Frame .....  | 79 |
| Figure 21. | Simulation of Closed-Loop Maneuver Momentum in the Body-Frame .....  | 79 |
| Figure 22. | Block Diagram of Open-Loop Attitude Control System .....   | 80 |
| Figure 23. | Open-Loop Profile of Maneuver Rotation Acceleration .....  | 81 |
| Figure 24. | Open-Loop Profile of Maneuver Rotation Rate.....   | 81 |
| Figure 25. | Open-Loop Profile of Maneuver Rotation Angle .....   | 82 |
| Figure 26. | Open-Loop Kinematic Maneuver Angle Error .....   | 84 |
| Figure 27. | Open-Loop Kinematic Maneuver Body-Frame Angular Rate.....  | 84 |
| Figure 28. | Open-Loop Kinematic Maneuver Body-Frame Spacecraft Momentum.....   | 85 |
| Figure 29. | Monte Carlo Simulation Results of Open-Loop Kinematic Slew: Terminal Pointing Errors .....                     | 85 |
| Figure 30. | Open-Loop Reaction Wheel Torque Kinematic Maneuver for Three-Axis Uncertainty .....                            | 86 |
| Figure 31. | Open-Loop Kinematic Maneuver for Three-Axis Uncertainty Angle Error .....                                      | 87 |
| Figure 32. | Open-Loop Kinematic Maneuver for Three-Axis Uncertainty Body-Frame Angular Rate.....                           | 87 |
| Figure 33. | Open-Loop Kinematic Maneuver for Three-Axis Uncertainty Body-Frame Spacecraft Momentum.....                    | 88 |

|            |  |     |
|------------|--|-----|
| Figure 34. | Unscented Reaction Wheel Maneuver Single-Axis Uncertainty<br>Angle Error with Arbitrary Momentum Bias.....   | 118 |
| Figure 35. | Unscented Reaction Wheel Maneuver Single-Axis Uncertainty<br>Body-Frame Angular Rate with Arbitrary Momentum Bias .....  | 118 |
| Figure 36. | Unscented Reaction Wheel Maneuver Single-Axis Uncertainty<br>Body-Frame Reaction Wheel Momentum with Arbitrary Momentum<br>Bias .....                              | 119 |
| Figure 37. | Monte Carlo Simulation Results of Unscented Reaction Wheel<br>Maneuver Arbitrary Momentum Bias with Single-Axis Uncertainty:<br>Terminal Pointing Errors .....     | 120 |
| Figure 38. | Solution of the Unscented Reaction Wheel Maneuver Arbitrary<br>Momentum Bias Problem with Single-Axis Uncertainty: Optimal<br>Control Versus Time.....             | 121 |
| Figure 39. | Solution of the Unscented Reaction Wheel Maneuver Arbitrary<br>Momentum Bias Problem with Single-Axis Uncertainty: Optimal<br>Hamiltonian Versus Time .....        | 121 |
| Figure 40. | Solution of the Unscented Reaction Wheel Maneuver Arbitrary<br>Momentum Bias Problem with Single-Axis Uncertainty: Co-States<br>$\lambda_q$ Versus Time.....       | 122 |
| Figure 41. | Solution of the Unscented Reaction Wheel Maneuver Arbitrary<br>Momentum Bias Problem with Single-Axis Uncertainty: Co-States<br>$\lambda_\omega$ Versus Time ..... | 122 |
| Figure 42. | Solution of the Unscented Reaction Wheel Maneuver Arbitrary<br>Momentum Bias Problem with Single-Axis Uncertainty: Co-States<br>$\lambda_h$ Versus Time.....       | 123 |
| Figure 43. | Solution of the Unscented Reaction Wheel Maneuver Arbitrary<br>Momentum Bias Problem with Single-Axis Uncertainty:<br>Conservation of Angular Momentum .....       | 124 |
| Figure 44. | Unscented Reaction Wheel Maneuver Three-Axis Uncertainty Angle<br>Error with Arbitrary Momentum Bias .....   | 125 |
| Figure 45. | Unscented Reaction Wheel Maneuver Three-Axis Uncertainty Body-<br>Frame Angular Rate with Arbitrary Momentum Bias .....  | 125 |
| Figure 46. | Unscented Reaction Wheel Maneuver Three-Axis Uncertainty Body-<br>Frame Reaction Wheel Momentum with Arbitrary Momentum Bias .....                                 | 126 |

|            |  |     |
|------------|--|-----|
| Figure 47. | Monte Carlo Simulation Results of Unscented Reaction Wheel<br>Maneuver Arbitrary Momentum Bias with Three-Axis Uncertainty:<br>Terminal Pointing Errors .....  | 126 |
| Figure 48. | Solution of the Unscented Reaction Wheel Maneuver Arbitrary<br>Momentum Bias Problem with Three-Axis Uncertainty: Optimal<br>Control Versus Time.....          | 127 |
| Figure 49. | Solution of the Unscented Reaction Wheel Maneuver Arbitrary<br>Momentum Bias Problem with Three-Axis Uncertainty: Optimal<br>Hamiltonian Versus Time .....     | 127 |
| Figure 50. | Solution of the Unscented Reaction Wheel Maneuver Arbitrary<br>Momentum Bias Problem with Three-Axis Uncertainty:<br>Conservation of Angular Momentum .....    | 128 |
| Figure 51. | Unscented Reaction Wheel Maneuver Single-Axis Uncertainty<br>Angle Error with Optimum Momentum Bias .....  | 130 |
| Figure 52. | Unscented Reaction Wheel Maneuver Single-Axis Uncertainty<br>Body-Frame Angular Rate with Optimum Momentum Bias.....   | 130 |
| Figure 53. | Unscented Reaction Wheel Maneuver Single-Axis Uncertainty<br>Body-Frame Reaction Wheel Momentum with Optimum Momentum<br>Bias .....                            | 131 |
| Figure 54. | Monte Carlo Simulation Results of Unscented Reaction Wheel<br>Maneuver Arbitrary Momentum Bias with Single-Axis Uncertainty:<br>Terminal Pointing Errors ..... | 131 |
| Figure 55. | Monte Carlo Simulation Results of Unscented Reaction Wheel<br>Maneuver Optimum Momentum Bias with Single-Axis Uncertainty:<br>Terminal Pointing Errors .....   | 132 |
| Figure 56. | Solution of the Unscented Reaction Wheel Maneuver Optimum<br>Momentum Bias Problem with Single-Axis Uncertainty: Optimal<br>Control Versus Time.....           | 133 |
| Figure 57. | Solution of the Unscented Reaction Wheel Maneuver Optimum<br>Momentum Bias Problem with Single-Axis Uncertainty: Optimal<br>Hamiltonian Versus Time .....      | 133 |
| Figure 58. | Solution of the Unscented Reaction Wheel Maneuver Optimum<br>Momentum Bias Problem with Single-Axis Uncertainty: Co-States<br>$\lambda_h$ Versus Time.....     | 134 |

|            |   |     |
|------------|---|-----|
| Figure 59. | Unscented Reaction Wheel Maneuver Three-Axis Uncertainty Angle Error with Optimum Momentum Bias.....  | 135 |
| Figure 60. | Unscented Reaction Wheel Maneuver Three-Axis Uncertainty Body-Frame Angular Rate with Optimum Momentum Bias.....  | 136 |
| Figure 61. | Unscented Reaction Wheel Maneuver Three-Axis Uncertainty Body-Frame Reaction Wheel Momentum with Optimum Momentum Bias.....                             | 136 |
| Figure 62. | Monte Carlo Simulation Results of Unscented Reaction Wheel Maneuver Arbitrary Momentum Bias with Three-Axis Uncertainty: Terminal Pointing Errors ..... | 137 |
| Figure 63. | Monte Carlo Simulation Results of Unscented Reaction Wheel Maneuver Optimum Momentum Bias with Three-Axis Uncertainty: Terminal Pointing Errors .....   | 137 |
| Figure 64. | Solution of the Unscented Reaction Wheel Maneuver Optimum Momentum Bias Problem with Three-Axis Uncertainty: Optimal Control Versus Time.....           | 138 |
| Figure 65. | Solution of the Unscented Reaction Wheel Maneuver Optimum Momentum Bias Problem with Three-Axis Uncertainty: Optimal Hamiltonian Versus Time .....      | 138 |

THIS PAGE INTENTIONALLY LEFT BLANK

## LIST OF TABLES

|          |   |     |
|----------|---|-----|
| Table 1. | ADCS Sensor and Actuator Combinations for Spacecraft Similar to the Representative Spacecraft ..... | 9   |
| Table 2. | $Z_D$ and $Z_{N=4}$ Monte Carlo Error and Standard Deviation Results .....                          | 65  |
| Table 3. | Spacecraft Parameters Used in This Dissertation .....   | 70  |
| Table 4. | Statistical Performance of Unscented Reaction Wheel Maneuvering .....                               | 140 |

THIS PAGE INTENTIONALLY LEFT BLANK

## LIST OF ACRONYMS AND ABBREVIATIONS

|        |  |
|--------|--|
| 1D     | One-dimensional                              |
| 2D     | Two-dimensional                              |
| 3D     | Three-dimensional                            |
| ADCS   | Attitude Determination and Control System    |
| APS    | Active Pixel Sensor                          |
| C&DH   | Command and Data Handling                    |
| CDF    | Cumulative Distribution Function             |
| CMG    | Control Moment Gyro                          |
| CMOS   | Complementary Metal Oxide Semiconductor      |
| CSS    | Coarse Sun Sensor                            |
| DOF    | Degree of Freedom                            |
| EoM    | End of Mission                               |
| FES    | Fine Error Sensor                            |
| FGS    | Fine Guidance Sensor                         |
| FSS    | Fine Sun Sensor                              |
| FUSE   | Far-Ultraviolet Spectroscopic Explorer       |
| GE     | General Electric                             |
| GenOC  | Generalized Optimal Control                  |
| GPS    | Global Positioning System                    |
| GSFC   | Goddard Space Flight Center                  |
| HST    | Hubble Space Telescope                       |
| ICBM   | Inter-Continental Ballistic Missile          |
| IMU    | Inertial Measurement Unit                    |
| IRU    | Inertial Reference Unit                      |
| IUE    | International Ultraviolet Explorer           |
| JHUAPL | Johns Hopkins University Applied Physics Lab |
| JWST   | James Webb Space Telescope                   |
| LRO    | Lunar Reconnaissance Orbiter                 |
| MEMS   | Microelectromechanical System                |
| MIMU   | Miniature Inertial Measurement Unit          |



|       |  |
|-------|--|
| MTB   | Magnetic Torque Bar  |
| NASA  | National Aeronautics and Space Administration              |
| NEMS  | Nanoelectromechanical System                               |
| NPS   | Naval Postgraduate School                                  |
| OAQ   | Orbiting Astronomical Observatory                          |
| OGO   | Orbiting Geophysical Observatory                           |
| OGS   | One Gyro Science Mode                                      |
| OSO   | Orbiting Solar Observatory                                 |
| PDF   | Probability Distribution Function                          |
| PID   | Proportional-Integrator-Derivative Controller              |
| RW    | Reaction Wheel   |
| RWA   | Reaction Wheel Assembly                                    |
| RGA   | Rate Gyro Assembly   |
| SOHO  | Solar and Heliospheric Observatory                         |
| STA   | Star-Tracker Assembly                                      |
| TAM   | Three-Axis Magnetometer                                    |
| TIMED | Thermosphere Ionosphere Mesosphere Energetics and Dynamics |
| TLE   | Two-Line Element   |
| TGS   | Two Gyro Science Mode                                      |
| TIROS | Television and Infra-Red Observation Satellite             |
| UCS   | Union of Concerned Scientists                              |
| VCL   | Vegetation Canopy Lidar                                    |

## ACKNOWLEDGMENTS

Thank you to everyone who has been supportive of my efforts during my PhD journey. Your positive thoughts, constructive criticism, and prayers have finally paid dividends! There are many people who have contributed to the achievement of this milestone, and I am grateful for every one of them. I will try to capture as many here as I can, and if I do miss someone, please know I appreciate you, too.

First and foremost, thank you to my family: Dan, Martin, Mom, Dad, Tara, aunts, uncles, cousins, and in-laws for their support. Education, both formally through schooling, and informally through the lifelong quest for learning, has been a priority for you. Through your examples, it has been a priority for me as well. Thank you for the immeasurable amounts of delicious home cooking you have provided to fuel the creation of this dissertation. Special thanks to Martin, whose arrival motivated me to finish this work and whose notes of love and encouragement motivate me to do my best every day.

Thank you to my dissertation committee: Dr. Mark Karpenko, Dr. I. Mike Ross, Dr. Isaac Kaminer, Dr. Jim Newman, and Dr. Frank Giraldo for your many hours of teaching, discussion, and most of all patience. Thank you for helping me make much-needed improvements. Your investment of time and expertise has been invaluable and will always be greatly appreciated.

Thank you to my work team, all the folks who make up the Space Systems Academic Group at NPS, especially Dr. Jim Newman, Dr. Wenschel Lan, Dr. Giovanni Minelli, Alex Savattone, Noah Weitz, David Rigmaiden, Jim Horning, Gary Thomason, Ron Phelps, Dan Sakoda, Dan Bursch and, most importantly, Dr. Rudy Panholzer. Thank you for making our office and lab such an amazing place to work. You make our space enjoyable, and I am fortunate to share this special place.

Thank you to my dear friend, Meghan Buchanan, who introduced me to the Naval Postgraduate School (NPS) and all the amazing people who work here. Your efforts laid the foundation for my achievement, and I am forever grateful. Keep climbing mountains my friend!

Thank you to my dear friend, Shankini Doraisingam, who was available to listen when I needed a kind ear. Our chats always brought a smile to my face while offering much-needed perspective. Please write a book about space spiders!

Thank you to Dr. Donna Gerren, who exemplified being a female Doctor of Aerospace Engineering. Your positive attitude, love of occupation and devotion to your students continues to inspire those around you. I am grateful to be counted among them. Thank you for setting an admirable example.

Thank you to my friends, Anne Howell Hubbard and Emma Williams, whom I have known since we were twelve years old! I am grateful for our enduring friendships and too-infrequent trips to the beach. Your laughter, Old Bay seasoning, and Beef Wellington are to die for! Thank you again, Anne, for the early morning Krispy Kreme rescue—you are my angel. Although I declined your suggestions to name my child after you, perhaps I can name my diploma after you? Behold the Anne-Emma! HA!

Many thanks to friends, neighbors, work mates, fellow students, and NPS Toastmasters for providing much-needed encouragement: Anna & Emanuele Bartolini, Dominick Bruno, Arnie Buss, Annette Cain, Van G. Chaney, Steev & Mary Beth Ditamore, Bill & Molly Evans, Kristin Fortino, Monique Fountain, Calina Franzosa, Carrie Glenn, Brenda Goodman, Spencer Green, Pat Hanson, Dean Hawes, Chas Hewgley, Sabrina Hiltunen, Nancy Hutchins, Marianna Jones, Jeff King, Kate Kurz, Amy Mahone, Tetyana Margolina, Meg Masquelier, Ruth McMaster, Mandy Orosco, Gladys Parada, Todd Richardson, Elsa Rivera, Nicole, Jonathan & Amelia Roberts, Dennis & Cindy Romero, Corrie Rothman, Fred Sadler, Molly Sand, Laurie & John Sheehan, Sam & Katie Spadoni, Art Testani, Rachelle Thompson, Carl Thormeyer, Bob Tilden, Gypsy Jeff Warfield, Kyle Wood, and others.

In closing, I would like to provide a few of my favorite quotes:

“There is always room for improvement.”—Dr. Jim Newman

“Onward and upward!”—Dr. Rudy Panholzer

“Do not give up when things get tough.”—Thomas Zurbuchen

# **I. INTRODUCTION**

Many spacecraft have a life expectancy that far exceeds their planned mission durations and therefore remain in orbit albeit with modified tasking. For example, the original mission duration for the National Aeronautics and Space Administration (NASA) Kepler space observatory (launched in March 2009) was 3.5 years [1], but the satellite was able to perform scientific measurements for over 9 years before being officially retired in October 2018 [2]. Similarly, NASA's Lunar Reconnaissance Orbiter (LRO) has had its mission extended multiple times and has been operating for over 13 years, well beyond the planned 3-year primary mission [3]. Another astonishing example is the Hubble Space Telescope (HST), which has been in operation for over 32 years since its launch in April 1990 [4].

These and other scientific spacecraft's extended missions are a result of the community's ability to develop guidance and control algorithms that keep systems operating when hardware control components such as rate gyros or miniature inertial measurement units (MIMU) fail intermittently or completely. As spacecraft components shrink in size and grow in computational capability, there is motivation to explore novel software solutions that can overcome these common hardware failures. This dissertation explores the possibility of using an optimal control technique called "unscented guidance" to minimize pointing error of a large angle maneuver implemented in the open-loop, allowing a spacecraft with degraded hardware to continue to operate. This method could be used to extend the scientific missions of multi-billion-dollar spacecraft thereby providing a greater return on taxpayer investment as well as potentially years-more data about the makeup of the surface of the moon, the existence of planets outside our solar system and images of galaxies far away or as a software replacement to rate gyros which is desirable for many small satellites (typically less than 200kg).

## **A. MOTIVATION**

Spacecraft are manufactured in an array of sizes, capabilities, and prices. From exquisite (large, highly capable, and expensive) to experimental (small, limited capability,

and inexpensive), these attributes are traded with one another to fit the desired mission. A current example of exquisite, the James Webb Space Telescope (JWST), fully deployed to a size of approximately 21.2m x 14.6m x 10.6m with a mass of 6330kg and cost about \$10 billion [5-6]. Its attitude determination and control system (ADCS) suite of instruments includes three star-tracker assemblies (STA), one inertial reference unit (IRU), two fine sun sensors (FSS) and four coarse sun sensors (CSS) for attitude determination with six reaction wheel assemblies (RWA) (sets with isolators in a pyramidal configuration) and thrusters for attitude control and momentum management [7]. Conversely, in the experimental realm, a 0.1m x 0.1m x 0.1m (1U) spacecraft with mass less than 1.3kg and no ADCS can be assembled for about \$50,000 using off-the-shelf components from companies such as Pumpkin, Inc. Although there is no definition of a typical satellite or a typical ADCS, in between exquisite and experimental lies a representative satellite with a representative ADCS which will be defined in the following paragraphs.

Modern spacecraft contain a variety of sub-systems including command and data handling (C&DH), electrical, structural, ADCS, communications, thermal and payloads. The ADCS provides spacecraft pointing, or a three-dimensional orientation of a space vehicle with respect to a reference frame. To accomplish spacecraft pointing, the ADCS uses a combination of sensors, software, and actuators. Sensors take measurements of rate or position relative to a known reference point and provide the information to the control software. This software determines how to apply control torques and sends commands to actuators that supply the desired control torques [8]. When all parts are functioning as designed, spacecraft pointing occurs with both accuracy and precision enabling scientific payloads to perform their duties. Contributions from all sub-systems, including the ADCS, must be considered against mission objectives, however, this dissertation will focus primarily on the contributions of the ADCS.

Attitude and rate sensors are measurement devices that include sun sensors, horizon sensors, magnetometers, star sensors and gyroscopes. Each sensor provides information about the spacecraft with respect to a particular reference frame. Most spacecraft have a combination of sensors with onboard processing capable of handling the inherent reference frame transformations. Spacecraft attitude determination system accuracy is dependent on

the accuracy of these sensors. Star-trackers are the most accurate source, typically with sub-arc-second accuracy [9].

Modern ADCS software aggregates available sensor measurements from on-board sources such as earth and star sensors, external sources such as Global Positioning System (GPS) and ground-based sources such as two-line element sets (TLEs), then processes the information to determine the spacecraft attitude in an inertial frame. Based on the current attitude and mode in which the spacecraft operates, such as nominal or low power, the software references an attitude control profile. At the appropriate time, the ADCS software provides commands to the actuators to execute the desired attitude control profile.

Actuators include gas thrusters, magnetic coils, and momentum exchange devices. These devices provide forces (translational acceleration) or torques (angular acceleration) to the spacecraft [9]. Gas thrusters can provide the greatest amount of torque, and they are often used on large spacecraft. At the other end of the torque spectrum, magnetic coils are found on small satellites where concerns over size and hazardous propellant make gas thrusters unpalatable. Safely in the middle, then, momentum exchange devices provide less torque than gas thrusters, more than magnetic coils, and are found on spacecraft large and small due to their demonstrated ability to provide precision pointing and relative low cost.

There are many combinations of spacecraft attitude determination sensors, software, and actuators. Every spacecraft program tailors the combination to their mission needs. Regardless of the situation, if a spacecraft desires fine pointing then a capable attitude control system is imperative [9].

## **B. BACKGROUND**

Satellites and their sub-systems have grown increasingly more sophisticated. In the realm of attitude control, passive attitude control has given way to active attitude control, momentum storage has been harnessed, hardware components have shrunk and consolidated onto computer chips and many on-board operations have transitioned from analog to digital, human in the loop to autonomous. As the ability to compute more

processes continues to grow and hardware continues to shrink, significant changes are, and will be, taking place with not only spacecraft appearance, but also spacecraft operations.

## **1. Attitude Control**

Modern attitude control literature often assumes three-axis attitude control, but satellites did not begin as objects with three axes of control. The earliest satellites lacked active control and as their technology advanced, single axis control and later multiple axis control were developed. Multi-axis attitude control is necessary for spacecraft that require accurate pointing. Although mission-driven, many modern, large spacecraft contain multi-axis control systems as do a significant portion of small spacecraft such as SpaceX's Starlink satellites.

Attitude control is separated into two groups, active and passive [10]. Active attitude control and stabilization requires dedicated torque production hardware, such as reaction wheels, coupled with controllers that minimize attitude error [9]. Many early satellites were equipped with limited computational and power resources, so active attitude control was not an option. Passive attitude stabilization is dependent on environmental torques and requires very little on-board computing or power, if any. Spin-stabilization is a passive spacecraft stabilization method that allows a limited amount of control about a single axis due to the gyroscopic torque generated by the spinning motion of the spacecraft. D. B. DeBra discusses methods of spacecraft control, including spin-stabilization that he refers to as “spin control,” and how these methods have changed to accommodate technology advances, in his 1981 paper “Evolving Spacecraft Control” [11]. Early examples of satellites that relied on spin-stabilization for attitude stabilization were the United States' Explorer satellites that launched in 1958 [11]. As DeBra noted, “Not all payloads operated well from a spinning platform” and alternative control methods followed.

Mission designers desired a way to point sensors and payloads continuously at objects such as the sun and a spinning spacecraft was not capable of meeting this requirement. To provide continuous pointing, the space survivable joint was developed. This joint allowed one part of the spacecraft to spin while other parts were pointed at a

desired object. This joint was a key design innovation for both the Orbiting Solar Observatory (OSO) series of spacecraft and the Improved Television Infrared Observation Satellite (ITOS) also known as TIROS-M [11]. OSO launched from 1962–1969 and employed dual-spin stabilization whereby one part of the spacecraft spins and the other part does not spin. ITOS was launched in 1970 and internalized the spinning wheel, termed a “flywheel” [11-12]. The initial Television Infrared Observation Satellite (TIROS) were launched between 1960 and 1965 and all were spinning satellites; these satellites were the first experimental weather satellites [13]. Development of the space survivable joint provided the second generation of TIROS spacecraft, ITOS, momentum storage and attitude stability which allowed the satellites to point cameras and infrared sensors directly at the earth [11].

The Nimbus series of spacecraft, launched from 1964 - 1978, addressed the principal ‘defect of (first generation) TIROS’ [14]. The Nimbus spacecraft featured an active, three-axis attitude control system, instead of a passive, spinning spacecraft, that provided attitude stabilization and control [14]. This active, three-axis attitude control system was based on General Electric’s (GE) prior work with the MARK IIIC TP ICBM re-entry vehicle and after launch on August 28, 1964, it made Nimbus I the first three-axis, fully stabilized satellite [14-15]. The Nimbus attitude control system managed torque using three reaction wheels for pointing and cold-gas thrusters for momentum unloading. Infrared horizon scanners provided pitch and roll error signals to the attitude control system. Later versions of Nimbus also included gravity-gradient stabilization hardware and a sun sensor that provided yaw axis error signals [15-16]. Shortly after Nimbus I launched, on September 5, 1964, the first of a series of six Orbiting Geophysical Observatory (OGO) spacecraft was launched demonstrating that three-axis attitude control could also be achieved using gas jets and horizon scanners without using reaction wheels. Like TIROS and Nimbus, the OGO satellites used their pointing ability to look directly at the earth [17].

Three-axis attitude control has been achieved using myriad methods, but the most popular has employed reaction wheels as actuators. Harold Perkel introduced a concept he termed “Stabilite” in his 1966 paper “Stabilite - A Three-Axis Attitude Control System” as a method to control three-axis motion of a spacecraft [12]. Perkel concluded his paper with



a prediction that “it is likely that some form of Stabilite will satisfy more missions than any other form of attitude stabilization” [12]. His prediction has proven accurate as SpaceX continues to launch Starlink satellites. Numbering over 2,800 thus far, and approved for 12,000, each one contains a three-axis attitude control system utilizing a set of four reaction wheels [18]. This constellation of satellites will dwarf the number of currently operational satellites which is 4,852 (including Starlink) as of December 31, 2021, according to the Union of Concerned Scientists (UCS) satellite database [19]. Three-axis attitude control using reaction wheels is the most common form of three-axis satellite attitude control.

## **2. Momentum Storage**

A rotating element, whether it is the satellite itself or a wheel contained within a satellite, provides a way to store angular momentum onboard a spacecraft. This gyroscopic quality is advantageous because it provides spacecraft attitude stability and a way to transfer momentum to and from the satellite body [20]. There are two basic types of momentum storage units: control moment gyros (CMGs) which are gimballed, meaning they maintain a level position as their support is moved, and momentum/reaction wheels which have a support mounted to the spacecraft.

A CMG contains a gimballed wheel that spins at a constant rate. One CMG is required for each axis of desired attitude control with additional units often provided for redundancy. Until recently, CMGs have been large, heavy, and expensive so they typically have been reserved for spacecraft that were also large, heavy, and expensive.

The terms momentum wheel and reaction wheel are often used interchangeably although momentum wheel usually refers to a reaction wheel that is intended to operate at a relatively high speed [21]. Momentum and reaction wheels use the same hardware with the name difference based on how the wheels are used. One wheel is required for each axis of desired attitude control, for three-axis attitude control there are three wheels often arranged along body axes or in a pyramidal shape with a fourth wheel provided for redundancy. Earth-pointing spacecraft, such as the ITOS satellites, employ momentum bias along the pitch-axis such that pitch control is maintained by momentum wheel torque control [12].

Momentum/reaction wheels are the “primary attitude control actuators on most spacecraft” [22]. Reaction wheels as actuators is a design that has been more accessible than other hardware designs due to the relatively small, light, and inexpensive form factor which has contributed to its popularity. Regardless of the specific type or physical arrangement, rotating elements such as reaction wheels leverage momentum storage to provide desired attitude stability and control for spacecraft.

### **3. Representative Spacecraft**

The breadth of spacecraft size and capability, especially when considered along an historical arc, is extensive and this dissertation will not attempt to address all the possibilities. To illustrate the novel work in this dissertation, a representative spacecraft is defined. The UCS currently operational satellite database was used as a starting point to which was added non-operational and defunct satellites [19]. Based on the resulting list of unclassified satellites that have been put into orbit since 1957, it was found that the average mass of a satellite is approximately 1500 kg. Since this dissertation is focused on the ADCS sub-system, the representative spacecraft must include high-precision pointing capability, on the order of sub-arcseconds, which is provided by an active, three-axis attitude control system with reaction wheels for pointing control and momentum storage. Best uses for this type of satellite lie in multi-target scenarios such as telescopes, gamma-ray burst observatories, X-ray observatories or spectroscopy.

The representative spacecraft chosen for use in this dissertation is purposefully skewed toward a medium-large capable spacecraft that is already on-orbit as it is this type of spacecraft that could immediately benefit from the novel work that is presented here. Smaller or less-capable spacecraft could also benefit, but they will be excluded from present analysis. The Far-Ultraviolet Spectroscopic Explorer (FUSE) satellite is a good example of a representative spacecraft. At 1360 kg and approximately 5.3 m x 1.9 m in size, it was launched into a 765 km circular, 25 deg inclination orbit on June 24, 1999 [23]. Its mission was to observe light in high resolution in the far ultraviolet (905–1187 Angstroms) spectral range from a wide range of astronomical sources such as stars, planetary nebulae, interstellar gas, intergalactic gas, and winds from massive stars [23]. To

achieve the pointing and stability accuracy necessary for this mission, the FUSE ADCS system included: two (redundant) three-axis magnetometers (TAMs), one fine error sensor (FES) camera, CSSs, two (redundant) IRUs each containing a set of three body-axis aligned, orthogonally mounted gyroscopes, four reaction wheels (three aligned with the spacecraft body axes and one redundant), and three orthogonally mounted, body-axis parallel magnetic torque bars (MTBs) for momentum management [24]. Additionally, this spacecraft was designed to be fully redundant, which means every measurement sensor and control surface had at least one hardware backup [25-26]. Although this mission launched during the 1990s “faster, better, cheaper” era as one of several cost-constrained, less than \$200 million, NASA Goddard Space Flight Center’s (GSFC) Explorers satellites, the circa 1999 state-of-the-art for high pointing accuracy spacecraft dictated fully redundant hardware systems to manage on-orbit hardware failures [23].

Many spacecraft have been built that followed a similar recipe for ADCS construction as FUSE: the International Ultraviolet Explorer (IUE) launched in 1978, Hubble Space Telescope (HST) launched in 1990, Solar and Heliospheric Observatory (SOHO) launched in 1995, Thermosphere Ionosphere Mesosphere Energetics and Dynamics (TIMED) launched in 2001. More recent examples include Dawn launched in 2007, Lunar Reconnaissance Orbiter (LRO) launched in 2009 and Vegetation Canopy LIDAR (VCL)/Glory launched in 2011. Table 1 summarizes these examples.

Table 1. ADCS Sensor and Actuator Combinations for Spacecraft Similar to the Representative Spacecraft

| Spacecraft     | Sensors                 |                       |   |              |            | Actuators           |                            |           |
|----------------|-------------------------|-----------------------|---|--------------|------------|---------------------|----------------------------|-----------|
|                | Coarse Sun Sensor (CSS) | Fine Sun Sensor (FSS) | Star-Tracker or Fine Error Sensor (FES) | Magnetometer | Rate Gyros | Reaction Wheel (RW) | Magnetic Torque bars (MTB) | Thrusters |
| Dawn [27-28]   | 16                      | N                     | 2                                       | N            | 3 (2DOF)   | 4                   | N                          | Y         |
| FUSE [24]      | Y                       | N                     | 1                                       | 2            | 6 (1DOF)   | 4                   | 3                          | N         |
| HST [29]       | 5                       | N                     | 3                                       | 2            | 6 (1DOF)   | 4                   | 4                          | N         |
| IUE [30]       | N                       | 2                     | 1                                       | N            | 6 (1DOF)   | 4                   | N                          | Y         |
| LRO [31-32]    | 10                      | N                     | 2                                       | N            | 3 (1DOF)   | 4                   | N                          | Y         |
| SOHO [33]      | N                       | 1                     | 1                                       | N            | 3 (2DOF)   | 4                   | N                          | Y         |
| TIMED [34]     | 4                       | N                     | 2                                       | 2            | 2 (3DOF)   | 4                   | 3                          | N         |
| VCL/Glory [35] | 16                      | N                     | 2                                       | 1            | 1 (3DOF)   | 4                   | N                          | Y         |

A better example of a representative spacecraft used to illustrate the novel work in this dissertation is the Lunar Reconnaissance Orbiter (LRO). LRO is used in dissertation simulations as the representative spacecraft. It is approximately 1916 kg in mass and asymmetrical in shape [36]. Its ADCS contains four reaction wheels for actuation and has a Miniature Inertial Measurement Unit (MIMU) that contains three rate gyros [31-32]. An issue with the MIMU negatively impacted LRO's maneuvering ability. Control system algorithms were modified on-orbit to mathematically manipulate data from other onboard sensors to replace missing MIMU data and allow continued operations [37]. This combination of mass, on-board control system capability and relevant on-orbit issue makes LRO an ideal model for use in this dissertation.

#### **4. ADCS Components**

Throughout the 1990s, improvements in digital component technology transformed control system hardware and software in the aerospace industry. Proliferation of digital control technology happened in aircraft and spacecraft controls as manufacturers replaced analog control electronics with digital versions [38]. By the early 2000s, microelectromechanical systems (MEMS) and nanoelectromechanical systems (NEMS) use in spacecraft were predicted to “evolve over the next decade to provide ever-higher levels of functional density per unit area” while the “continuing increase in functional density will enable decreased spacecraft system size, and ultra-small spacecraft” [39]. Today, MEMS based gyroscopes and accelerometers are readily available. MEMS technology has allowed control system designs to shrink by several orders of magnitude. For example, a Honeywell HG4930 MEMS Inertial Measurement Unit (IMU) that includes three MEMS rate gyroscopes and three accelerometers available in 2020 is about the same volume and mass as one Bendix rate gyroscope available in 1978 [40-41].

Sun sensors and horizon sensors have similarly shrunk in size yet gained functionality. Sensors that used to be larger than a deck of cards (81 x 81 x 20 mm), weighed as much as a coffee cup (259 g) and often required analog-to-digital conversion are now available in sizes that are smaller in diameter than a penny, are one-seventh the previous mass (19 mm, 3 g) and embed functionality within the sensor packaging, although heritage designs continue to be available [42-46].

Star sensors also have benefitted from technological advances that brought about miniaturization and lower cost, in this case via complementary metal oxide semiconductor (CMOS) technology that was applied to the manufacture of multi-megapixel cameras [45]. CMOS active pixel sensor (APS) technology enabled mass production of “one-chip imaging systems with a full digital interface” and were predicted in 1995 to “make image capture devices as ubiquitous in our daily lives as the microprocessor” with CMOS APS cameras emerging for use in sun sensors and star cameras [47-48]. Modern star-trackers utilize this technology to match tracked stars against a catalog for the purpose of determining the inertial position of a satellite, that is position of the satellite relative to a

celestial reference frame [22]. Typical update rates for modern star-trackers are between 0.5-10 Hz with a high update rate version at 50 Hz in development [22], [49].

## **5. Representative Problem**

Spacecraft anomalies (what happens when things go wrong) have been around for as long as spacecraft. Explorer-I, the first American satellite, experienced a flat spin about the maximum moment of inertia after several orbits, which was unplanned, but the spacecraft was able to continue its mission [50]. There are many reasons why spacecraft experience anomalies including poor engineering and faulty components. Component failures are of particular interest because they can seem random in their occurrences, but with a focus on spacecraft robustness, engineers can design solutions into the spacecraft that withstand these failures and deliver a successful mission [51], [52]. Component failures - particularly rate gyros - range from human-induced failures such as with IUE and SOHO to the slow degradation effects of old age such as with the Hubble Space Telescope and LRO. There are also plenty of examples in between including FUSE and TIMED.

IUE launched in 1978 with an expected life span of three years. One-and-one-half years into the mission, three gyros were turned off during eclipse season and only two restarted when power was restored [52-53]. At four-and-one-half years into the mission, three gyros were non-operational while three remained. Contingency plans were developed for additional gyro failures such that fine digital sun sensor data was repurposed for the failed axis or axes and combined with the remaining gyro data to continue three-axis control [53]. The spacecraft was operational for eighteen years, far exceeding its original goal of three [30], [50].

SOHO launched in 1995, completed its primary two-year mission in May 1998 and then entered an extended mission phase. In June 1998, ground control command errors during an otherwise routine gyroscope calibration and momentum unloading event caused the spacecraft to be oriented in such a way that the gyro flotation fluid froze. The frozen fluid fractured the electrical connections thus causing the failure of all six gyros [50]. SOHO benefitted from follow-on contingency plans that were developed for IUE and as a

result, (as of the writing of this dissertation) SOHO continues to operate well into its twenty-sixth year [50].

The Hubble Space Telescope deployed from the space shuttle in April of 1990. Part of its operations plan involved the use of manned servicing missions to replace the limited-life rate gyroscopes [54]. These gyros have been replaced several times over five servicing missions [55]. Since future servicing missions are not possible - due to the cancellation of the Space Shuttle program—it is necessary to utilize software methods such as Hubble’s two- and one-gyro science control laws that compensate for the loss of the aging rate gyros to maintain the mission. The two- and one-gyro science control laws fuse measurements from magnetometers, star-trackers, and fine guidance sensors to close the loop about failed gyro axes [56]. The evolution of Hubble’s attitude control system has allowed it to continue operations for over thirty-two years.

LRO was launched in June of 2009 and by early 2018 had powered off its MIMU due to X-axis gyro degraded laser intensity [37]. In the original LRO design, three single-axis gyros, X, Y, & Z, plus internal processing formed the MIMU. Measurements from the MIMU were combined with measurements from two star-trackers and this combination was provided to a Kalman filter to estimate the satellite attitude and rate [37]. After MIMU failure, with the MIMU no longer in the control loop, the satellite was unable to perform science slews—these are slews between targets that are large, on the order of tens to hundreds of degrees—because there was insufficient information to estimate the satellite attitude and rate. To overcome this issue, the satellite estimates rate by mathematically manipulating position and torque sensor measurements—specifically via a complementary filter that uses differentiated quaternions and integrated angular acceleration [37]. These changes to the control system have allowed LRO to continue operations and it provides science data well into its twelfth year.

FUSE launched in June of 1999 and by October of 2001 had experienced a failure of one of the six gyros and degraded laser intensity, tripping low-intensity indicators, on five of the six gyros [23], [25]. FUSE was planned to operate a three-year mission, but this goal looked questionable at two-and-one-half years into the mission when science operations were stopped due to the gyro failure coupled with the loss of two of the four

reaction wheels [26]. Through significant modifications to control system algorithms, including use of repurposed fine error sensor and three-axis magnetometer data and the addition of a non-linear dynamical model of the satellite, the mission was extended to more than eight years [23], [25].

TIMED launched in December of 2001 with an expected mission lifetime of two years. Like the gyro degradation seen with the FUSE spacecraft, one year after launch, a single axis (gyro) began to fail in the primary Inertial Reference Unit (IRU) assembly, so the secondary IRU was turned on. One year later, a single axis of the backup IRU began to fail [34]. A change to the control system software, which used star-tracker provided differentiated quaternions and sun sensor data, allowed the mission to continue and it is now well into its twentieth year [34].

It is clear to see that rate gyros are failure prone [23], [34], [37], [50], [54-55], [57]. The failures described here have negatively impacted many spacecraft missions both through downtime as new control laws are developed and tested, such as with Hubble, and through reduced science collection due to maneuver constraints imposed by control law redesign, such as with LRO. A lack of confidence in gyro reliability and gyro failures motivate the idea of gyroless attitude control [50].

## **6. Gyroless Attitude Control: Closed-Loop**

The idea of gyroless attitude control has been around since the 1960s [50]. Implementation of gyroless attitude control, however, has been much more elusive. Gyroless solutions have been applied to emergency situations when gyros have failed on-orbit. Rarely, until the recent development of capable small satellite designs, has a gyroless attitude control solution been implemented as a nominal—primary—operating solution [58]. Even for these modern, gyroless small satellites, the governing attitude control system depends on feedback-based (closed-loop) attitude control. Closed-loop attitude control requires on-board sensor position and rate information to be continuously fed into feedback dependent software that provides spacecraft attitude control commands to the spacecraft actuators which results in spacecraft movement.



Concerns about gyro reliability motivated the gyroless design of the first Orbiting Astronomical Observatory (OAO) satellite, part of a four-satellite series launched from 1966–1972. The first OAO was gyroless and six star-trackers were the method to provide attitude reference [50]. This satellite operated for seven minutes at which time it experienced high-voltage arcing of the star-trackers which caused a lack of satellite control that led to battery depletion and was terminated after 20 orbits (~3 days). Following this failure, the subsequent three OAO spacecraft were built with IRUs containing gyros to provide attitude reference instead of star-trackers [50].

In 1982, the IUE satellite experienced two on-orbit gyro failures, which coupled with an earlier failure of one gyro, left the satellite with three of the original six. While three gyros were sufficient for satellite operation, the team at NASA's Goddard Spaceflight Center (GSFC) was worried about the possibility of another failure which would probably end the mission, so they were tasked with development of a sub-arc second pointing two-gyro control system, that was considered impossible at the time [50], [53]. The two-gyro control system that the team at Goddard developed over the following year depended on deriving rate data for the missing axis from the Fine Sun Sensor (FSS) position data; they later extended this effort to one-gyro control with the FSS providing derived rate data for the two missing axes [53]. The two-gyro control laws were utilized on-orbit with performance similar to the baseline whereas the one-gyro control laws were tested on-orbit but never used for operations [22].

Zero-gyro control laws were eventually developed, in anticipation of further gyro degradation, for the purpose of keeping the spacecraft power and thermal-safe but would not have provided the sub-arc-second pointing accuracy necessary to continue the IUE science mission [50], [59]. This was the first evidence of a zero-gyro software solution for fixing a failed gyro hardware problem. The IUE zero-gyro control laws, like the one-gyro version, used the FSS to provide two axes of position and derived rate information [30]. For the third axis, the zero-gyro version used thrusters to set a momentum bias “anchor” to inertially fix the satellite then measured the momentum transfer between reaction wheels and integrated this measurement to determine angular rate and position of the third axis [30], [59]. Although this zero-gyro solution was never used for IUE operations, it was re-

purposed for use on the SOHO satellite after all six of its gyros failed on-orbit in 1998. SOHO did not require precision pointing, so the IUE-developed zero-gyro solution sufficed as a substitute for the failed gyros, and this satellite is still operating [50].

Between the IUE experience in 1982 and today, engineers at GSFC and supporting aerospace entities—Orbital Sciences (now Northrup Grumman), Johns Hopkins University, and Lockheed Martin—became fluent in the implementation of zero-gyro software solutions for on-orbit gyro hardware failures [58]. Various methods for substitution of missing angular rate information emerged such as fine sun sensors coupled with a momentum bias anchor for IUE and SOHO. Another approach was to use coarse sun sensors coupled with magnetometer data for the low-earth orbiting HST [60-62]. The FUSE mission used a payload provided fine error sensor coupled with magnetometer data [26]. Yet another approach was to use differentiated quaternions (from star trackers) coupled with other sensor data. TIMED combined coarse sun sensor data with differentiated quaternions whereas LRO combined angular acceleration (from integration of a control torque) with differentiated quaternions [34], [37]. In each case, the closed-loop control system design dictated a constant input of angular rate information. Once this information was no longer available, each of these bespoke zero-gyro solutions was developed to provide an alternative rate data stream using a combination of on-board sensor data that was never intended to be used as angular rate data. Although these fixes were clever and often extended the mission, they were also time consuming, difficult to produce and test after the spacecraft had launched, and inefficiency was inherent.

Many papers have explored gyroless attitude control systems and cited advancements in star-tracker and microprocessor technologies as reasons that could allow star-trackers to eclipse the use of gyros for spacecraft angular rate reference. Authors from Draper Labs and RCA in 1982 to Thales Alenia Space with Agenzia Spaziale Italiana in 2018, and many others, have proposed star-trackers or combinations of star-trackers with other on-board sensors as innovative control concepts that eliminated the need for gyros [49], [63-81]. Star-tracker-based gyroless attitude control systems have become common in small satellites and, regardless of spacecraft size, continue to be a popular research area as star-tracker size shrinks and robustness improves [82-83].

Microprocessor and MEMS improvements have not only have benefitted star-tracker attitude control algorithms, but also improved other gyroless attitude control algorithms. The ability of microprocessors to compute complex data sets on-board spacecraft has both increased their utility and shrunk their size [45]. Gyroless attitude control systems are a natural progression from large, unreliable hardware to smaller, more reliable hardware whose measurements are aggregated and processed on-board the spacecraft using microprocessor technology. In the case of many small satellites, star-trackers paired with on-board microprocessors performing quaternion differentiation have replaced the functionality of rate gyros [84].

Gyroless attitude control methods require angular velocity estimation to replace missing rate sensor data. Gyroless methods in general fall into one of the four following categories: derivation, estimation, integration, or combination. Star trackers are a special case of the derivation category but were discussed independently due to their singular importance and proliferation in gyroless implementations. The paper “Classification of Algorithms for Angular Velocity Estimation” by Itzhack Bar-Itzhack defines two methods for estimation: the “derivative approach” captures those methods that explicitly perform a differentiation of measured positions with respect to time; the “estimation approach” captures methods that use initial guesses to directly populate an estimation algorithm that obtains a rate estimate as part of the state space [85]. Categorizing gyroless attitude control methods is confusing since many of the methods overlap or use two-stage processes which, by definition, involve multiple methods. Confusion regarding categorization is made worse by references that change categories. A 1998 paper, “The Use of Pseudo-Linear and SDARE Filtering for Satellite Angular-Rate Estimation” by Richard Harman and Itzhack Bar-Itzhack cited the “Magnetometer-Only Attitude and Rate Estimates During the Earth Radiation Budget Satellite 1987 Control Anomaly” paper by M. Challa, S. Kotaru and G. Natanson as an example of a derivation approach [86-87]. However, Bar-Itzhack’s 2001 paper “Classification of Algorithms for Angular Velocity Estimation” cites the M. Challa, S. Kotaru and G. Natanson paper as an example of an estimation approach. For the purposes of this dissertation, the dividing line between derivation and estimation algorithms is drawn at the sensor; derivation methods apply to references where position sensor(s) are specified

whereas estimation methods apply to references where no specific sensor or set of sensors is identified.

Derivation methods utilize on-board sensor measurements from magnetometers, sun sensors or GPS signals, in addition to star-trackers as previously discussed [57], [86-122]. Spacecraft angular rate calculations are performed via differentiation with respect to time of the available position vector or vectors. This calculation is performed either inside a filtering algorithm or outside with the results fed into the filter.

Estimation methods typically are sensor agnostic and in this sense are more generic than derivation methods. Estimation methods are seeded with many types of data including on-board sensor vector measurements, *a priori* data, parameter models or used for offline processing [123-138]. Estimation methods commonly use Kalman filters as part of their design.

Integration methods utilize measurements of spacecraft control torques, disturbance torques or changes in spacecraft angular momentum to provide a rate calculation which is used to seed a dynamics model [136], [139-141]. Accuracy of the rate calculation is dependent on the accuracy of the dynamics model and sensor information [140]. Dynamics models are often inaccurate due to unknowns such as disturbances that are associated with the spacecraft environment.

When sensor data is aggregated from multiple sources or novel methods of processing data are introduced, a combination of methods can result [84], [142-147]. A combination of methods often happens when multiple sensor measurements require different algorithms for processing. A common example is a combination of derivation of star-tracker position and integration of reaction wheel speed change that are used together to generate a rate calculation.

Regardless of method, replacing the rate gyro angular rate data stream is a challenging task that introduces error and risk to the satellite program. Gyroless control modes have been avoided in baseline designs of attitude control software. Historically, avoidance was due to a lack of on-board memory although that issue has vanished with improvements in on-board computing. A couple of examples where gyroless control modes

were purposefully built into an attitude control system include the Dawn and SORCE spacecraft [27], [104]. Dawn's gyroless mode was built to operate during cruise mode, as the satellite traveled to an asteroid, to preserve rate gyro lifetime for science operations. SORCE's gyroless mode was developed in response to schedule and cost constraints that caused the rate gyros to be unavailable late in the development cycle. Although SORCE's gyroless mode was successful on-orbit, it was not the design that was intended, and operators had to ensure that at least one star-tracker was always un-occulted (not obscured) which caused scheduling and maneuver difficulties [58]. LRO experienced similar operational challenges with its on-orbit-developed gyroless control mode. At least one star-tracker always had to be available during a large maneuver, otherwise, the Kalman filter might diverge, and this divergence would then destabilize the feedback loop. An approach taken to avoid obscuration of the star-trackers during large-angle maneuvers was a constrained maneuver trajectory [148] in which keep-out cones prevented star-tracker obscuration.

Today, gyroless control modes for large spacecraft are rarely included in the control system design because spacecraft developers focus on designs that have succeeded in space before and there is very little tolerance for risk which leads to a perpetuation of the same, proven design that includes rate gyros [58]. Small spacecraft have been a notable exception over the past few years. The risk tolerance for a small satellite (under 200kg) program is much higher while the available volume, mass, and power to accommodate a rate gyro system is much lower, in fact in many cases, does not exist. Small satellites have made the idea of gyroless control a reality albeit with concessions in pointing stability. Large spacecraft, like the Chandra X-Ray Observatory, have depended upon high accuracy attitude control for decades; Chandra was able to achieve 0.04 arcsecond pointing stability on-orbit in 1999 [149]. Twenty-two years later, the best small satellite performance to date is from the Blue Canyon Technologies XACT unit which was able to achieve 1.8-4.6 arcsecond pointing stability on the ASTERIA 6U CubeSat in 2017 [150]. Shrinking electronics while expanding their capability has been ongoing for a few decades but shrinking spacecraft control system hardware has proven more difficult. Research involving small satellite gyroless systems with fine pointing stability continues. To date,

small spacecraft control system hardware has not yet provided the same pointing stability as large spacecraft hardware.

Large spacecraft or small, gyroless attitude control solutions have depended on closed-loop (feedback) implementation. For baseline spacecraft control, feedback offers stability and robustness in a realm of uncertainties. In his book *Synthesis of Feedback Systems*, Isaac Horowitz states: “One of the foremost properties of feedback is its ability to reduce the sensitivity of a system to variations in the system parameters” [151]. This means that over time, the feedback attitude control system can desensitize its outputs to errors in its inputs. This property of feedback motivates the work previously described on fusing measurements from various sensors to replace the loss of information normally provided by a failed sensor such as a rate gyroscope. However, when problems occur on spacecraft, a feedback control design can have an undesirable effect, inhibiting methods of problem correction [58].

## **7. Gyroless Attitude Control: Open-Loop**

Another approach for maneuvering in the presence of feedback sensor failures is to operate the spacecraft in the open-loop. Performing an open-loop reorientation maneuver is, however, very risky due to the presence of uncertainty in the modeled spacecraft dynamics. Even with a reasonable knowledge of the spacecraft parameters, the targeting error associated with an open-loop maneuver can be large. The large terminal errors may prevent handover to a fine pointing control mode. On the other hand, if uncertainty is properly managed in an open-loop framework, then it may be possible to perform an open-loop reorientation maneuver in such a way that handover to fine pointing control occurs and collection of scientific data continues.

A prime example of on-orbit gyroless open-loop attitude control (the only one the author has been able to find) is the ‘dead-reckoning’ maneuver implemented on FUSE. Using the best rate, vehicle dynamics and torque environment estimates available, <5 deg maneuvers were successfully completed with better than 90% accuracy which allowed Fine Error Sensor (FES) software to take over to further reduce the attitude error [26]. The success of the open-loop FUSE maneuver was limited in its implementation—less than

five degrees and only in a situation when there was no better alternative—but demonstrated that a gyroless open-loop attitude control solution is possible.

The idea that an open-loop, gyroless control solution is possible is the motivation for the work contained in this dissertation. If a gyroless solution is possible in small angle situations, what limitations are there on using it for large angle maneuvers? Is terminal error the only limitation? How can terminal error be minimized?

One approach for minimizing uncertainty, such as terminal error, in an open-loop framework was proposed in a paper titled “Unscented Optimal Control for Space Flight” by I. Michael Ross, Ronald Proulx and Mark Karpenko [152]. This paper proposed a proof-of-concept for gyroless (zero-gyro) operation of the Hubble Space Telescope using a rigid-body as the spacecraft model. Standard optimal control theory was combined with a nonlinear filtering approach to reduce problem size; this combination was later referred to as “Unscented Guidance” in a paper by I. Michael Ross, Ronald Proulx and Mark Karpenko [153]. The nonlinear filtering approach was first introduced by Simon Julier, Jeffrey Uhlmann and Hugh Durrant-Whyte in a 1995 paper titled “A New Approach for Filtering Nonlinear Systems” and was later referred to as the “Unscented Transform” [154-155]. The objective of the unscented guidance approach is to produce an optimal control trajectory for a spacecraft that maneuvers from an initial state to a final state. The optimal control trajectory achieves the final state while simultaneously minimizing a desired parameter such as time or position error.

The “Unscented Optimal Control for Space Flight” paper proposed that using an unscented guidance method may provide a viable approach to continue spacecraft large-angle maneuvers in the absence of feedback which allows science operations to continue [152]. This paper, however, modeled the spacecraft as a simple rigid-body without explicitly considering the dynamics of the reaction wheels. Thus, it remains unclear if unscented guidance would be feasible on a practical reaction wheel spacecraft.

This dissertation explores unscented guidance as a means to design a gyroless open-loop attitude control method that utilizes reaction wheels to perform large-angle maneuvers. This gyroless open-loop large-angle capable control method could be used on

any spacecraft that contains reaction wheels, as a backup mode in case of hardware failure on highly capable spacecraft which would extend their life or as a low-cost full-time mode on a small spacecraft.

### **C. CONTRIBUTIONS OF THIS DISSERTATION**

As spacecraft attitude control components fail, mission engineers regain control through various and sometimes elaborate methods. These methods differ among spacecraft, and each is unique due to the combination of spacecraft component, mission, and solution affordability that each situation confers. Existing methods operate in closed-loop environments and there are currently no methods that operate exclusively in an open-loop environment. Development of a mission-extending concept that maintains control of the reaction-wheel-based spacecraft while minimizing both position and angular rate error in an uncertain, open-loop environment would provide additional scientific data and a greater return on the dollars invested.

Previous papers describing an open-loop concept showed as a proof-of-concept that it is possible to accurately reorient a rigid-body spacecraft in the presence of uncertainty and in the absence of sensor feedback using a concept called unscented guidance [152-153]. As part of the original work shown in this dissertation, a paper titled “Unscented Guidance for Zero-Feedback Reaction Wheel Slews” described unscented guidance for point-to-point reaction wheel maneuvers for a satellite with an arbitrary momentum bias [156]. This paper extended the rigid-body idea to a more realistic spacecraft model that includes reaction wheel actuators. The original work was further extended in a paper titled “Optimum Momentum Bias for Zero-Feedback Reaction Wheel Slews” [157] by exploring the relationship between momentum bias magnitude and terminal accuracy, and an optimum bias for performing an unscented reaction wheel attitude maneuver was found. Additionally, it was found that non-zero momentum bias is a necessary condition for a solution to an open-loop, rest-to-rest large-angle maneuver using reaction wheels. The initial momentum is incorporated in the problem formulation as an additional optimization parameter. This is because the magnitude and direction of the momentum bias influences



the non-linear dynamic coupling. Finding the ideal momentum bias for a given maneuver is, however, a non-trivial problem.

This dissertation presents an open-loop method to minimize error for a reaction-wheel-based spacecraft using optimal control techniques such that a large-angle maneuver is performed with accuracy sufficient for handing off fine pointing to fine-guidance sensors (FGS). To solve this problem, this dissertation develops equations of motion, defines representative spacecraft parameters, creates the unscented reaction wheel maneuver algorithm, and solves various versions of the problem. Unscented reaction wheel maneuvers with arbitrary momentum bias and with optimum momentum bias are solved to quantify the level of improvement in the final error that this algorithm provides [156-157]. This open-loop method is a novel and practical contribution to the body of knowledge.

#### **D. DISSERTATION OUTLINE**

Chapter II reviews some optimal control concepts that can be used to solve nonlinear optimization problems. Optimal control with uncertain parameters is introduced. Discussion includes sampling methods such as Monte Carlo, Multidimensional Approximation and Unscented Guidance [153], [158]. Ernst Zermelo's shortest time vehicle steering problem in a wind vector field is used to illustrate concepts [159]. A semi-discrete Lebesgue-Stieltjes version of the Zermelo problem is solved for comparison with the deterministic version. These results are a reproduction of previous work [153] to illustrate the concept. Analysis and discussion of results follow including applicability to the unscented reaction wheel maneuver problem.

Chapter III reviews concepts for conventional reaction-wheel attitude control. Definitions for the representative spacecraft, quaternions, equations of motion and quaternion error feedback are reviewed. Open-loop kinematic profiles are developed to establish the baseline performance of open-loop maneuvers. Results are provided for a closed-loop attitude control maneuver and open-loop based on the kinematic profile maneuver. Open-loop results are discussed for both single-axis and three-axes of inertia tensor uncertainty. Results are reviewed and a discussion regarding why open-loop solutions are generally not practical is provided.

Chapter IV formulates an unscented reaction wheel maneuver nonlinear optimal control problem for solving a cost functional. The unscented reaction wheel maneuver problem cost functional is based on the concept of mean squared error. Necessary conditions for this problem are defined both for the case of arbitrary momentum bias and for the case of optimum momentum bias.

Chapter V provides results for the unscented reaction wheel maneuver nonlinear optimal control problem. Single-axis and three-axes of uncertainty with arbitrary momentum bias results are provided. These results show that an unscented reaction wheel maneuver provides final error comparable to a closed-loop solution and hint at perhaps an even better solution if momentum bias is simultaneously optimized [156]. An unscented reaction wheel maneuver including simultaneous optimization of momentum bias for both single-axis and three-axis uncertainty further improves the solution which results in less final average error than the comparable closed-loop solution [157].

Chapter VI provides conclusions and thoughts regarding future work which are included for completeness and to inspire future work in this valuable area of research.

THIS PAGE INTENTIONALLY LEFT BLANK

## II. OPTIMAL CONTROL BACKGROUND

The earliest examples of optimization theory date from the time of Ancient Greeks [160-161]. One example demonstrates that a circle is the shape that maximizes the area inside a perimeter, as shown by Queen Dido. Through the 1600–1700s, dynamic optimization theory problems were popular with academics, and many weighed in on the topic including Bernoulli, Newton, Leibniz, and Euler [160], [162-164]. The problems that were posed at this time were focused on the interconnectedness of time and motion—Newton’s laws of motion were first published in 1687. Regarding the optimization of time coupled with motion, Bernoulli’s Brachistochrone example is a good one—is a straight line the fastest way to get to a destination? Under certain conditions, it’s not.

In the 1950s, optimization theory and optimal control theory developed as scientists sought new methods to control spacecraft [161]. The calculus of variations was an established method for solving optimization problems in the 1950s and continues to be widely used. However, the calculus of variations has limitations on what problems it can solve—it cannot be used to solve many optimal control problems. This is because the calculus of variations assumes there are no constraints on the value of the control variable (and originally did not include the existence of a control variable), but in optimal control of physical systems, control variable constraints, such as for finite amounts of thrust, are commonplace [161], [164]. Lev Pontryagin and his students formulated a way to work with these constraints and obtain an optimal control solution. They produced a wealth of work in this area including a rigorous proof of the theorem of optimal control called: Pontryagin’s maximum principle [160-161], [164].

The idea underlying all optimal control problems is that of a “control function that minimizes a performance measure,” which is a mathematical functional [160]. What the control function is and what performance measures it is desired to minimize are unique to each problem. Moreover, each problem can be part of a landscape of optimal control problems, so users must explore carefully. A commonality among these problems is that their results are often not intuitive—there are few straight lines. This non-intuitive nature

makes optimal control problems both difficult to solve and to comprehend. Thankfully, computers help with both.

The control function is chosen by the user and can have many values. A standard optimal control problem seeks a control trajectory,  $\mathbf{u}$ , that both shapes and controls the function such that a performance measure is minimized [160], [164]. The standard optimal control problem defined here is a Bolza-type problem [164]. It has a cost functional comprised of the endpoint, or Mayer, cost which is shown as  $E$  in the problem formulation, and the running, or Lagrange, cost which is shown as  $F$ . This cost functional is to be minimized—final time is a common example. The minimization is subject to state variables,  $\mathbf{x}$ , the control trajectory,  $\mathbf{u}$ , which are captured in the dynamics, and any initial or final endpoints including any constraints. Ross’s text “A Primer on Pontryagin’s Principle in Optimal Control” presents a standard optimal control problem of the Bolza-type that is reproduced here (1) [164]:

$$\left\{ \begin{array}{ll} \text{Minimize} & J[\mathbf{x}(\cdot), \mathbf{u}(\cdot), t_f] = E(\mathbf{x}(t_f), t_f) \\ & + \int_{t_0}^{t_f} F(\mathbf{x}(t), \mathbf{u}(t), t) dt & \text{cost} \\ \text{Subject to} & \dot{\mathbf{x}}(t) = \mathbf{f}(\mathbf{x}(t), \mathbf{u}(t), t) & \text{dynamics} \\ & \mathbf{x}(t_0) = \mathbf{x}^0 \\ & t_0 = t^0 & \text{endpoints} \\ & \mathbf{e}(\mathbf{x}_f, t_f) = \mathbf{0} \end{array} \right. \quad (1)$$

One example of a standard optimal control problem is a Zermelo minimum time problem. Ernst Zermelo first proposed the minimum time problem in his 1930 paper “Über die Navigation in der Luft als Problem der Variationsrechnung 1930c” reprinted in “Collected Works Vol. II Calculus of Variations, Applied Mathematics, and Physics” [159]. This problem describes the possible paths taken by an airship moving in a constant wind vector field—in later literature the airship is replaced by a boat and wind replaced with current—and has been used often as an example in optimal control [153], [163], [165-166]. This chapter uses the problem, reconstructed from previous work in [153], as an illustrative example to demonstrate how an optimal control problem is constructed, including how it is extended to include uncertainty. A solution to the optimal control

problem is presented through the development of Pontryagin's necessary conditions for optimality.

#### A. DETERMINISTIC ZERMELO MINIMUM-TIME PROBLEM

A deterministic function is one that, using specific inputs, returns the same result every time it is evaluated. In this sense, a deterministic function is one that produces a result that is not random. One version of a deterministic Zermelo problem ( $Z_D$ ) is constructed as a “standard” optimal control example problem, as shown in the Ross et al. paper titled “Unscented Guidance” [153]. Motion for this problem is constrained to the  $xy$ -plane, so the state solutions to the problem exist in  $\mathbb{R}^2$ . The cost to be minimized is time. Final time should be as small as possible, and this is defined in the top row of the problem formulation where final time is the variable to be minimized. Notice that there is no running cost,  $F$ , associated with this problem, only a cost,  $E$ , at time final which is consistent with a Mayer-type optimal control problem. The dynamics refer to a ship steering with constant wind. The start position is  $x_0 = 2.25, y_0 = 1.0$ , at initial time = 0 sec., and the final position, at time final,  $t_f$ , is  $x_f = 0$  and  $y_f = 0$ . This Zermelo problem is reproduced here [153]:

$$\begin{aligned}
 \mathbf{x} &:= (x, y) \in \mathbb{R}^2 \\
 \mathbf{u} \in \mathbb{U} &:= \{(u_1, u_2) \in \mathbb{R}^2 : u_1^2 + u_2^2 = 1\} \\
 \mathbf{p} &:= (p, q) = (1, -1) \in \mathbb{R}^2 \\
 (Z_D) &\left\{ \begin{array}{l} \text{Minimize } J[\mathbf{x}(\cdot), \mathbf{u}(\cdot), t_f] := t_f \\ \text{Subject to } \dot{x}(t) = py(t) + u_1(t) \\ \quad \dot{y}(t) = qx(t) + u_2(t) \\ \quad (\mathbf{x}(t_0), t_0) = (2.25, 1, 0) \\ \quad \mathbf{x}(t_f) = \mathbf{0} \end{array} \right\} \tag{2}
 \end{aligned}$$

where the ship steering vector normalized by ship speed is  $\mathbf{u} = (u_1, u_2)$  and the wind vector field is  $\mathbf{p} = (p, q)$ .

A verification and validation of any candidate optimal control solution must be performed. A set of necessary conditions that a candidate optimal control solution to the  $Z_D$  problem (2) must satisfy is found by developing Pontryagin's necessary conditions for optimality [164]. The necessary conditions are derived as follows:

1. Construct the Hamiltonian
2. Develop the Adjoint equations
3. Minimize the Hamiltonian
4. Construct the Endpoint Lagrangian
5. Determine transversality conditions
6. Evaluate the Hamiltonian value condition
7. Analyze the Hamiltonian evolution equation

### **Construct the Hamiltonian**

The problem formulation defines the following state vector in primal space:

$$\mathbf{x} \in \mathbb{R}^2$$

A common unit of measure is needed, and this unit is defined as  $\lambda$  for the control Hamiltonian. The problem of measuring a sandwich may define  $\lambda$  as calories, ounces, or dollars for a common unit of measure [164]. The  $\lambda$  cost unit is defined for measurement of the control Hamiltonian, and it follows for the deterministic Zermelo problem that this adjoint co-vector exists in the same dimension but in dual space:

$$\lambda \in \mathbb{R}^2$$

The adjoint co-vector for the deterministic Zermelo problem is defined as:

$$\boldsymbol{\lambda} := \begin{bmatrix} \lambda_x \\ \lambda_y \end{bmatrix}$$

The control Hamiltonian equation is defined as the following:

$$H(\boldsymbol{\lambda}, \mathbf{x}, \mathbf{u}, t) := F(\mathbf{x}, \mathbf{u}, t) + \boldsymbol{\lambda}^T \mathbf{f}(\mathbf{x}, \mathbf{u}, t) \quad (3)$$

For the deterministic Zermelo problem, there is no running cost,  $F$ , associated with this problem or:

$$F(\mathbf{x}, \mathbf{u}, t) = \mathbf{0}$$

The cost co-vector transpose is defined as:

$$\boldsymbol{\lambda}^T = \begin{bmatrix} \lambda_x & \lambda_y \end{bmatrix}$$

The dynamics are given by:

$$\mathbf{f} = \begin{bmatrix} py(t) + u_1(t) \\ qx(t) + u_2(t) \end{bmatrix}$$

The deterministic Zermelo Hamiltonian equation is then given by:

$$H(\boldsymbol{\lambda}, \mathbf{x}, \mathbf{u}, t) := 0 + \begin{bmatrix} \lambda_x & \lambda_y \end{bmatrix} \begin{bmatrix} py(t) + u_1(t) \\ qx(t) + u_2(t) \end{bmatrix} = \lambda_x (py(t) + u_1(t)) + \lambda_y (qx(t) + u_2(t)) \quad (4)$$

This equation can be re-written using  $p = 1$  and  $q = -1$  as defined in the problem statement:

$$H(\boldsymbol{\lambda}, \mathbf{x}, \mathbf{u}, t) = \lambda_x y(t) - \lambda_y x(t) + \lambda_x u_1(t) + \lambda_y u_2(t)$$

Because this problem also has a control constraint, the Lagrangian of the Hamiltonian ( $\bar{H}$ ) must be used. The Lagrangian of the Hamiltonian equation is defined as:



$$\bar{H}(\boldsymbol{\mu}, \boldsymbol{\lambda}, \mathbf{x}, \mathbf{u}, t) := H(\boldsymbol{\lambda}, \mathbf{x}, \mathbf{u}, t) + \boldsymbol{\mu}^T \mathbf{h}(\mathbf{u}) \quad (5)$$

The  $\mu$  units are defined for consistent measurement of the Lagrangian of the Hamiltonian (5). The transpose of the path co-vector ( $\mu$ ) is defined as:

$$\boldsymbol{\mu}^T = [\mu]$$

The path function,  $h$ , uses the path constraint:

$$\mathbf{h}(\mathbf{u}, t) = u_1(t)^2 + u_2(t)^2$$

Which allows the  $Z_D$  Lagrangian of the Hamiltonian to be rewritten as:

$$\bar{H}(\boldsymbol{\mu}, \boldsymbol{\lambda}, \mathbf{x}, \mathbf{u}, t) := \lambda_x y(t) - \lambda_y x(t) + \lambda_x u_1(t) + \lambda_y u_2(t) + \mu(u_1(t)^2 + u_2(t)^2) \quad (6)$$

### Develop the adjoint equations

The  $Z_D$  adjoint equations are found by taking the partial derivative of the control Hamiltonian (4) with respect to the state variables:

$$-\dot{\lambda}_x := \frac{\partial H}{\partial x} = -\lambda_y \quad (7)$$

$$-\dot{\lambda}_y := \frac{\partial H}{\partial y} = \lambda_x \quad (8)$$

### Minimize the Hamiltonian

Pontryagin's Principle requires that the Hamiltonian (3) be minimized at each instant of time for the deterministic Zermelo's time-varying control space [164]. To meet this requirement, the deterministic Zermelo problem must meet a combination of stationarity and complementarity conditions. The stationarity condition is:

$$\frac{\partial \bar{H}}{\partial \mathbf{u}} = \frac{\partial H}{\partial \mathbf{u}} + \left( \frac{\partial \mathbf{h}}{\partial \mathbf{u}} \right)^T \boldsymbol{\mu} = 0 \quad (9)$$

The complementarity condition is:

$$\mu_i \begin{cases} \leq 0 & \text{if } h_i(\mathbf{u}, t) = h_i^L(t) \\ = 0 & \text{if } h_i^L(t) < (h_i(\mathbf{u}, t)) < h_i^U(t) \\ \geq 0 & \text{if } h_i(\mathbf{u}, t) = h_i^U(t) \\ \text{unrestricted} & \text{if } h_i^L(t) = h_i^U(t) \end{cases} \quad (10)$$

The stationarity condition is now applied to the deterministic Zermelo problem such that the partial derivative of  $\bar{H}$  with respect to  $\mathbf{u}$  is set equal to zero:

$$\frac{\partial \bar{H}}{\partial u_1} = \lambda_x + 2\mu u_1 = 0 \quad (11)$$

$$\frac{\partial \bar{H}}{\partial u_2} = \lambda_y + 2\mu u_2 = 0 \quad (12)$$

Then the complementarity condition is applied, which provides information about the behavior of the path co-vector. This results in  $\mu$  being unrestricted because:

$$1 \leq u_1^2 + u_2^2 \leq 1 \quad (13)$$

is an equality constraint.

### Construct the Endpoint Lagrangian

The deterministic Zermelo problem is in the Mayer form, with final time the objective. Endpoint boundary conditions must be evaluated at final time using the transversality conditions, minimized Hamiltonian, the Hamiltonian value condition, and the Hamiltonian evolution equation. The Endpoint Lagrangian equation is constructed to evaluate these conditions.

The endpoint Lagrangian equation is defined as:

$$\bar{E}(\mathbf{v}, \mathbf{x}_f, t_f) := E(\mathbf{x}_f, t_f) + \mathbf{v}^T \mathbf{e}(\mathbf{x}_f, t_f) \quad (14)$$

This equation partially depends on the endpoint function which is defined as the following:

$$\mathbf{e}(\mathbf{x}_f, t_f) := \begin{bmatrix} x_f - 0 \\ y_f - 0 \end{bmatrix} = \mathbf{0}$$

The  $v$  co-variables are defined for measurement of the endpoint Lagrangian. The transpose of the endpoint co-vector ( $v$ ) is defined as:

$$v^T = \begin{bmatrix} v_1 & v_2 \end{bmatrix}$$

For the deterministic Zermelo problem, the endpoint Lagrangian equation becomes:

$$\bar{E}(\mathbf{v}, \mathbf{x}_f, t_f) := t_f + \begin{bmatrix} v_1 & v_2 \end{bmatrix} \begin{bmatrix} x_f \\ y_f \end{bmatrix} = t_f + v_1 x_f + v_2 y_f \quad (15)$$

### Determine the transversality conditions

Transversality conditions are found by taking the partial derivative of the Endpoint Lagrangian ( $\bar{E}$ ) with respect to the final positions of the state vectors, or more generally, the terminal state:

$$\begin{aligned} \lambda_x(t_f) &:= \frac{\partial \bar{E}}{\partial x_f} = v_1 \\ \lambda_y(t_f) &:= \frac{\partial \bar{E}}{\partial y_f} = v_2 \end{aligned} \quad (16)$$

These terms give us unknowns in terms of other unknowns, so no new useful information is provided.

### Hamiltonian value condition

The minimized Hamiltonian is called the lower Hamiltonian which is denoted by  $\mathcal{H}$ . The lower Hamiltonian at final time is equivalent to the negative of the partial

derivative of the endpoint Lagrangian ( $\bar{E}$ ) (14) taken with respect to final time. Evaluating this partial derivative is known as the Hamiltonian value condition [164]. The deterministic Zermelo problem yields the following Hamiltonian value condition:

$$\mathcal{H}[\textcircled{t}_f] = -\frac{\partial \bar{E}}{\partial t_f} = 1 \quad (17)$$

This equation can be rewritten as:

$$\mathcal{H}[\textcircled{t}_f] = -1$$

where the constant Hamiltonian value of -1 is standard for minimum time problems.

### **Hamiltonian evolution equation**

The derivative of the lower Hamiltonian with respect to time is equivalent to the partial derivative of the Lagrangian of the Hamiltonian with respect to time. The deterministic Zermelo problem yields the following Hamiltonian evolution equation:

$$\frac{d\mathcal{H}}{dt} = \frac{\partial \bar{H}}{\partial t} = 0 \quad (18)$$

This equation tells us that the value of the lower Hamiltonian will be a constant with respect to time.

### **Review of Necessary Conditions**

The Hamiltonian and the Lagrangian of the Hamiltonian, (4) and (6), were found for the deterministic Zermelo problem. The Hamiltonian offered no insight to the problem, but the Lagrangian of the Hamiltonian provided more information. The Lagrangian of the Hamiltonian was evaluated using both the complementarity and stationarity conditions, (9) and (10). The complementarity condition, when applied to the deterministic Zermelo problem, resulted in the path co-vector,  $\mu$ , being unrestricted (13). The stationarity condition provided equations that relate the adjoint co-vectors to the path co-vector and

control solutions (11) and (12). These equations will be used to validate the control solution results shown later in this section. In addition, the adjoint co-vectors (7) and (8) must meet requirements imposed on their derivatives such that the derivative of  $\lambda_x$  is equivalent to  $\lambda_y$  and the derivative of  $\lambda_y$  is equal to  $-\lambda_x$  as required by the transversality equations (16). The Endpoint Lagrangian was developed to provide evaluation of transversality conditions, the Hamiltonian value condition, and the Hamiltonian evolution equation (15). Transversality conditions were evaluated but no new information was provided. The Hamiltonian value condition was evaluated for the deterministic Zermelo problem and showed that the value of the lower Hamiltonian was a constant of -1 (17). This value is consistent with the literature regarding minimum-time problems. Evaluation of the Hamiltonian evolution equation for the deterministic Zermelo problem stipulated that the value of the lower Hamiltonian be a constant, and the result of -1 meets that expectation (18).

With knowledge of these necessary conditions, a candidate control solution (both  $u_1$  and  $u_2$ ) for the  $Z_D$  problem is found by using an optimal control solver. In this dissertation, the control history is obtained using DIDO, the MATLAB toolbox for solving optimal control problems [167]. Figure 1 shows the candidate control solutions for  $u_1$  and  $u_2$ .

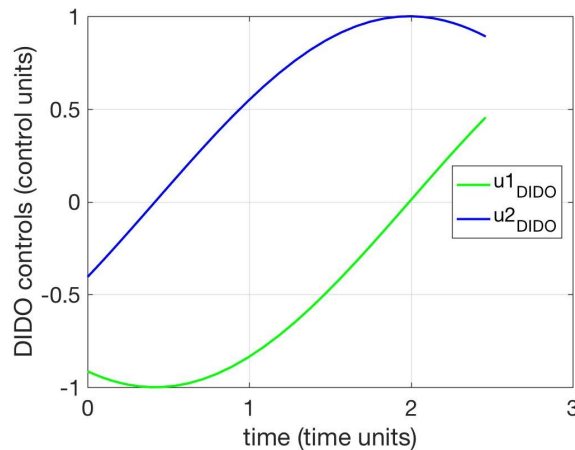


Figure 1. Solution of the Deterministic Zermelo Problem: Optimal Control Versus Time

The optimal trajectory,  $y$ -position vs.  $x$ -position, is shown in Figure 2 and as is seen, the time-optimal trajectory is not a straight line. This view of the  $x$  and  $y$  positions makes it easy to visualize a boat moving on the surface of the water from one location to another, in this case from an initial position of (2.25, 1) to a final position of (0, 0).

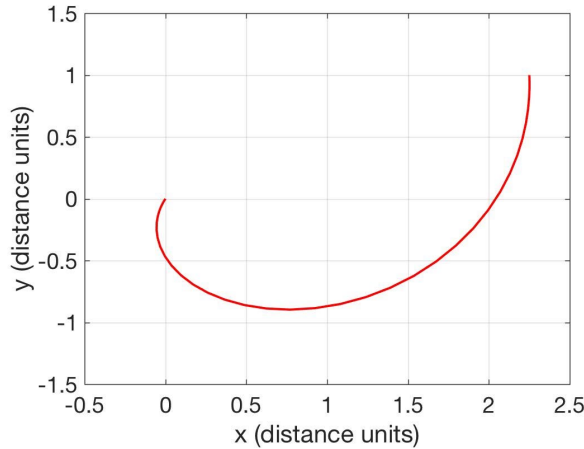


Figure 2. Solution of the Deterministic Zermelo Problem: Optimal Position  $y$  Versus  $x$

For this deterministic Zermelo optimal control problem, Hamiltonian, co-states (adjoint and path co-vectors) and path constraint are reviewed as an indication of solution optimality. These necessary conditions derivations must hold for the candidate solution to be considered an optimal solution. As a part of the necessary conditions derivations, evaluation of the Hamiltonian value condition stipulated that the minimized Hamiltonian would be a constant value of -1 which is consistent with a minimum time problem. Indeed, as seen in Figure 3, the candidate solution does have a minimized Hamiltonian value close to -1. Figures 4 and 5 show that control and co-state pairs are the same function scaled by -1. This knowledge can be used to re-visit the stationarity condition that produced the following equations (11) and (12) that are reprinted here for clarity:

$$\frac{\partial \bar{H}}{\partial u_1} = \lambda_x + 2\mu u_1 = 0$$

$$\frac{\partial \bar{H}}{\partial u_2} = \lambda_y + 2\mu u_2 = 0$$

Substitution of the co-state variable by the negative of the control variable in either equation yields a  $\mu$  value of  $1/2$ . Figure 6 shows that the value of the path co-vector,  $\mu$ , is  $1/2$  for all time.

A path constraint was imposed on the problem such that  $u_1^2 + u_2^2 = 1$ . Figure 7 shows that this constraint was met as the value of the path function is 1 for all time.

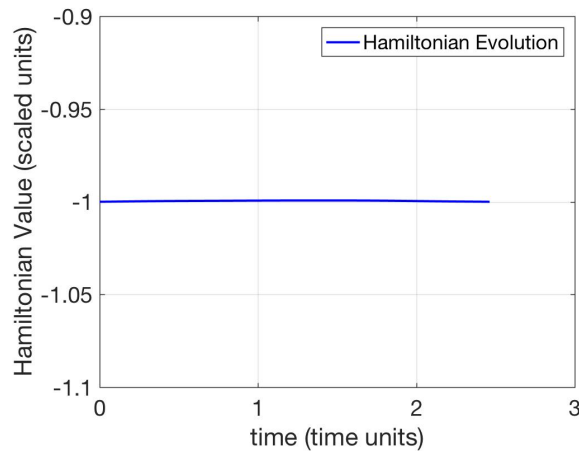


Figure 3. Solution of the Deterministic Zermelo Problem: Optimal Hamiltonian Versus Time

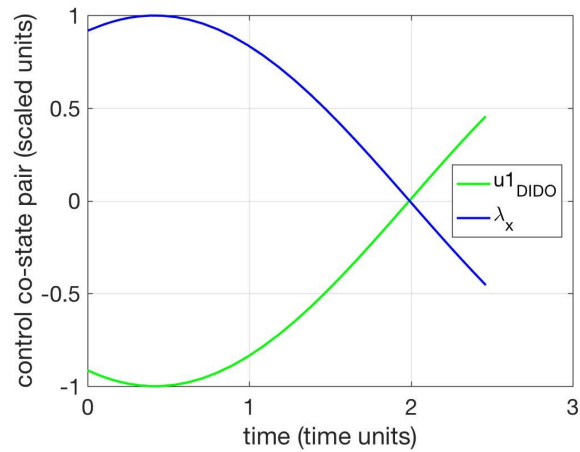


Figure 4. Solution of the Deterministic Zermelo Problem: Optimal Control  $u_1$  and Co-State  $\lambda_x$  Pair Versus Time

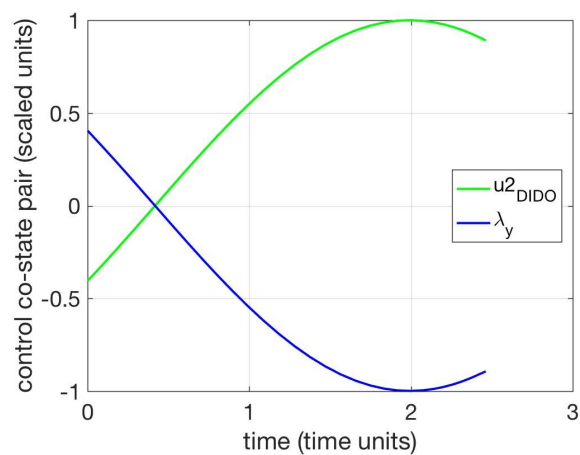


Figure 5. Solution of the Deterministic Zermelo Problem: Optimal Control  $u_2$  and Co-State  $\lambda_y$  Pair Versus Time



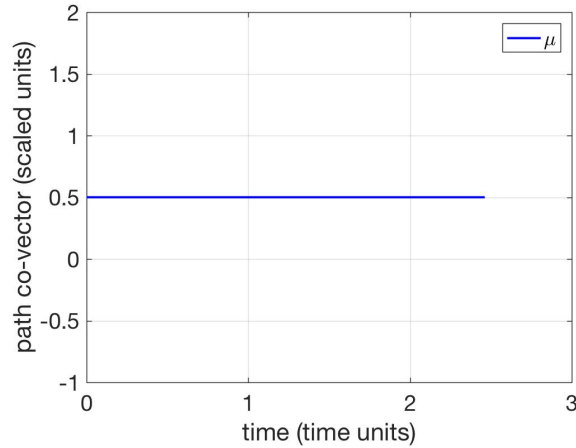


Figure 6. Solution of the Deterministic Zermelo Problem: Optimal Path Co-Vector Versus Time

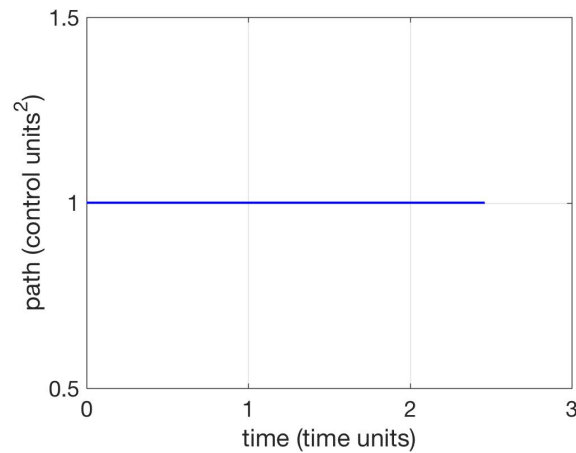


Figure 7. Solution of the Deterministic Zermelo Problem: Constraint Path Versus Time

As a final test of the candidate control solution, a propagation test was performed. This test takes the candidate control solutions,  $u_1$  and  $u_2$ , then uses a MATLAB numerical integrator to produce a position solution in the  $xy$ -plane. The “goodness” of the candidate control solutions can be evaluated based on how close the propagated position results come to the optimal results [164]. Figure 8 shows that propagation of this set of candidate control solutions provides a result that is similar to the optimal result shown in Figure 2. The shape of the curves for both result sets are similar, but the propagated figure shows a final position

that is offset approximately  $(0.06, -0.38)$  from the desired position of  $(0, 0)$ . This error is to be expected as an artifact of the interpolation and numerical integration of the control and so the propagated result shows that the optimal solution is reasonable.

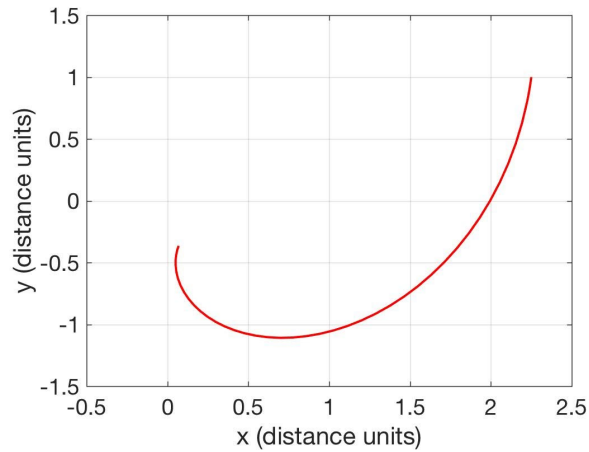


Figure 8. Solution of the Deterministic Zermelo Problem:  
Propagation Test  $y$  Versus  $x$

Due to the predicted Hamiltonian, co-states, path constraint, and propagation test results meeting expectations, this candidate optimal control solution is considered an optimal solution to the  $Z_D$  problem.

## B. OPTIMAL CONTROL WITH UNCERTAIN PARAMETERS

Nonlinear optimal control problems that include parameter uncertainty are a “particularly challenging” subset of optimal control problems [168]. There is substantial interest in solving problems with inherent uncertainty as they are numerous and broadly apply to areas such as spacecraft dynamics, aircraft routing, combat modelling, and management science [169-171]. The main challenge in solving this subset of optimal control problems is the existence of a solution [164].

This section presents an introduction to optimal control problems with parameter uncertainty, including various methods that may be used to solve these problems. The Zermelo minimum-time problem is adapted such that the wind becomes an uncertain

parameter [172]. This adaptation changes the cost functional from minimum time to minimum error at the desired final position. A set of necessary conditions that a candidate optimal control solution must satisfy is found and results are reviewed.

## 1. Introduction to Optimal Control with Parameter Uncertainty

A deterministic optimal control problem may be written in a Mayer form as [164], [172-175]:

$$(D) \left\{ \begin{array}{ll} \text{Minimize} & J_{det}[\mathbf{x}(\cdot), \mathbf{u}(\cdot), t_f] \quad \doteq E(\mathbf{x}(t_f), t_f) \\ \text{Subject to} & \dot{\mathbf{x}}(t) = \mathbf{f}(\mathbf{x}(t), \mathbf{u}(t), t) \\ & (\mathbf{x}(t_0), t_0) = (\mathbf{x}^0, t^0) \\ & \mathbf{e}(\mathbf{x}(t_f), t_f) \leq \mathbf{0} \\ & \mathbf{h}(\mathbf{x}(t), t) \leq \mathbf{0} \end{array} \right\}$$

where  $J_{det}$  is a deterministic cost functional defined by the Mayer (endpoint) cost,  $E$ . The vector function,  $\mathbf{f}$ , contains the problem dynamics. Vector functions,  $\mathbf{e}$  and  $\mathbf{h}$ , are the endpoint constraint function and path constraint function, respectively.

This problem may be subject to an uncertain parameter,  $\mathbf{p}$ , such as a wind vector field or water current. Consider the state-space dynamics of a system with uncertain parameter  $\mathbf{p}$ :

$$\mathbf{p} \in \mathbb{R}^2$$

$$\dot{\mathbf{x}} = \mathbf{f}(\mathbf{x}, \mathbf{u}, t; \mathbf{p})$$

where vector function  $\mathbf{f}$  is the dynamics function. The dynamics are deterministic if the values for  $\mathbf{p}$  are known, as was demonstrated in the deterministic Zermelo problem where  $\mathbf{p} = (1, -1)$  for the specific values of  $\mathbf{p}$  selected. Given control trajectory,  $\mathbf{u}(t)$ , we obtain  $\mathbf{x}(t, \mathbf{p})$  as the solution to this dynamics system. Following standard practice in control systems design, values for uncertain  $\mathbf{p}$  may be selected as some “nominal”  $\mathbf{p} \in \text{supp}(\mathbf{p})$ , where  $\text{supp}(\cdot)$  denotes the support of a statistical distribution, e.g. Gaussian, uniform, etc. [151], [176]. The Mayer cost may be defined, for example, in terms of the terminal attitude or rate errors. However, the solution to the Mayer problem will only minimize the terminal

error for  $\mathbf{p}$  and not necessarily over  $\text{supp}(\mathbf{p})$  because  $\mathbf{p}$  is uncertain. What is desired is to minimize the cost functional over  $\text{supp}(\mathbf{p})$ , but this is not straightforward due to  $\mathbf{p}$  being an uncertain parameter. To resolve this issue, define a new cost functional with an explicit dependence on  $\mathbf{p}$  [172], [174-175]:

$$J_p[\mathbf{x}(\cdot, \mathbf{p}), \mathbf{u}(\cdot), t_f; \mathbf{p}] := E_p(\mathbf{x}(t_f, \mathbf{p}), t_f; \mathbf{p}) \quad (19)$$

However,  $J_p$  (19) cannot be minimized due to its dependence on uncertain  $\mathbf{p}$ . Recognizing that  $\mathbf{p}$  is a scalar function in the real domain, a cost functional  $J$  can be created by integrating  $J_p$  over the support of  $\mathbf{p}$ . This equation is written in terms of a Lebesgue-Stieltjes integral [172], [174-175]:

$$J[\mathbf{x}(\cdot, \cdot), \mathbf{u}(\cdot), t_f] := \int_{\text{supp}(\mathbf{p})} J_p[\mathbf{x}(\cdot, \mathbf{p}), \mathbf{u}(\cdot), t_f; \mathbf{p}] dm(\mathbf{p}) \quad (20)$$

where the cost functional  $J$  is defined as an  $N_p$ -dimensional integral over  $\text{supp}(\mathbf{p})$ . Formulation of the problem in terms of a Lebesgue-Stieltjes integral (20) allows a measure function,  $m$ , to be chosen as the joint cumulative distribution function (CDF) of  $\mathbf{p}$  [31], [153], [172], [174-175]. As mentioned previously, this distribution can take many forms, including Gaussian or uniform distributions, as defined by the user [151], [176].

Using the Lebesgue-Stieltjes integral, the standard Mayer optimal control problem is re-cast as a Lebesgue-Stieltjes optimal control problem [172], [174-175]:

$$(LS) \left\{ \begin{array}{ll} \text{Minimize} & J[\mathbf{x}(\cdot, \cdot), \mathbf{u}(\cdot), t_f] := \int_{\text{supp}(\mathbf{p})} J_p[\mathbf{x}(\cdot, \mathbf{p}), \mathbf{u}(\cdot), t_f; \mathbf{p}] dm(\mathbf{p}) \\ \text{Subject to} & \dot{\mathbf{x}}(t, \mathbf{p}) = \mathbf{f}(\mathbf{x}(t, \mathbf{p}), \mathbf{u}(t), t; \mathbf{p}) \\ & (\mathbf{x}(t_0, \mathbf{p}), t_0) = (\mathbf{x}^0, t^0) \\ & \mathbf{e}(\mathbf{x}(t_f, \mathbf{p}), t_f; \mathbf{p}) \leq \mathbf{0} \\ & \mathbf{h}(\mathbf{x}(t, \mathbf{p}), t; \mathbf{p}) \leq \mathbf{0} \\ & \mathbf{p} \in \text{supp}(\mathbf{p}) \end{array} \right.$$

In a deterministic optimal control problem, the objective is to determine one state-control function pair  $(\mathbf{u}(\cdot), \mathbf{x}(\cdot))$  that minimizes the Bolza cost functional. In the Lebesgue-Stieltjes optimal control problem, the objective is to determine the function-tube pair,

$(\mathbf{u}(\cdot), \mathbf{x}(\cdot, \cdot)) := (\mathbf{u}(\cdot), \{\mathbf{x}(\cdot, \mathbf{p}) : \mathbf{p} \in \text{supp}(\mathbf{p})\})$ , that minimizes the Lebesgue-Stieltjes cost functional and further satisfies the constraints for all  $t \in [t_0, t_f]$  and all  $\mathbf{p} \in \text{supp}(\mathbf{p})$ . The “tube” in this sense is defined by the CDF and statistically limits the possible function or functions that can minimize the cost. The Lebesgue-Stieltjes optimal control problem thus demands that all conditions associated with the original problem be satisfied for all values of  $\mathbf{p} \in \text{supp}(\mathbf{p})$  by a single control trajectory,  $\mathbf{u}(t)$ . This suggests that uncertainty can be completely managed without feedback. Note that a solution to this “stringent” problem may not exist.

## 2. Semi-Discrete Lebesgue-Stieltjes

Evaluation of the Lebesgue-Stieltjes integral may be done using any suitable cubature (numerical computation of a multiple integral) scheme [175]:

$$\int_{\text{supp}(\mathbf{p})} J_p[\mathbf{x}(\cdot, \mathbf{p}), \mathbf{u}(\cdot), t_f; \mathbf{p}] d\mathbf{m}(\mathbf{p}) = \sum_{i=1}^n w_i J_p[\mathbf{x}(\cdot, \mathbf{p}_i), \mathbf{u}(\cdot), t_f; \mathbf{p}_i] \quad (21)$$

where  $(\mathbf{p}_i, w_i)$  for  $i = 1, 2, \dots, n$  is a collection of points and weights for sampling the support of  $\mathbf{p}$ . For finite  $n$ , a semi-discrete Lebesgue-Stieltjes optimal control problem is constructed by replacing the Lebesgue-Stieltjes integral (21) by its cubature [175]. The semi-discrete Lebesgue-Stieltjes optimal control problem is written in terms of a standard deterministic optimal control problem by assembling an ensemble of models for each cubature point as [175], [177-178]:

$$(LS^n) \left\{ \begin{array}{ll} \text{Minimize} & J_n[\mathbf{x}_1(\cdot, \cdot), \dots, \mathbf{x}_n(\cdot, \cdot), \mathbf{u}(\cdot), t_f] := \sum_{i=1}^n w_i J_p[\mathbf{x}(\cdot, \mathbf{p}_i), \mathbf{u}(\cdot), t_f; \mathbf{p}_i] \\ \text{Subject to} & \begin{array}{ll} \dot{\mathbf{x}}_1(t, \mathbf{p}_1) & = \mathbf{f}(\mathbf{x}_1(t, \mathbf{p}_1), \mathbf{u}(t), t_f; \mathbf{p}_1) \\ \vdots & \vdots \\ \dot{\mathbf{x}}_n(t, \mathbf{p}_n) & = \mathbf{f}(\mathbf{x}_n(t, \mathbf{p}_n), \mathbf{u}(t), t_f; \mathbf{p}_n) \\ (\mathbf{x}(t_0, \mathbf{p}_i), t_0) & = (\mathbf{x}^0, t^0) \\ \mathbf{e}(\mathbf{x}(t_f, \mathbf{p}_i), t_f; \mathbf{p}_i) & \leq \mathbf{0} \\ \mathbf{h}(\mathbf{x}(t, \mathbf{p}_i), t; \mathbf{p}_i) & \leq \mathbf{0} \\ \mathbf{p}_i & \in \text{supp}(\mathbf{p}) \forall i = 1, 2, \dots, n \end{array} \end{array} \right\}$$

Because this problem is a standard optimal control problem, it can, in theory, be solved using any suitable technique such as shooting, collocation, robust optimization, polynomial chaos, Monte Carlo, approximation, multidimensional approximation, Pseudospectral or unscented guidance [158], [168], [179-191]. This chapter discusses three sampling techniques: Monte Carlo, multidimensional approximation, and unscented guidance. This discussion is followed by a demonstration of the unscented guidance method using the frequently cited Zermelo minimum time problem [153], [159], [165-166].

### 3. Monte Carlo Sampling

National Aeronautics and Space Administration's (NASA) Independent Verification and Validation (IV&V) program states that "Monte Carlo (MC) simulation is the forefront class of computer-based numerical methods for carrying out precise, quantitative risk analyses of complex projects" [192]. The aerospace industry uses MC to verify and validate software that is used on aircraft, spacecraft, missiles, and more. Impacts of uncertain spacecraft parameters, such as spacecraft inertia, can be assessed by using a MC simulation. For Monte Carlo sampling, the cubature weights are  $w_i = 1/n$  for all  $i$  and the cubature nodes are random samples of the support of  $\mathbf{p}$ . By the law of large numbers [193], the cubature should be close to the expected value when the number,  $n$ , of Monte Carlo samples is large, e.g.,  $n = 1000$  or greater. The semi-discrete Lebesgue-Stieltjes problem formulation using 1000 Monte Carlo samples is re-written as:

$$(MC^n) \left\{ \begin{array}{ll} \text{Minimize} & J_n[\mathbf{x}_1(\cdot, \cdot), \dots, \mathbf{x}_n(\cdot, \cdot), \mathbf{u}(\cdot), t_f] := \frac{1}{1000} \sum_{i=1}^{n=1000} J_p[\mathbf{x}(\cdot, \mathbf{p}_i), \mathbf{u}(\cdot), t_f; \mathbf{p}_i] \\ \text{Subject to} & \mathbf{x}_1(t, \mathbf{p}_1) = \mathbf{f}(\mathbf{x}_1(t, \mathbf{p}_1), \mathbf{u}(t), t_f; \mathbf{p}_1) \\ & \vdots \\ & \mathbf{x}_{1000}(t, \mathbf{p}_{1000}) = \mathbf{f}(\mathbf{x}_{1000}(t, \mathbf{p}_{1000}), \mathbf{u}(t), t_f; \mathbf{p}_{1000}) \\ & (\mathbf{x}(t_0, \mathbf{p}_i), t_0) = (\mathbf{x}^0, t^0) \\ & \mathbf{e}(\mathbf{x}(t_f, \mathbf{p}_i), t_f; \mathbf{p}_i) \leq \mathbf{0} \\ & \mathbf{h}(\mathbf{x}(t, \mathbf{p}_i), t; \mathbf{p}_i) \leq \mathbf{0} \\ & \mathbf{p}_i \in \text{supp}(\mathbf{p}) \forall i = 1, 2, \dots, 1000 \end{array} \right.$$

It is apparent from the problem statement above that Monte Carlo sampling will generate a very large-scale optimal control problem.

#### 4. Multidimensional Approximation Sampling

Multidimensional approximation, also called GenOC in Kragelund's thesis "Optimal Sensor-Based Motion Planning for Autonomous Vehicle Teams," is a method for sampling an uncertain nonlinear optimal control problem developed by Claire Walton and described in her 2015 thesis titled "The Design and Implementation of Motion Planning Problems Given Parameter Uncertainty" [188], [194]. This method expands the approximation methods presented by Chris Phelps et al. in "Sample Average Approximations in Optimal Control of Uncertain Systems" and "Consistent Approximation of an Optimal Search Problem" and is similar to the multidimensional Pseudospectral method developed by Ruths and Li in "Multidimensional Pseudospectral Method for Optimal Control of Quantum Ensembles" [168], [184], [195]. Multidimensional approximation is a numerical algorithm for performing integrations of both space and time using any suitable optimal control solver(s). The ability to use a varied combination of optimal control solvers differentiates it from previous work by Ruths and Li that specified integrations over space and time using only Pseudospectral methods [187]. The multidimensional approximation method is well established and has been used in numerous publications. Its use has primarily addressed optimal control problems dealing with uncertain targets such as the case of finding a search trajectory (candidate solution path) that maximizes the probability of detecting an uncertain target [158], [168], [184], [190], [194]. The resulting optimal control problem is solved using SNOPT (a large-scale optimal non-linear problem (NLP) solver) to compute the numerical solution [196]. A Bolza-type problem formulation using multidimensional approximation sampling is written as [188]:

$$J^{MN} = \sum_{i=1}^M \alpha_i^M \left[ F(\bar{x}_i^{NN}, \omega_i^M) + \sum_{k=0}^N b_k^N r(\bar{x}_i^{Nk}, \bar{u}^{Nk}, t_k, \omega_i^M) \right] \quad (22)$$

This cost functional (22) has one finite set of nodes with weights,  $M$ , that discretizes the parameter space—set  $M$  has nodes  $\{\omega_i^M\}_{i=1}^M$  with associated weights  $\{\alpha_i^M\}_{i=1}^M$ . For

discretization over time, there is a finite set of grid points,  $N$ —set  $N$  has associated weights  $\{b_N^k\}_{k=0}^N$ . In this way, multidimensional approximation reduces the number of sampling points to something on the order of  $1e^1$  to  $1e^2$  versus a comparable Monte Carlo sampling that is on the order of  $1e^3$  or larger [158]. The multidimensional approximation method will not be used to solve the unscented reaction wheel maneuver nonlinear optimal control problem featured in this dissertation but could be considered for future research.

## 5. Unscented Sampling

To overcome the curse of dimensionality normally associated with cubature techniques [160], [164], [197], another sampling option is to take  $(\mathbf{p}_i, w_i)$  to be the sigma points (weighted sampling points) that are normally associated with the unscented Kalman filter [198-202]. The unscented transform was originally introduced by Julier et al. as a method to avoid linearization in nonlinear filtering under the idea that it is better to approximate a probability density function than to linearize a nonlinear function [154], [198-200], [203-206]. A combination of the concept of the unscented transform, as defined by Julier et al., with standard optimal control is the basis for unscented guidance [153], [172], [207].

In unscented guidance [153], the philosophy of approximation being better than linearization is followed to obtain a low-order semi-discretization of the Lebesgue-Stieltjes optimal control problem. The unscented guidance method results in a “tube” of potential solution-parameter paths for the system. This method reduces the overall number of calculations and still achieves the same or better statistical performance as a much larger random sampling method. In contrast to Monte Carlo sampling where  $n$  must be suitably large, the unscented transform uses a minimal number of cubature points to match statistical moments to a given order. For example, using the spherical simplex unscented transformation [155], only  $n = N_p + 2$  cubature points are needed which is on the order of  $1e^0$  [208]. The multidimensional approximation method also samples the problem space to achieve a solution using a small number of points. Due to the multidimensional problem setup, the number of points needed to achieve a solution will typically be larger than an unscented guidance method. For example, if three points are need for a solution using



unscented guidance, the comparable problem would require  $3 \times 3$  or nine points to sample the multidimensional problem space. The comparatively small number of points needed for unscented sampling generates a smaller-scale semi-discretization of the Lebesgue-Stieltjes optimal control problem. This problem is easily solved for an open-loop control trajectory,  $\mathbf{u}(t)$ , that manages the effects of parametric uncertainty. This method is an established approach to sampling nonlinear optimal control problems and has been featured in numerous publications [152-153], [156-157], [172], [209-211]. The Ross, Proulx & Karpenko paper titled “Unscented Optimal Control for Spaceflight” describes a proof-of-concept for a zero-gyro large-angle maneuver of a rigid-body that uses unscented guidance to reach a near-zero-mean-error final position solution [152].

The Zermelo minimum time problem is used here as an illustrative example to demonstrate how the unscented guidance approach is formulated [153], [172]. This example will show that a combination of an approximate probability distribution function (PDF) with optimal control software achieves a desired open-loop solution to a nonlinear optimal control problem with uncertainty.

## 6. A Semi-Discrete Lebesgue-Stieltjes Zermelo Problem

In this example, the deterministic Zermelo problem is developed into an uncertain one where the wind,  $\mathbf{p}$ , is the uncertain parameter [153], [172]. This uncertain Zermelo problem is then transformed into a semi-discrete Lebesgue-Stieltjes Zermelo problem that easily changes to an unscented guidance version of the problem. Results are included to illustrate statistical improvements.

The goal of the control solution for this uncertain problem is to determine a function-tube pair,  $(\mathbf{u}(\cdot), \mathbf{x}(\cdot, \cdot)) := (\mathbf{u}(\cdot), \{\mathbf{x}(\cdot, \mathbf{p}) : \mathbf{p} \in \text{supp}(\mathbf{p})\})$  that minimizes the user-defined cost functional. In the case of this example Zermelo problem, the cost functional minimizes the mean error of the terminal position of the ship [153], [172]. The goal is to maneuver the ship in the uncertain wind environment while reaching the destination or getting as close as possible to it. An uncertain version ( $Z_{\text{unc}}$ ) of the deterministic Zermelo ( $Z_D$ ) problem is shown here:

$$\mathbf{x} := (x, y) \in \mathbb{R}^2$$

$$\mathbf{u} \in \mathbb{U} := \{(u_1, u_2) \in \mathbb{R}^2 : u_1^2 + u_2^2 = 1\}$$

$$\mathbf{p} := (p, q) \sim \mathcal{N}((1, -1), \text{diag}(0.2^2, 0.1^2))$$

$$(Z_{unc}) \left\{ \begin{array}{ll} \text{Minimize} & J_{Zu}[\mathbf{x}(\cdot, \cdot), \mathbf{u}(\cdot), t_f; \mathbf{p}] \quad := t_f \\ \text{Subject to} & \mathbf{x}(t, \mathbf{p}) \quad = \mathbf{p}y(t, \mathbf{p}) + u_1(t) \\ & \mathbf{y}(t, \mathbf{p}) \quad = \mathbf{q}x(t, \mathbf{p}) + u_2(t) \\ & (\mathbf{x}(t_0), t_0) \quad = (2.25, 1, 0) \\ & \mathbf{x}(t_f, \mathbf{p}) \quad = \mathbf{0} \end{array} \right\}$$

The problem formulation for uncertain Zermelo incorporates the wind vector field as a uniformly uncertain term. In deterministic Zermelo, the wind vector field was defined as  $\mathbf{p} = (p, q) = (1, -1)$ , whereas in uncertain Zermelo it is defined as a nominal value at  $(1, -1)$  with uniform uncertainty of  $0.2^2$  in  $p$  and  $0.1^2$  in  $q$ . The uncertainty in the  $\mathbf{p}$  vector field propagates into the dynamics terms and the final position of the ship, as shown by the addition of both  $\mathbf{p}$  and  $\mathbf{q}$  terms in the problem formulation.

The uncertain Zermelo problem is not readily solvable due to uncertainty in  $\mathbf{p}$ . Using the same technique described in “Introduction to Optimal Control with Parameter Uncertainty” and “Semi-Discrete Lebesgue-Stieltjes,” the uncertain Zermelo problem is transformed into a semi-discrete Lebesgue-Stieltjes problem. The Lebesgue-Stieltjes integral is replaced by an ensemble of sampling points,  $\mathbf{p}_i$ , with weights,  $w_i$ ,  $(\mathbf{p}_i, w_i)$  for  $i = 1, 2, \dots, n$ , that sample the statistical distribution of the uncertain wind vector field,  $\mathbf{p}$  [175], [177-178]. The semi-discrete Lebesgue-Stieltjes Zermelo problem formulation is written as a sequence of standard endpoint (“Mayer”) optimal control problems where  $n = \infty$  [153], [172], [174-175], [177-178], [211]:

$$\mathbf{x} := [(x_1, y_1), \dots, (x_n, y_n)] \in \mathbb{R}^{2n}$$

$$\mathbf{u} \in \mathbb{U} := \{(u_1, u_2) \in \mathbb{R}^2 : u_1^2 + u_2^2 = 1\}$$

$$\left. \begin{array}{ll}
\text{Minimize} & J_{LSn}[\mathbf{x}_1(\cdot, \cdot), \dots, \mathbf{x}_n(\cdot, \cdot), \mathbf{u}(\cdot), t_f; \mathbf{p}] \quad \doteq \sum_{i=1}^{n=\infty} w_i x_i^2(t_f, \mathbf{p}_i) + \sum_{i=1}^{n=\infty} w_i y_i^2(t_f, \mathbf{p}_i) \\
\text{Subject to} & \dot{x}_1(t, \mathbf{p}_1) = p_1 y(t, \mathbf{p}_1) + u_1(t) \\
& \dot{y}_1(t, \mathbf{p}_1) = q_1 x(t, \mathbf{p}_1) + u_2(t) \\
& \vdots \\
& \dot{x}_{n=\infty}(t, \mathbf{p}_{n=\infty}) = p_{n=\infty} y(t, \mathbf{p}_{n=\infty}) + u_1(t) \\
& \dot{y}_{n=\infty}(t, \mathbf{p}_{n=\infty}) = q_{n=\infty} x(t, \mathbf{p}_{n=\infty}) + u_2(t) \\
& (x_1(t_0), y_1(t_0), t_0) = (2.25, 1, 0) \\
& \vdots \\
& (x_{n=\infty}(t_0), y_{n=\infty}(t_0), t_0) = (2.25, 1, 0) \\
& \sum_{i=1}^{n=\infty} w_i x_i(t_f, \mathbf{p}_i) = \mathbf{0} \\
& \sum_{i=1}^{n=\infty} w_i y_i(t_f, \mathbf{p}_i) = \mathbf{0} \\
& \mathbf{p}_i \in \text{supp}(\mathbf{p}) \forall i = 1, 2, \dots, n = \infty
\end{array} \right\} (Z_{LSn})$$

This semi-discrete Lebesgue-Stieltjes Zermelo problem formulation is easily changed to an unscented guidance problem formulation by replacing the infinite number of Lebesgue-Stieltjes weighted points with a small number of sigma points. The sigma points statistically sample the solution space [153]. They are developed using the spherical simplex unscented transform methodology as defined by Julier [155] where spherical simplex points lie on the origin or on a hypersphere centered at the origin. The general spherical simplex unscented transform sigma point definition is:

$$\chi_i^j = \left\{ \begin{array}{ll} \begin{bmatrix} \chi_0^{j-1} \\ 0 \end{bmatrix} & \text{for } i = 0 \\ \begin{bmatrix} \chi_i^{j-1} \\ -\frac{1}{\sqrt{j(j+1)W_i}} \end{bmatrix} & \text{for } i = 1, \dots, j \\ \begin{bmatrix} 0_{j-1} \\ \frac{j}{\sqrt{j(j+1)W_i}} \end{bmatrix} & \text{for } i = j+1 \end{array} \right\} \quad (23)$$

For the semi-discrete Lebesgue-Stieltjes Zermelo problem, the number of sigma points desired,  $i$ , is four, the space dimension,  $j$ , is two, and the state dimension,  $n$ , is two. A set of four spherical simplex points for  $Z_{LSn}$  gives us  $Z_{N=4}$ . This set of four sigma points (23) is defined using the following six steps:

1. Define the dimension of the problem then calculate the number of sigma points necessary to describe it:
  - a. Define  $Z_{N=4}$  as an  $n = 2$ -dimension problem
  - b. Number of sigma points =  $n + 2 = 4$  (or  $N=4$  for  $Z_{N=4}$ )
2. Choose a weight for initial sigma point that is between 0 and 1
  - c. Choose  $W_0 = 1/4$  for this case since it is one of  $N=4$  total sigma points which makes the math straightforward
3. Constrain  $W_1 = W_2$  and solve for these weights using:

$$W_i = (1 - W_0) / (n + 1)$$

- d. So  $W_1 = W_2 = W_3 = 1/4$
4. Check that  $W_0 + W_1 + W_2 + W_3 = 1$
5. Initialize sigma point vector sequence for  $j = 2$ :

$$\chi_i^{j=2} = \left\{ \begin{array}{ll} \begin{bmatrix} 0 \\ 0 \end{bmatrix} & \text{for } i = 0 \\ \begin{bmatrix} \frac{1}{\sqrt{2W_1}} \\ -\frac{1}{\sqrt{2W_1}} \end{bmatrix} & \text{for } i = 1 \\ \begin{bmatrix} \frac{1}{\sqrt{2W_2}} \\ -\frac{1}{\sqrt{2W_2}} \end{bmatrix} & \text{for } i = j = 2 \\ \begin{bmatrix} 0 \\ \frac{2}{\sqrt{6W_3}} \end{bmatrix} & \text{for } i = j + 1 = 3 \end{array} \right\} \quad (24)$$

6. Transform the sigma point vector sequence (24) from zero mean and unit covariance of the  $n \times n$  Identity matrix  $\mathbf{P}_{zz}$  to center at mean  $p = (1, -1)$  and covariance:

$$P_{zz} = \begin{bmatrix} 0.2^2 & 0 \\ 0 & 0.1^2 \end{bmatrix}$$

This transformation uses the following equation [155]:

$$\mathcal{Z}_i^j = \bar{\mathbf{z}} + \sqrt{\mathbf{P}_{zz}} \chi_i^j \quad (25)$$

where the square root of  $\mathbf{P}_{zz}$  is a matrix square root of  $\mathbf{P}_{zz}$  using for example the Cholesky decomposition. This transformation (25) results in the following transformed sigma point vector sequence:

$$\chi_{N_i}^{j=2} = \left\{ \begin{array}{ll} \begin{bmatrix} 1 \\ -1 \end{bmatrix} & \text{for } i = 0 \\ \begin{bmatrix} 1 + 0.2 * \left( -\frac{1}{\sqrt{2W_1}} \right) \\ -1 + 0.1 * \left( -\frac{1}{\sqrt{2W_1}} \right) \end{bmatrix} & \text{for } i = 1 \\ \begin{bmatrix} 1 + 0.2 * \left( -\frac{1}{\sqrt{2W_2}} \right) \\ -1 + 0.1 * \left( -\frac{1}{\sqrt{6W_2}} \right) \end{bmatrix} & \text{for } i = j = 2 \\ \begin{bmatrix} 1 \\ -1 + 0.1 * \left( \frac{2}{\sqrt{6W_3}} \right) \end{bmatrix} & \text{for } i = j + 1 = 3 \end{array} \right\} \quad (26)$$

Using this set of  $N = 4$  sigma points (26), the next step is to re-write the  $Z_{LSn}$  problem formulation as the following semi-discretization  $Z_{N=4}$  where each sigma point is a copy of the initial problem formulation:

$$\mathbf{x} := [(x_1, y_1), (x_2, y_2), (x_3, y_3), (x_4, y_4)] \in \mathbb{R}^8$$

$$\mathbf{u} \in \mathbb{U} := \{(u_1, u_2) \in \mathbb{R}^2 : u_1^2 + u_2^2 = 1\}$$

$$\mathbf{p} := (p, q) \sim \mathcal{N}((1, -1), \text{diag}(0.2^2, 0.1^2))$$

$$(Z_{N=4}) \left\{ \begin{array}{ll} \text{Minimize} & J[\mathbf{x}_i(\cdot, \cdot), \mathbf{u}(\cdot), t_f; \mathbf{p}] \doteq \sum_{i=1}^4 w_i x_i^2(t_f, \mathbf{p}_i) + \sum_{i=1}^4 w_i y_i^2(t_f, \mathbf{p}_i) \\ \text{Subject to} & \dot{x}_1(t, \mathbf{p}_1) = p_1 y_1(t, \mathbf{p}_1) + u_1(t) \\ & \dot{y}_1(t, \mathbf{p}_1) = q_1 x_1(t, \mathbf{p}_1) + u_2(t) \\ & \dot{x}_2(t, \mathbf{p}_2) = p_2 y_2(t, \mathbf{p}_2) + u_1(t) \\ & \dot{y}_2(t, \mathbf{p}_2) = q_2 x_2(t, \mathbf{p}_2) + u_2(t) \\ & \dot{x}_3(t, \mathbf{p}_3) = p_3 y_3(t, \mathbf{p}_3) + u_1(t) \\ & \dot{y}_3(t, \mathbf{p}_3) = q_3 x_3(t, \mathbf{p}_3) + u_2(t) \\ & \dot{x}_4(t, \mathbf{p}_4) = p_4 y_4(t, \mathbf{p}_4) + u_1(t) \\ & \dot{y}_4(t, \mathbf{p}_4) = q_4 x_4(t, \mathbf{p}_4) + u_2(t) \\ & (x_1(t_0), y_1(t_0), t_0) = (2.25, 1, 0) \\ & (x_2(t_0), y_2(t_0), t_0) = (2.25, 1, 0) \\ & (x_3(t_0), y_3(t_0), t_0) = (2.25, 1, 0) \\ & (x_4(t_0), y_4(t_0), t_0) = (2.25, 1, 0) \\ & \sum_{i=1}^4 w_i x_i(t_f, \mathbf{p}_i) = 0 \\ & \sum_{i=1}^4 w_i y_i(t_f, \mathbf{p}_i) = 0 \\ & \mathbf{p}_i \in \text{supp}(\mathbf{p}) \forall i = 1, 2, 3, 4 \end{array} \right.$$

A candidate optimal control solution to this uncertain Zermelo problem by can be evaluated by developing Pontryagin's necessary conditions.

### Construct the Hamiltonian(s)

The uncertain Zermelo problem formulation defines the following state vector in primal space:

$$\mathbf{x} \in \mathbb{R}^8$$

The  $\lambda$  cost unit is used for measurement of the control Hamiltonian, and it follows for the uncertain Zermelo problem that this adjoint co-vector exists in the same dimension but in dual space:

$$\lambda \in \mathbb{R}^8$$

The adjoint co-vector for the uncertain Zermelo problem is defined as:

$$\lambda := \begin{bmatrix} \lambda_{x_1} \\ \lambda_{y_1} \\ \lambda_{x_2} \\ \lambda_{y_2} \\ \lambda_{x_3} \\ \lambda_{y_3} \\ \lambda_{x_4} \\ \lambda_{y_4} \end{bmatrix}$$

The uncertain Zermelo Hamiltonian is then given by:

$$H(\lambda, \mathbf{x}, \mathbf{u}, t) := 0 + \begin{bmatrix} \lambda_{x_1} & \lambda_{y_1} & \lambda_{x_2} & \lambda_{y_2} & \lambda_{x_3} & \lambda_{y_3} & \lambda_{x_4} & \lambda_{y_4} \end{bmatrix} \begin{bmatrix} p_1 y_1(t, \mathbf{p}_1) + u_1(t) \\ q_1 x_1(t, \mathbf{p}_1) + u_2(t) \\ p_2 y_2(t, \mathbf{p}_2) + u_1(t) \\ q_2 x_2(t, \mathbf{p}_2) + u_2(t) \\ p_3 y_3(t, \mathbf{p}_3) + u_1(t) \\ q_3 x_3(t, \mathbf{p}_3) + u_2(t) \\ p_4 y_4(t, \mathbf{p}_4) + u_1(t) \\ q_4 x_4(t, \mathbf{p}_4) + u_2(t) \end{bmatrix} \quad (27)$$

This equation can be rewritten as:



$$\begin{aligned}
H(\boldsymbol{\lambda}, \mathbf{x}, \mathbf{u}, t) = & \lambda_{x_1} (p_1 y_1(t, \mathbf{p}_1) + u_1(t)) + \lambda_{y_1} (q_1 x_1(t, \mathbf{p}_1) + u_2(t)) + \lambda_{x_2} (p_2 y_2(t, \mathbf{p}_2) + u_1(t)) + \dots \\
& \lambda_{y_2} (q_2 x_2(t, \mathbf{p}_2) + u_2(t)) + \lambda_{x_3} (p_3 y_3(t, \mathbf{p}_3) + u_1(t)) + \lambda_{y_3} (q_3 x_3(t, \mathbf{p}_3) + u_2(t)) + \dots \\
& \lambda_{x_4} (p_4 y_4(t, \mathbf{p}_4) + u_1(t)) + \lambda_{y_4} (q_4 x_4(t, \mathbf{p}_4) + u_2(t))
\end{aligned}$$

Because this problem also has a control constraint, the Lagrangian of the Hamiltonian ( $\bar{H}$ ) must be used. The Lagrangian of the Hamiltonian is defined as:

$$\bar{H}(\boldsymbol{\mu}, \boldsymbol{\lambda}, \mathbf{x}, \mathbf{u}, t) := H(\boldsymbol{\lambda}, \mathbf{x}, \mathbf{u}, t) + \boldsymbol{\mu}^T \mathbf{h}(\mathbf{u})$$

The  $\mu$  cost unit is defined for measurement of the Lagrangian of the Hamiltonian. The transpose of the path co-vector ( $\mu$ ) is defined as:

$$\boldsymbol{\mu}^T = [\mu]$$

The path function,  $h$ , uses the path constraint:

$$\mathbf{h}(\mathbf{u}, t) = u_1(t)^2 + u_2(t)^2$$

Which allows the uncertain Zermelo Lagrangian of the Hamiltonian to be written:

$$\begin{aligned}
\bar{H}(\boldsymbol{\mu}, \boldsymbol{\lambda}, \mathbf{x}, \mathbf{u}, t) = & \lambda_{x_1} (p_1 y_1(t, \mathbf{p}_1) + u_1(t)) + \lambda_{y_1} (q_1 x_1(t, \mathbf{p}_1) + u_2(t)) + \lambda_{x_2} (p_2 y_2(t, \mathbf{p}_2) + u_1(t)) + \dots \\
& \lambda_{y_2} (q_2 x_2(t, \mathbf{p}_2) + u_2(t)) + \lambda_{x_3} (p_3 y_3(t, \mathbf{p}_3) + u_1(t)) + \lambda_{y_3} (q_3 x_3(t, \mathbf{p}_3) + u_2(t)) + \dots \\
& \lambda_{x_4} (p_4 y_4(t, \mathbf{p}_4) + u_1(t)) + \lambda_{y_4} (q_4 x_4(t, \mathbf{p}_4) + u_2(t)) + \mu(u_1(t)^2 + u_2(t)^2)
\end{aligned} \tag{28}$$

### Develop the adjoint equations

The adjoint equations are found by taking the partial derivative of the Hamiltonian with respect to the state variables at each of the four sigma points:

$$-\dot{\lambda}_{x_1} := \frac{\partial H}{\partial x_1} = \lambda_{y_1} q_1$$

$$-\dot{\lambda}_{x_2} := \frac{\partial H}{\partial x_2} = \lambda_{y_2} q_2$$

$$\begin{aligned}
-\dot{\lambda}_{x_3} &:= \frac{\partial H}{\partial x_3} = \lambda_{y_3} q_3 \\
-\dot{\lambda}_{x_4} &:= \frac{\partial H}{\partial x_4} = \lambda_{y_4} q_4 \\
-\dot{\lambda}_{y_1} &:= \frac{\partial H}{\partial y_1} = \lambda_{x_1} p_1 \\
-\dot{\lambda}_{y_2} &:= \frac{\partial H}{\partial y_2} = \lambda_{x_2} p_2 \\
-\dot{\lambda}_{y_3} &:= \frac{\partial H}{\partial y_3} = \lambda_{x_3} p_3 \\
-\dot{\lambda}_{y_4} &:= \frac{\partial H}{\partial y_4} = \lambda_{x_4} p_4
\end{aligned} \tag{29}$$

### Minimize the Hamiltonian

The uncertain Zermelo problem must meet a combination of stationarity and complementarity conditions such that the problem is minimized at each instant of time [164]. The stationarity condition as defined in (9) is repeated here for reference:

$$\frac{\partial \bar{H}}{\partial \mathbf{u}} = \frac{\partial H}{\partial \mathbf{u}} + \left( \frac{\partial \mathbf{h}}{\partial \mathbf{u}} \right)^T \boldsymbol{\mu} = \mathbf{0}$$

The complementarity condition as defined in (10) is:

$$\mu_i \begin{cases} \leq 0 & \text{if } h_i(\mathbf{u}, t) = h_i^L(t) \\ = 0 & \text{if } h_i^L(t) < (h_i(\mathbf{u}, t)) < h_i^U(t) \\ \geq 0 & \text{if } h_i(\mathbf{u}, t) = h_i^U(t) \\ \text{unrestricted} & \text{if } h_i^L(t) = h_i^U(t) \end{cases}$$

The stationarity condition is now applied to the uncertain Zermelo problem such that the partial derivative of  $\bar{H}$  with respect to  $\mathbf{u}$  is set equal to zero:

$$\frac{\partial \bar{H}}{\partial u_1} = \lambda_{x_1} + \lambda_{x_2} + \lambda_{x_3} + \lambda_{x_4} + 2\mu u_1 = 0 \quad (30)$$

$$\frac{\partial \bar{H}}{\partial u_2} = \lambda_{y_1} + \lambda_{y_2} + \lambda_{y_3} + \lambda_{y_4} + 2\mu u_2 = 0 \quad (31)$$

Then the complementarity condition is applied, which provides information about the behavior of the path co-vector that in this case is the same equation as for the deterministic Zermelo case (13):

$$h^L(t) = h^U(t)$$

This condition results in  $\mu$  being unrestricted because:

$$1 \leq u_1^2 + u_2^2 \leq 1$$

### Construct the Endpoint Lagrangian

The uncertain Zermelo problem is in the Mayer form, with final position equal to zero as the objective. Endpoint boundary conditions must be evaluated at final time using the transversality conditions, the Hamiltonian value condition, and the Hamiltonian evolution equation. The Endpoint Lagrangian equation is constructed to evaluate these conditions.

The endpoint Lagrangian equation is defined in (14) as:

$$\bar{E}(\mathbf{v}, \mathbf{x}_f, t_f) := E(\mathbf{x}_f, t_f) + \mathbf{v}^T \mathbf{e}(\mathbf{x}_f, t_f)$$

This equation partially depends on the endpoint function which is defined as the following:

$$\mathbf{e}(\mathbf{x}_f, t_f) := \begin{bmatrix} \sum_{i=1}^4 w_i x_i \\ \sum_{i=1}^4 w_i y_i \end{bmatrix} = \mathbf{0}$$

The  $v$  variables are defined for measurement of the endpoint Lagrangian. The transpose of the endpoint co-vector ( $v$ ) is defined as:

$$v^T = \begin{bmatrix} v_x & v_y \end{bmatrix}$$

For the uncertain Zermelo problem, the endpoint Lagrangian equation becomes:

$$\bar{E}(\mathbf{v}, \mathbf{x}_f, t_f) := 0 + \begin{bmatrix} v_x & v_y \end{bmatrix} \begin{bmatrix} \sum_{i=1}^4 w_i x_i \\ \sum_{i=1}^4 w_i y_i \end{bmatrix}$$

This equation can be written as:

$$\bar{E}(\mathbf{v}, \mathbf{x}_f, t_f) := v_x \sum_{i=1}^4 w_i x_i + v_y \sum_{i=1}^4 w_i y_i \quad (32)$$

### Determine the transversality conditions

Transversality conditions are found by taking the partial derivative of the Endpoint Lagrangian ( $\bar{E}$ ) with respect to the final positions of the state vectors, or more generally, the terminal state at each of the four sigma points where the sum of weights is equal to one:

$$\begin{aligned} \lambda_x(t_f) &:= \frac{\partial \bar{E}}{\partial x_f} = v_x \\ \lambda_y(t_f) &:= \frac{\partial \bar{E}}{\partial y_f} = v_y \end{aligned} \quad (33)$$

These terms give us unknowns in terms of other unknowns, so no new useful information is provided.

### **Hamiltonian value condition**

An endpoint cost is evaluated using the Hamiltonian value condition. The minimized Hamiltonian is called the lower Hamiltonian which is denoted by  $\mathcal{H}$ . The lower Hamiltonian at final time is equivalent to the negative of the partial derivative of the endpoint Lagrangian ( $\bar{E}$ ) taken with respect to final time. Evaluating this partial derivative is known as the Hamiltonian value condition. The uncertain Zermelo problem yields the following Hamiltonian value condition:

$$\mathcal{H}[\textcircled{t}_f] := -\frac{\partial \bar{E}}{\partial t_f} = 0 \quad (34)$$

that is standard for time-free problems.

### **Hamiltonian evolution equation**

The derivative of the lower Hamiltonian with respect to time is equivalent to the partial derivative of the Lagrangian of the Hamiltonian with respect to time. The uncertain Zermelo problem yields the following Hamiltonian evolution equation:

$$\frac{d\mathcal{H}}{dt} = \frac{\partial \bar{H}}{\partial t} = 0 \quad (35)$$

This equation tells us that the value of the lower Hamiltonian will be a constant.

### **Review of Necessary Conditions**

Both the Hamiltonian and Lagrangian of the Hamiltonian (27) and (28), were found for the uncertain Zermelo problem. The Hamiltonian offered no insight to the problem, but the Lagrangian of the Hamiltonian provided more information. The Lagrangian of the

Hamiltonian was evaluated using both the complementarity and stationarity conditions (9) and (10). The complementarity condition, when applied to the uncertain Zermelo problem, resulted in the path co-vector,  $\mu$ , being unrestricted as in deterministic Zermelo (13). The stationarity condition provided equations that relate the adjoint co-vectors at each sigma point to the path co-vector and control solutions (30) and (31). These equations will be used to validate the control solution results shown later in this section. In addition, the adjoint co-vectors at each sigma point must meet requirements imposed on their derivatives such that the derivative of  $\lambda_x$  is equivalent to  $-\lambda_y$  scaled by an uncertain wind term,  $q$ . Also, the derivative of  $\lambda_y$  is equal to  $-\lambda_x$  scaled by an uncertain wind term,  $p$ . These derivative requirements hold true at each sigma point (29). The Endpoint Lagrangian was developed to provide evaluation of transversality conditions, the Hamiltonian value condition, and the Hamiltonian evolution equation (32). Transversality conditions were evaluated for each sigma point, but no new information was provided (33). The Hamiltonian value condition was evaluated for the deterministic Zermelo problem and showed that the value of the lower Hamiltonian was a constant of 0 (34). This value is consistent with the literature regarding time-free problems [164]. Evaluation of the Hamiltonian evolution equation for the uncertain Zermelo problem stipulated that the value of the lower Hamiltonian be a constant, and the result of 0 meets that expectation (35).

With knowledge of these necessary conditions and using the  $Z_{N=4}$  unscented guidance framework, a candidate control solution (both  $u_1$  and  $u_2$ ) for the  $Z_{N=4}$  problem is found using the optimal solver, DIDO [167]. Figure 9 shows the candidate control solutions of  $u_1$  and  $u_2$  for the uncertain Zermelo problem.

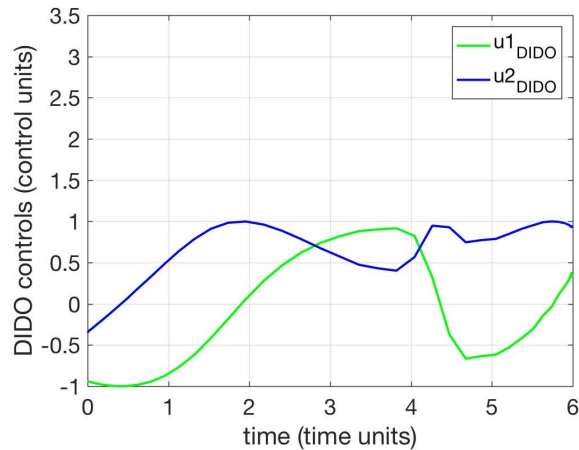


Figure 9. Solution of the Uncertain Zermelo Problem: Optimal Control Versus Time

The optimal trajectories,  $y$ -position vs.  $x$ -position for each sigma point, are shown in Figure 10 and their shapes are spirals. The four sigma point solutions are grouped close to a final position of  $(0, 0)$ :  $(0.08, 0.06)$ ,  $(-0.02, -0.03)$ ,  $(-0.03, -0.02)$  and  $(-0.03, -0.02)$ .

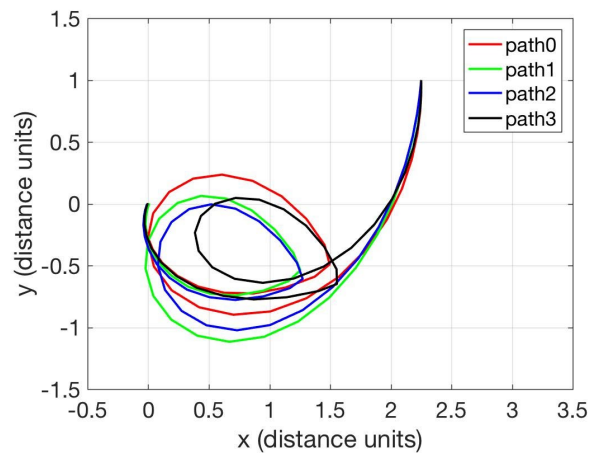


Figure 10. Solution of the Uncertain Zermelo Problem: Optimal Position  $y$  Versus  $x$

For this uncertain Zermelo optimal control problem, Hamiltonian, co-states (adjoint and path co-vectors) and path constraint are reviewed as an indication of solution optimality. These necessary conditions derivations must hold for the candidate solution to

be considered an optimal solution. As a part of the necessary conditions derivations, evaluation of the Hamiltonian value condition stipulated that the minimized Hamiltonian would be a constant close to 0 which is consistent with a time-free problem. Indeed, as seen in Figure 11, the candidate solution does have a minimized Hamiltonian value close to 0. Figures 12 and 13 show that all co-states are close to zero even though the associated control trajectories are not. This knowledge can be used to re-visit the stationarity condition that produced the following equations:

$$\frac{\partial \bar{H}}{\partial u_1} = \lambda_{x_1} + \lambda_{x_2} + \lambda_{x_3} + \lambda_{x_4} + 2\mu u_1 = 0$$

$$\frac{\partial \bar{H}}{\partial u_2} = \lambda_{y_1} + \lambda_{y_2} + \lambda_{y_3} + \lambda_{y_4} + 2\mu u_2 = 0$$

Substitution of the co-state variables with values close to zero in either equation leads to a  $\mu$  value that is also close to zero. Figure 14 shows that the value of the path co-vector,  $\mu$ , is close to zero for all time.

A path constraint was imposed on the problem such that  $u_1^2 + u_2^2 = 1$ . Figure 15 shows that this constraint was met as the value of the path function is 1 for all time.

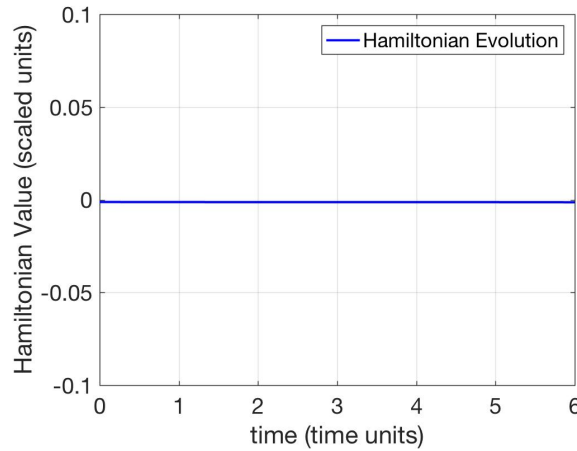


Figure 11. Solution of the Uncertain Zermelo Problem: Optimal Hamiltonian Versus Time



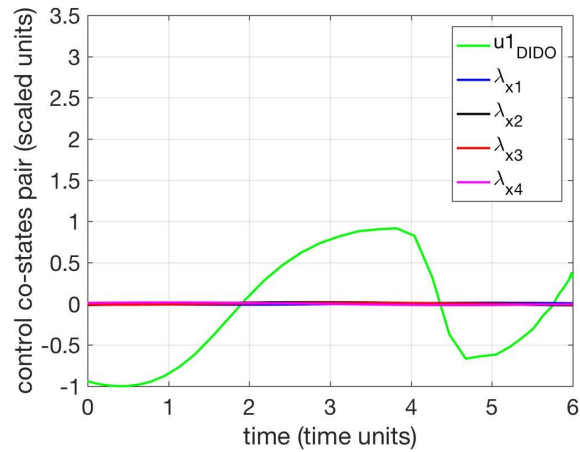


Figure 12. Solution of the Uncertain Zermelo Problem: Optimal Control  $u_1$  and Co-States  $\lambda_x$  Pair Versus Time

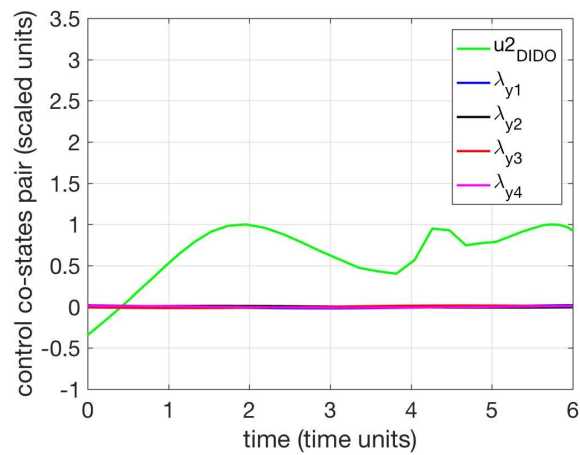


Figure 13. Solution of the Uncertain Zermelo Problem: Optimal Control  $u_2$  and Co-States  $\lambda_y$  Pair Versus Time

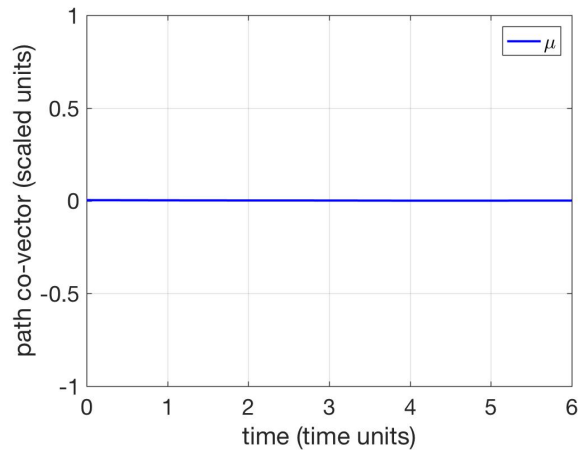


Figure 14. Solution of the Uncertain Zermelo Problem: Optimal Path Co-Vector Versus Time

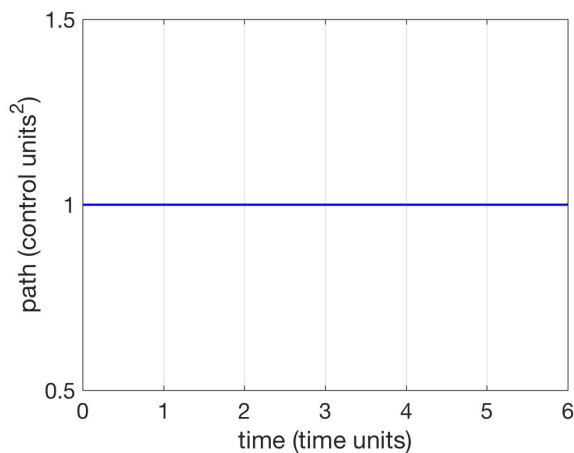


Figure 15. Solution of the Uncertain Zermelo Problem: Constraint Path Versus Time

As a final test of the candidate control solution, a propagation test was performed. This test takes the candidate control solutions,  $u_1$  and  $u_2$ , then uses a MATLAB numerical integrator to produce a position solution in the  $xy$ -plane. This Monte Carlo solution was generated  $N=10$  times to capture the effect of the uncertain wind terms. The “goodness” of the candidate control solutions can be evaluated based on how close the propagated position results come to the optimal results [164]. Figure 16 shows that propagation of this set of candidate control solutions provides results that are similar to the optimal results

shown in Figure 10. The shape of the curves for both result sets are similar, but the propagated figure shows final position offsets within approximately  $(\pm 0.05, \pm 0.03)$  from the desired position of  $(0, 0)$ . This error is expected due to the uncertainty in the wind vector field,  $\mathbf{p}$ . This propagated result shows that the optimal solution has successfully accommodated the uncertainty.

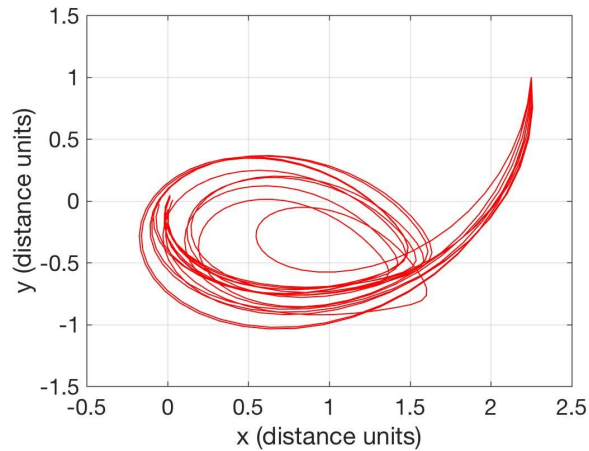


Figure 16. Solution of the Uncertain Zermelo Problem: Propagation Test  $y$  Versus  $x$  Using  $N=10$  Monte Carlo Runs

Due to the predicted Hamiltonian, co-states, path constraint, and propagation test results meeting expectations, this candidate optimal control solution is considered an optimal solution to the  $Z_{N=4}$  problem. Figure 17 depicts the data from the  $N=1000$  run Monte Carlo scenario for the uncertain Zermelo problem,  $Z_{N=4}$ . The mean final position was  $(0.12, 0.02)$  for the Monte Carlo solution. The mean error for the Monte Carlo solution was  $x = 0.0014$  and  $y = 0.0008$ . The Monte Carlo standard deviation was  $0.0828$  and  $0.1631$  for  $x$  and  $y$  respectively. These results agree with results published in the paper “Unscented Guidance” where the error mean was  $x = -0.0018$  and  $y = 0.0005$  and standard deviation was  $x = 0.1139$  and  $y = 0.1112$  [153].

Table 2 summarizes mean error and standard deviation results for  $Z_D$  and  $Z_{N=4}$ . Both mean error and standard deviation values were smaller for  $Z_{N=4}$  versus  $Z_D$  even though  $Z_{N=4}$  includes uncertainty in the dynamics. Mean error for  $Z_{N=4}$  was  $(0.0014, 0.0008)$  which was

more than an order of magnitude (ten times) smaller than the  $Z_D$  values of (0.0333, 0.0152). Standard deviation for  $Z_{N=4}$  was (0.0828, 0.1631) which was smaller than the  $Z_D$  values of (0.2351, 0.1712). These uncertain Zermelo results are better than the deterministic Zermelo results because use of sigma points properly captures the statistics of the problem whereby both the mean error and standard deviation values are reduced.

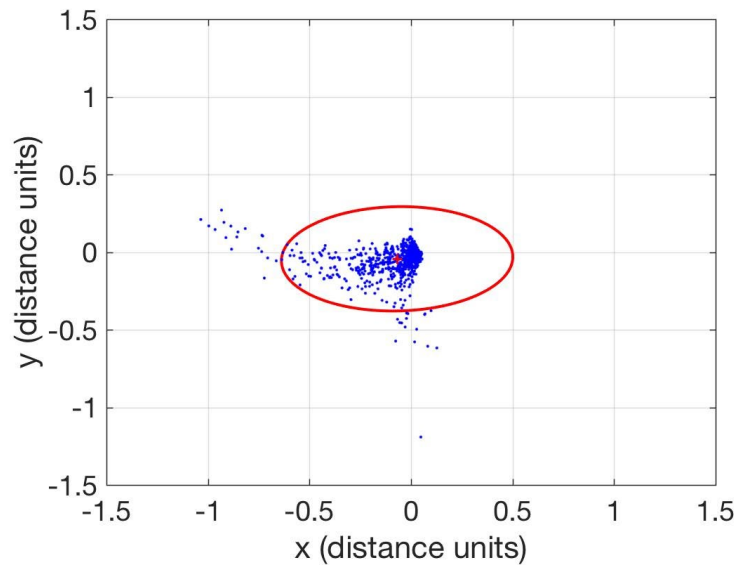


Figure 17. Solution of the Uncertain Zermelo problem:  $N=1000$   
Monte Carlo Simulation of Target Error Distribution

Table 2.  $Z_D$  and  $Z_{N=4}$  Monte Carlo Error and Standard Deviation Results

| Zermelo Version | Target Value | Error Mean | Standard Deviation |
|-----------------|--------------|------------|--------------------|
| $Z_D$           | $x(t_f) = 0$ | 0.0333     | 0.2351             |
|                 | $y(t_f) = 0$ | 0.0152     | 0.1712             |
| $Z_{N=4}$       | $x(t_f) = 0$ | 0.0014     | 0.0828             |
|                 | $y(t_f) = 0$ | 0.0008     | 0.1631             |

It is obvious that a minimum number of sigma points is necessary to properly capture statistical information about the optimal control problem. These Zermelo problem results reveal that a number of sigma points corresponding with only the first few moments of the problem contributes to reductions in mean error and covariance. These reductions in

error and covariance give confidence in the methodology of using unscented guidance with sigma points to achieve an optimal solution.

## **7. Dissertation Use of Unscented Guidance Method**

The two versions of the Zermelo problem studied in [153] developed a methodology for generating an unscented guidance optimal control solution. The deterministic Zermelo problem established a foundation of problem development. The optimal control solution found for the uncertain Zermelo problem was verified using a Monte Carlo simulation. This simulation showed improved error statistics, both smaller mean error and standard deviation, thus demonstrating that the unscented guidance concept is a valid method for sampling an uncertain linear system. The methodology summarized here is used to develop a control solution for the non-linear unscented reaction wheel maneuver problem in the following chapters of this dissertation.

## **C. CHAPTER SUMMARY**

The purpose of this chapter was to introduce the concept of optimal control for a linear system (with application for non-linear systems), the effect of uncertain parameters on these systems and the framework of sampling that is used to find solutions for uncertain optimal control problems. A deterministic Zermelo minimum-time problem was used to illustrate how a linear optimal control problem is formulated. This problem was then solved through application of Pontryagin's necessary conditions for optimality. A candidate control solution was developed using DIDO in MATLAB and tested against the necessary conditions. The candidate control solution was found to be an actual optimal control solution. The deterministic Zermelo problem was changed to accommodate an uncertain parameter, in this case a wind vector field, that affects the position of a ship maneuvering within it. Monte Carlo, Multidimensional Approximation and Unscented Guidance sampling were introduced as possible methods for determining a solution for an optimal control problem with uncertain parameters. An uncertain Zermelo problem was developed using a semi-discrete Lebesgue-Stieltjes approach then solved through development of Pontryagin's necessary conditions for optimality. A candidate control solution was produced using the chosen method of unscented guidance sigma point sampling within

DIDO/MATLAB. The candidate uncertain Zermelo control solution was compared against the necessary conditions for optimality and was found to be an optimal control solution. A Monte Carlo analysis of the candidate control solution was also run to confirm optimal results and validate use of sigma points as a sampling method. The sigma point sampling is used going forward in this dissertation.

THIS PAGE INTENTIONALLY LEFT BLANK

### **III. CONVENTIONAL REACTION-WHEEL ATTITUDE CONTROL**

This chapter defines the representative spacecraft model, describes useful concepts associated with the model such as equations of motion and quaternions, uses the model to demonstrate a closed-loop (feedback) maneuver, uses the model to demonstrate a baseline open-loop maneuver, and illustrates why open-loop control systems are typically not used.

#### **A. REPRESENTATIVE SPACECRAFT**

There are many spacecraft that have experienced mission ending feedback sensor hardware failures. Some spacecraft such as the Hubble Space Telescope (HST) and the Lunar Reconnaissance Orbiter (LRO) have been able to overcome hardware failures and experience longer science lifetimes due to the work of engineers and scientists who have been able to craft mission extending control system software fixes to these hardware problems.

HST has generated a wealth of science data; its hardware components and software changes, including to the control system, are well documented [29], [55], [212-222]. HST engineering and science teams conceived of reduced mode (safemode) software contingency plans for expected hardware failures as far back as 1990, some of which have been tested on the spacecraft [29], [213]. Additional reduced mode (Two-Gyro Science Mode (TGS) and One-Gyro Science Mode (OGS)) software contingency plans have been developed since that time and tested on-orbit [53], [222]. These reduced mode software versions are available to be turned-on as hardware continues to age and fail [55].

In contrast, LRO is a much newer spacecraft that recently experienced a hardware failure that forced changes to the control software for the mission to continue [56]. In fact, research is ongoing among the LRO team to further improve the control software and extend the mission given the failed hardware and other mission constraints [223]. Values used for the dissertation spacecraft include baseline inertia tensor, reaction wheel alignment matrix and maximum reaction wheel torque are similar to the values of the LRO satellite. Maximum slew rate is a value imposed on the dissertation spacecraft due to the



proportional rate limiter. Reaction wheel torque discount, position and rate gains are chosen to be representative values [31]. Table 3 presents an overview of the parameters used in this dissertation.

Table 3.           Spacecraft Parameters Used in This Dissertation

| Parameter                       | Symbol                    | Value   | Units                           |
|---------------------------------|---------------------------|---|---------------------------------|
| nominal inertia tensor          | $\mathbf{J}_{\text{nom}}$ | $\begin{bmatrix} 1168.0 & 0 & 0 \\ 0 & 1296.4 & 0 \\ 0 & 0 & 940.5 \end{bmatrix}$   | $\text{kg} \cdot \text{m}^2$    |
| reaction wheel alignment matrix | $\mathbf{Z}$              | $\begin{bmatrix} 0.5736 & 0.5736 & 0.5736 & 0.5736 \\ 0.5792 & -0.5792 & -0.5792 & 0.5792 \\ 0.5792 & 0.5792 & -0.5792 & -0.5792 \end{bmatrix}$ | —                               |
| maximum reaction wheel torque   | $u_{\text{max}}$          | 0.16  | $\text{N} \cdot \text{m}$       |
| reaction wheel torque discount  | $\eta$                    | 0.75  | —                               |
| maximum slew rate*              | $\omega_{\text{max}}$     | 0.5   | deg/s                           |
| position gain                   | $k_p$                     | $0.085^2$   | $1/\text{s}^2$                  |
| rate gain                       | $k_r$                     | 0.017   | $1/(\text{rad} \cdot \text{s})$ |

\*Maximum slew rate is a value that is imposed due to the proportional rate limiter.

## B.    SPACECRAFT ATTITUDE KINEMATICS

Quaternions are four-component vectors that are used extensively to describe spacecraft attitude [22], [162], [223-225]. A four-component vector is defined where  $q_{1-3}$  is known as the vector component and  $q_4$  is the scalar component:

$$\mathbf{q} = \begin{bmatrix} q_1 \\ q_2 \\ q_3 \\ q_4 \end{bmatrix}$$

A 4x4 skew-symmetric matrix generated from the four-vector is commonly defined as [224]:

$$\mathbf{q} = \begin{bmatrix} q_4 & -q_3 & q_2 & q_1 \\ q_3 & q_4 & -q_1 & q_2 \\ -q_2 & q_1 & q_4 & q_3 \\ -q_1 & -q_2 & -q_3 & q_4 \end{bmatrix}$$

The kinematic differential equation for quaternions is thus [225]:

$$\begin{bmatrix} \dot{q}_1 \\ \dot{q}_2 \\ \dot{q}_3 \\ \dot{q}_4 \end{bmatrix} = \frac{1}{2} \begin{bmatrix} q_4 & -q_3 & q_2 & q_1 \\ q_3 & q_4 & -q_1 & q_2 \\ -q_2 & q_1 & q_4 & q_3 \\ -q_1 & -q_2 & -q_3 & q_4 \end{bmatrix} \begin{bmatrix} \omega_1 \\ \omega_2 \\ \omega_3 \\ 0 \end{bmatrix} \quad (36)$$

## C. CLOSED-LOOP EQUATIONS OF MOTION

Closed-loop attitude control systems depend on a comparison of desired attitude to sensed attitude where error is driven to zero by the controller. When using quaternions as the spacecraft attitude representation, this action can be termed “quaternion error feedback” [225]. In this section, we develop the equations of motion for the attitude control of a reaction-wheel-based satellite using quaternion error feedback.

### 1. Satellite Equations of Motion

A mathematical model of the attitude dynamics of a reaction-wheel-based satellite is developed by extending Euler’s rigid body equations [225] to include the momentum stored by the reaction wheels. For a reaction wheel system, angular momentum is conserved in the inertial frame. In the absence of external torques, the rotational dynamics are derived by differentiating the momentum vector with respect to time and setting the derivative to zero. In the inertial frame this derivative is simply:

$$\frac{d}{dt}({}^N\mathbf{H}) = \mathbf{0} \quad (37)$$

where superscript “N” is used to denote a vector referenced to the inertial frame. Since it is generally more convenient to write the system momentum,  $\mathbf{H}$ , in a spacecraft body-fixed frame, the derivative (37) is re-written (using the transport theorem [226]) as:

$$\frac{d}{dt}({}^B\mathbf{H}) + {}^B\boldsymbol{\omega}_{B/N} \times {}^B\mathbf{H} = \mathbf{0} \quad (38)$$

where the vector quantities are now referenced to the body frame, ‘B’.

The total system momentum in the body frame is written as:

$${}^B\mathbf{H} = \mathbf{J}^B \boldsymbol{\omega}_{B/N} + {}^B\mathbf{Z}^{WW} \mathbf{h} \quad (39)$$

where  $\mathbf{J}$  is the body-frame referenced inertia tensor of the spacecraft (including the reaction wheels),  ${}^B\boldsymbol{\omega}_{B/N}$  is the spacecraft angular rate vector and vector  ${}^W\mathbf{h}$  is the vector of reaction wheel momenta about the individual spin axes. Matrix  ${}^B\mathbf{Z}^{WW}$  is a column matrix of unit-vectors relating the reaction wheel spin axes to the body-fixed frame so the product  ${}^B\mathbf{Z}^{WW} \mathbf{h}$  expresses the reaction wheel momentum in the body frame.

Differentiating, the total system momentum in the body frame (39), we have:

$${}^B\dot{\mathbf{H}} = \dot{\mathbf{J}}^B \boldsymbol{\omega}_{B/N} + \mathbf{J}^B \dot{\boldsymbol{\omega}}_{B/N} + {}^B\dot{\mathbf{Z}}^{WW} \mathbf{h} + {}^B\mathbf{Z}^{WW} \dot{\mathbf{h}} \quad (40)$$

Assuming that the spacecraft mass properties are nominally fixed during the period of interest and knowing that the directions of the reaction wheel spin axes are also fixed, the differentiated total system momentum in the body frame equation (40) becomes:

$${}^B\dot{\mathbf{H}} = \mathbf{J}^B \dot{\boldsymbol{\omega}}_{B/N} + {}^B\mathbf{Z}^{WW} \dot{\mathbf{h}} \quad (41)$$

Substituting the total system momentum (39) in the body frame and the reduced differentiated total system momentum in the body frame (41) into the derivative of the system momentum in the body frame (38) gives:

$$\mathbf{J}^B \dot{\boldsymbol{\omega}}_{B/N} + {}^B\mathbf{Z}^{WW} \dot{\mathbf{h}} + {}^B\boldsymbol{\omega}_{B/N} \times \left( \mathbf{J}^B \boldsymbol{\omega}_{B/N} + {}^B\mathbf{Z}^{WW} \mathbf{h} \right) = \mathbf{0} \quad (42)$$

This equation (42) may be rearranged as:

$${}^B \dot{\omega}_{B/N} = \mathbf{J}^{-1} \left( -{}^B \omega_{B/N} \times \mathbf{J} {}^B \omega_{B/N} - {}^B \omega_{B/N} \times {}^B \mathbf{Z}^{WW} \mathbf{h} - {}^B \mathbf{Z}^{WW} \dot{\mathbf{h}} \right) \quad (43)$$

From Sidi [9], the equation for the torque of reaction wheel  $i$  is given as:

$${}^W \tau_i = {}^W \dot{h}_i + J_i^W \left( {}^B \mathbf{Z}_{(i,i)}^W \cdot {}^B \omega_{B/N} \right) \quad (44)$$

The second term on the right-hand side of this equation accounts for the relative motion between the spacecraft and the wheel and can be ignored if the angular rate of the wheel is larger than the rotational rate of the spacecraft, which is normally the case. Thus, either vector  ${}^W \boldsymbol{\tau}$  or vector  ${}^W \dot{\mathbf{h}}$  is considered as the control vector (44) for the system.

To complete the spacecraft model, the attitude kinematics need to be specified. Quaternions are used for this purpose. Taking  $q_4$  as the scalar, the quaternion kinematic differential equations are found in [225] and shown in (36) with:

$$\mathbf{Q}({}^B \omega_{B/N}) = \begin{bmatrix} 0 & \omega_3 & -\omega_2 & \omega_1 \\ -\omega_3 & 0 & \omega_1 & \omega_2 \\ \omega_2 & -\omega_1 & 0 & \omega_3 \\ -\omega_1 & -\omega_2 & -\omega_3 & 0 \end{bmatrix}$$

Selecting the system state vector as  $\mathbf{x} = [\mathbf{q}_{B/N}, {}^B \omega_{B/N}, {}^W \mathbf{h}]^T$  and the control vector as  $\mathbf{u} = {}^W \dot{\mathbf{h}}$ , a system of nonlinear ordinary differential equations including (43) describes the attitude dynamics of the spacecraft and is written as:

$$\dot{\mathbf{x}} = \begin{bmatrix} \dot{\mathbf{q}}_{B/N} \\ {}^B \dot{\omega}_{B/N} \\ {}^W \dot{\mathbf{h}} \end{bmatrix} = \begin{bmatrix} \frac{1}{2} \mathbf{Q}({}^B \omega_{B/N})(\mathbf{q})_{B/N} \\ \mathbf{J}^{-1} \left( -{}^B \omega_{B/N} \times \mathbf{J} {}^B \omega_{B/N} - {}^B \omega_{B/N} \times {}^B \mathbf{Z}^{WW} \mathbf{h} - {}^B \mathbf{Z}^{WW} \dot{\mathbf{h}} \right) \\ \mathbf{u} \end{bmatrix} \quad (45)$$

## 2. Quaternion Error Feedback

The block diagram of a closed-loop quaternion error attitude control system is shown in Figure 18. In this section and for the remainder of this dissertation, the subscripts and superscripts used to denote relative motion and reference frames will be dropped to simplify the equations. The meaning of the variables will be as described previously unless otherwise noted in the text. As seen in Figure 18, the control loop is comprised of a series of blocks designed to determine the control input vector,  $\mathbf{u}$ , which is fed to the reaction wheels. Changes in the wheel momentum produce changes to the spacecraft attitude which results in a desired orientation as specified by the commanded quaternion,  $\mathbf{q}_c$ . A key element of the feedback loop is the attitude estimator that utilizes various sensors such as rate gyroscopes, star-trackers, etc., along with a measurement-fusing filter to estimate the spacecraft attitude and angular rate. The signals output by the attitude estimator are used to evaluate the estimated error quaternion,  $\hat{\mathbf{q}}_e$ , and error rate,  $\hat{\boldsymbol{\omega}}_e = -\hat{\boldsymbol{\omega}}$ . These two error vectors are then processed by the feedback law to generate a vector of feedback torques,  $\boldsymbol{\tau}_{fb}$ , defined in the spacecraft body-fixed frame. An additional torque command,  $\boldsymbol{\tau}_g$ , is injected into the control loop to approximately cancel the gyroscopic torque. The resulting command torque vector,  $\boldsymbol{\tau}_c = \boldsymbol{\tau}_{fb} + \boldsymbol{\tau}_g$  is then mapped to the reaction wheels by a control allocation block, so that the vector of individual wheel commands,  $\mathbf{u}$ , is implemented to change the stored momentum,  $\mathbf{h}$ , of the reaction wheel array. The spacecraft will then respond according to the physics of rotational motion.

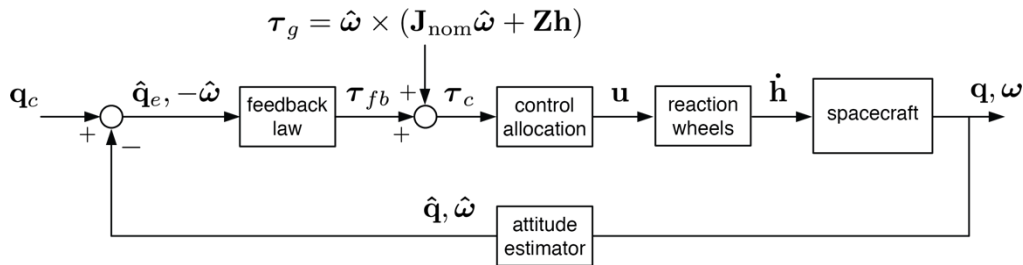


Figure 18. Block Diagram of Closed-loop Quaternion Error Feedback Attitude Control System

In this dissertation, the details of the attitude estimator are not of interest. It is therefore assumed that the signals,  $\hat{\mathbf{q}}$  and  $\hat{\boldsymbol{\omega}}$  are equivalent to  $\mathbf{q}$  and  $\boldsymbol{\omega}$  in Figure 18. Under this assumption, the quaternion error,  $\mathbf{q}_e$ , may be computed as in [9], [225]:

$$\mathbf{q}_e = \begin{bmatrix} \mathbf{v}_e \\ s_e \end{bmatrix} = \mathbf{q}^{-1} \otimes \mathbf{q}_c \quad (46)$$

where superscript “ $\mathbf{q}^{-1}$ ” is used to denote the quaternion conjugate and symbol “ $\otimes$ ” denotes quaternion multiplication. Furthermore, vector  $\mathbf{v}_e$  and scalar  $s_e$  represent the vector and scalar parts of the quaternion error, respectively.

The actual value of the attitude error angle,  $\Phi_e$ , is proxied as the argument of the inverse tangent as described in [225] for eigenaxis rotations under slew rate constraint. The attitude error angle is computed from the quaternion error (46) trajectory using the following equation:

$$\Phi_e = 2 \tan^{-1} \left( \frac{\sum_{i=1}^3 \mathbf{v}_{e,i}^2}{s_e} \right) \quad (47)$$

The quaternion angle error is taken as  $\Phi_e = \pi$  when  $s_e = 0$ .

A practical quaternion error feedback law is given by [31]:

$$\boldsymbol{\tau}_c = -k_p \mathbf{J}_{\text{nom}} \mathcal{N}(\mathbf{v}_e) - k_r \mathbf{J}_{\text{nom}} \boldsymbol{\omega}_e \quad (48)$$

where  $k_p$  and  $k_r$  are suitably chosen “position” and “rate” gains and  $\mathbf{J}_{\text{nom}}$  denotes the assumed (nominal) inertia tensor for the vehicle. Due to imprecise knowledge of the spacecraft mass properties,  $\mathbf{J}_{\text{nom}} \neq \mathbf{J}$ , in general. The nonlinear function  $\mathcal{N}(\mathbf{v}_e)$  is a proportional limiter on the quaternion error that enforces a slew rate limit while simultaneously preserving the direction of the attitude error vector [31]. A slew rate limit is a practical constraint needed to ensure that the gyroscopic torque does not become so large that it exceeds the torque capability of the reaction wheels. In the equation for

quaternion error feedback (48), the proportional limiter implements the following logic [156]:

$$\begin{aligned} & \text{if } \left( \max \left( \left| (2\mathbf{v}_e k_p) / (k_r \omega_{\max}) \right| \right) > 1 \right) \\ & \quad \mathcal{N}(\mathbf{v}_e) = \mathbf{v}_e / \max \left( \left| (2\mathbf{v}_e k_p) / (k_r \omega_{\max}) \right| \right) \\ & \text{else} \\ & \quad \mathcal{N}(\mathbf{v}_e) = \mathbf{v}_e \end{aligned}$$

The command torque  $\boldsymbol{\tau}_c$ , determined by the previously defined feedback law (48), is allocated to the individual wheels by inverting matrix  $\mathbf{Z}$ . For many spacecraft a redundant array of wheels is used to ensure that the three-axis control is maintained in the event of a wheel failure. In this case, matrix  $\mathbf{Z}$  is not a square matrix, so the Moore-Penrose pseudoinverse is used to allocate the command torque to the wheels. The Moore-Penrose pseudoinverse is computed as:

$$\mathbf{Z}^\# = \mathbf{Z}^T (\mathbf{Z}\mathbf{Z}^T)^{-1} \quad (49)$$

When the control allocation is computed, some or all the commanded reaction wheel torques may be larger than the capability of the wheels. Thus, to accommodate the actuator saturation constraints, the actuator commands must be scaled so that  $|u_i| \leq u_{\max}$  for each actuator. To ensure that the torque vector scaling lies in the desired direction, the scaling should be done as follows with (49) from [227]:

$$\mathbf{u} = \eta u_{\max} \frac{\mathbf{Z}^\# \boldsymbol{\tau}_c}{\|\mathbf{Z}^\# \boldsymbol{\tau}_c\|_\infty} \quad (50)$$

where  $\|\cdot\|_\infty$  denotes the max-norm (element of vector  $\mathbf{Z}^\# \boldsymbol{\tau}_c$  with the maximum absolute value) and parameter  $\eta \leq 1$  is a discount factor on the total reaction wheel torque reserved for feedback. The remaining torque authority is allocated for compensation of the gyroscopic torque.

#### D. EXAMPLE CLOSED-LOOP MANEUVER

The quaternion error feedback logic (48) is simulated for an example reorientation maneuver to illustrate how a conventional closed-loop control scheme can desensitize output to errors in knowledge of the system parameters. The dissertation spacecraft parameters listed in Table 3 are used and it is assumed that the uncertainty lies in the knowledge of the spacecraft inertia tensor, specifically, 10% uncertainty in the (1,1) element of the inertia tensor. The simulated maneuver is a rest-to-rest slew through angle  $\Phi = 120$  deg about the spacecraft body  $x$ -axis. Thus, the initial conditions on the satellite attitude and rate are  $\mathbf{q}(t_0) = [0, 0, 0, 1]^T$  and  $\boldsymbol{\omega}(t_0) = [0, 0, 0]^T$  while the commanded offset quaternion is  $\mathbf{q}_c = [\sqrt{3}/2, 0, 0, 1/2]^T$ . The initial momentum bias for the spacecraft is chosen as an arbitrary, but achievable, value of  ${}^B\mathbf{H}(t_0) = [-3.35, 6.91, 0.46]^T$  Nms, which for the reaction wheels translates to  ${}^W\mathbf{h} = [1.72, -4.24, -4.64, 1.32]^T$  Nms. The results of this section were first published in [156].

Figure 19 reports the time history of the attitude error angle,  $\Phi_e$  (47), as the spacecraft maneuvers from the 120 deg  $x$ -axis offset to the final position at zero degrees offset. This maneuver is performed in the closed-loop using error feedback. It is apparent that the closed-loop attitude control system does a very good job of regulating the angle error to zero, despite the uncertainty in the satellite inertia tensor. Using baseline values of the satellite inertias, the closed-loop attitude controller reduces the position (angle) error to less than 0.05 deg at  $t = 313$  seconds.

Figure 20 reports the time history of the angular rate through the closed-loop maneuver. The angular rate response corresponding to the baseline inertia values of the satellite are shown as solid lines. Variation in the body axis rates is shown as shaded “uncertainty tubes” surrounding the nominal (baseline) curve. The satellite rate response adheres to the 0.5 deg/s rate limit imposed on the slew via the proportional limiter. It is also evident that the satellite body rates vary only slightly over the simulation as shown by the small size of the uncertainty tubes. The largest variation in the satellite rate occurs for the body  $x$ -axis.



The satellite momentum (expressed in the body frame) is shown in Figure 21. Similar to Figure 20, the nominal momentum is shown as solid lines and the variations from nominal are shown as shaded uncertainty tubes surrounding the nominal curves. Referring to Figure 21, it is evident that the closed-loop control system functions by adjusting the momentum exchange in response to the attitude and rate feedback in such a way that the slew rate limit is enforced despite the inertia uncertainty. Additionally, the feedback signals are utilized by the closed-loop system to drive the terminal attitude and rate errors toward zero. This desensitizing characteristic of the feedback system is precisely why sensors such as rate gyroscopes need to be used to perform practical reorientation maneuvers.

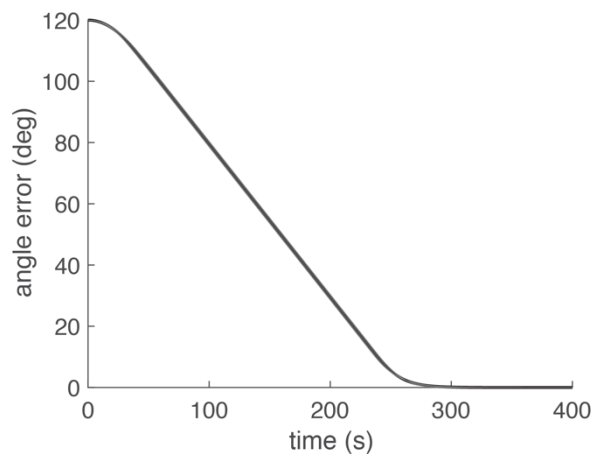


Figure 19. Simulation of Closed-Loop Maneuver Angle Error

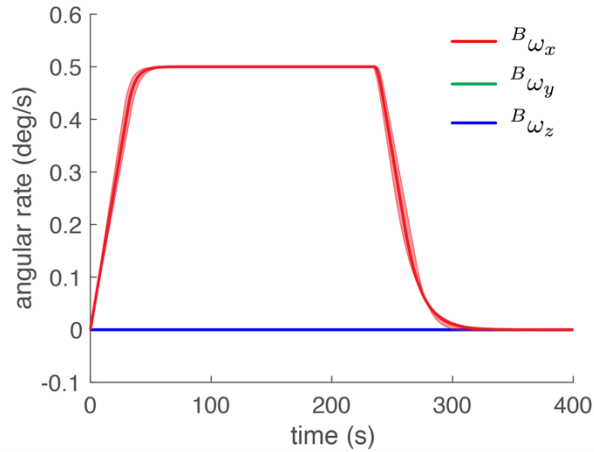


Figure 20. Simulation of Closed-Loop Maneuver Angular Rate in the Body-Frame

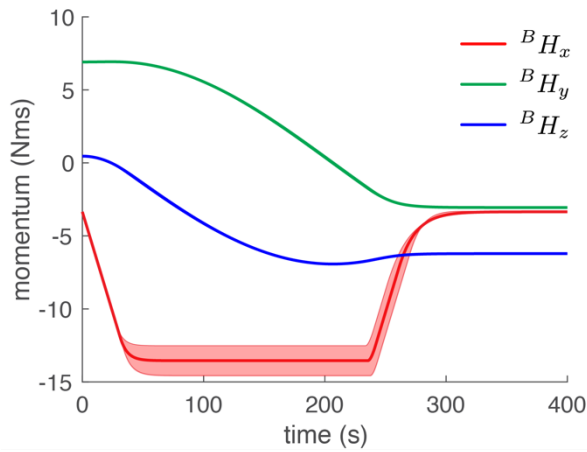


Figure 21. Simulation of Closed-Loop Maneuver Momentum in the Body-Frame

## E. OPEN-LOOP KINEMATIC MANEUVER PROFILE

When the feedback sensors of a closed-loop attitude control system fail, options to continue spacecraft control are limited. Sometimes, spacecraft control can continue in the open-loop. The block diagram of an open-loop attitude control system is shown in Figure 22. As seen in Figure 22, the open-loop system is comprised of a set of blocks designed to implement the control input vector,  $\mathbf{u}$ , that adjusts the reaction wheel momenta which changes the attitude of the spacecraft. Ideally, the open-loop control will achieve the

desired final position. In the presence of uncertainty, however, there may be a significant difference between the desired attitude and the attitude that is achieved by the application of the open-loop control. The results of this section were first published in [157].

To determine the open-loop control vector, a body-frame torque vector,  $\tau_{bf}$ , is constructed from a kinematic maneuver profile about the Eigenaxis and an estimate of the satellite inertia tensor. Such a maneuver is typically a bang-off-bang maneuver (see [227] for details). Using the kinematic maneuver profiles of Figures 23–25, an additional torque command,  $\tau_g$ , is computed and added to the path to approximately cancel the gyroscopic torque. The resulting command torque vector,  $\tau_c = \tau_{bf} + \tau_g$ , is then mapped to the reaction wheels by a control allocation block, so that the vector of individual wheel commands,  $\mathbf{u}$ , is implemented. The spacecraft will then respond according to the physics of rotational motion. A kinematic profile maneuver time of  $t = 313$  sec. was chosen to match the closed-loop solution time. The baseline simulated maneuver is a rest-to-rest slew through angle  $\Phi = 120$  deg about the spacecraft body  $x$ -axis. Thus, the initial conditions on the satellite attitude and rate are  $\mathbf{q}(t_0) = [0, 0, 0, 1]^T$  and  $\boldsymbol{\omega}(t_0) = [0, 0, 0]^T$  while the commanded offset quaternion is  $\mathbf{q}_c = [\sqrt{3}/2, 0, 0, 1/2]^T$ .

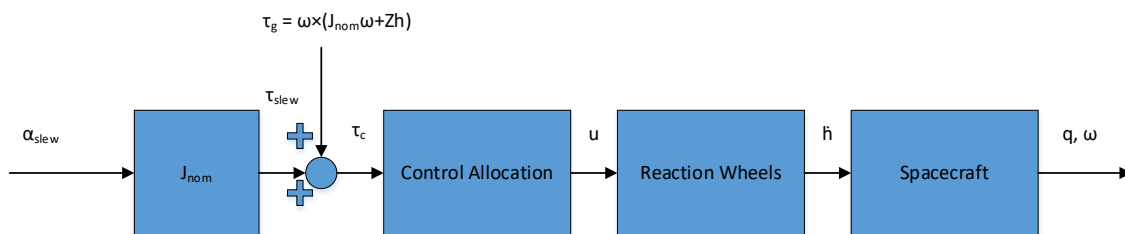


Figure 22. Block Diagram of Open-Loop Attitude Control System

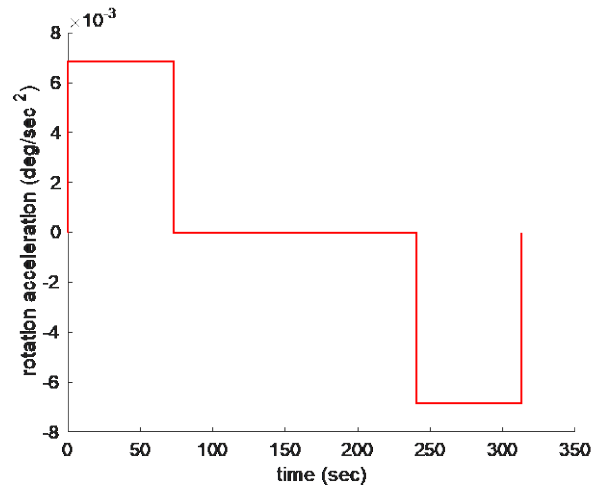


Figure 23. Open-Loop Profile of Maneuver Rotation Acceleration

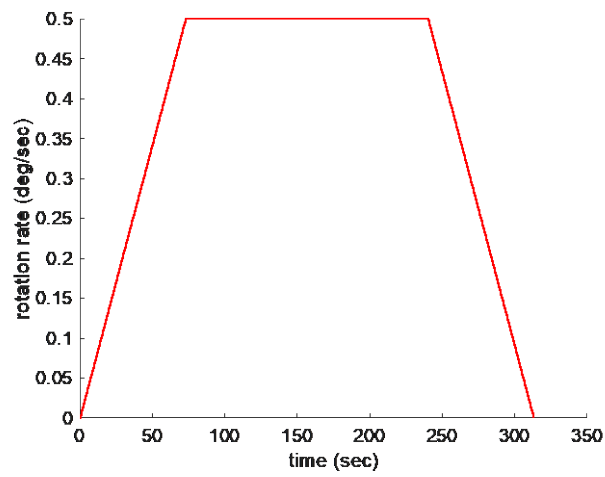


Figure 24. Open-Loop Profile of Maneuver Rotation Rate

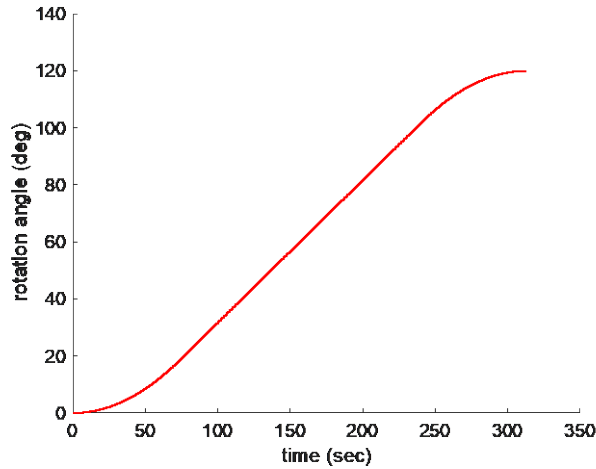


Figure 25. Open-Loop Profile of Maneuver Rotation Angle

#### F. OPEN-LOOP KINEMATIC MANEUVER: SINGLE-AXIS INERTIA UNCERTAINTY

Using the kinematic maneuver profiles, the performance of an open-loop large-angle slew is explored to establish a baseline for open-loop performance and for comparison later against unscented guidance solutions. As specified with the closed-loop slew, it is assumed that the parametric uncertainty lies in the knowledge of the spacecraft inertia tensor. Specifically, 10% uncertainty in the (1,1) element of the inertia tensor will be implemented using the representative spacecraft parameters listed in Table 3. The initial momentum bias for the spacecraft is assumed to be  ${}^B\mathbf{H}(t_0) = [-3.35, 6.91, 0.46]^T$  Nms, which for the reaction wheels translates to  ${}^W\mathbf{h} = [1.72, -4.24, -4.64, 1.32]^T$  Nms. The gyroscopic torque correction in Figure 22 is also computed. The results of this section were first published in [156-157].

Figure 26 reports the time history of the attitude error angle through the open-loop slew from 120 degrees to zero degrees of position error. It is apparent that the open-loop attitude control system does a very poor job of regulating the angle error to zero due to the inherent system uncertainty found in the satellite inertia tensor. When reoriented in the open-loop, a large angle error is developed as seen in the shaded “uncertainty tube” surrounding the baseline curve in Figure 26.

Figure 27 reports the time history of the angular rates of the spacecraft body axes through the slew. The angular rate response for each body axis corresponds to the baseline inertia values of the satellite and are shown as solid lines. Variation in the body axis rates is shown as shaded “uncertainty tubes” surrounding the nominal (baseline) curves. It is evident that the satellite body rates vary considerably over the simulation as shown by the large size of the uncertainty tubes. The largest variation in the satellite rate occurs for the body  $x$ -axis but is present in the body  $y$ -axis and  $z$ -axis as well. It is notable that rate errors are observed about all three body-axes when the maneuver is performed in the open-loop. This is because the gyroscopic torques cannot be properly canceled by the open-loop commands.

The open-loop satellite momentum (expressed in the body frame) is shown in Figure 28. It is observed that the spacecraft body momentum does not show any variation. This is because the system error exists in the inertia tensor, not in the torque profile that is fed into the open-loop controller. In the open-loop, it is not possible to modulate the system momentum to control the error as is done by a closed-loop controller.

Figure 29 shows Monte Carlo simulation results of open-loop kinematic slew terminal pointing errors for  $N=1000$  runs. Using baseline values of the satellite inertias, the average open-loop angle error was calculated to be 5.50 deg and the average value of the rate error was computed as 0.034 deg/sec at  $t = 313$  seconds. Reorienting the spacecraft in the open-loop can lead to large pointing errors, even when the error exists in only one axis.

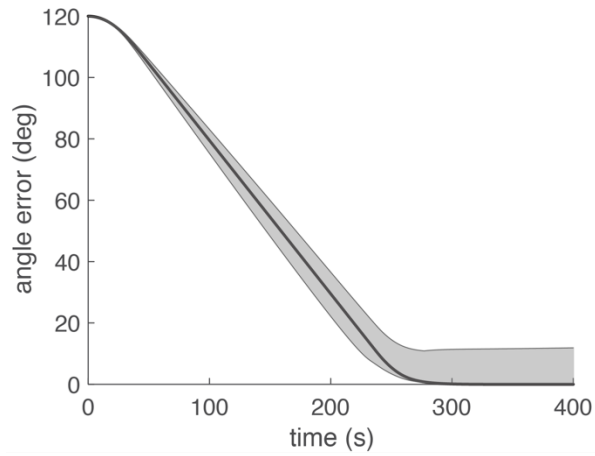


Figure 26. Open-Loop Kinematic Maneuver Angle Error

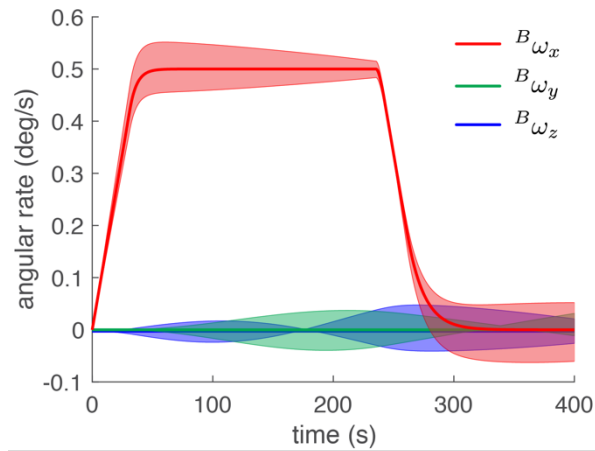


Figure 27. Open-Loop Kinematic Maneuver Body-Frame Angular Rate

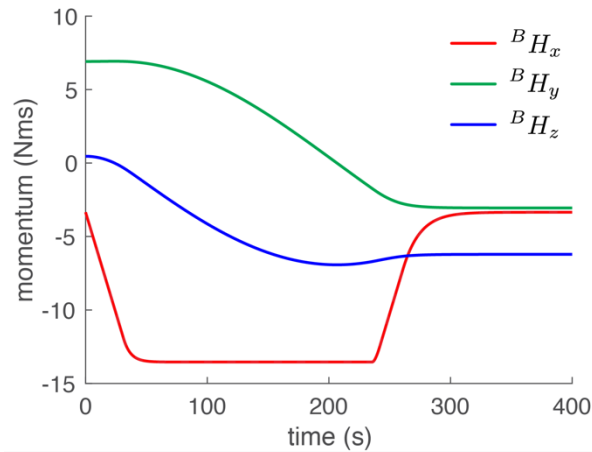


Figure 28. Open-Loop Kinematic Maneuver Body-Frame Spacecraft Momentum

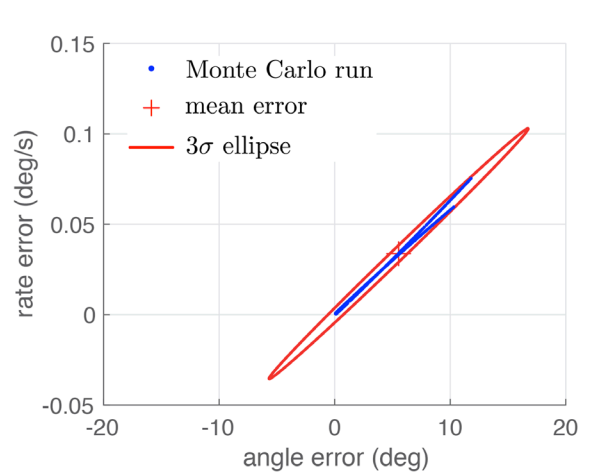


Figure 29. Monte Carlo Simulation Results of Open-Loop Kinematic Slew: Terminal Pointing Errors

## G. OPEN-LOOP KINEMATIC MANEUVER: THREE-AXIS INERTIA UNCERTAINTY

Using the kinematic maneuver profiles, the performance of an open-loop large-angle slew with three-axis uncertainty is explored for comparison with closed-loop and open-loop single-axis uncertainty results. It is assumed that the parametric uncertainty lies in the knowledge of the spacecraft inertia tensor. Specifically, 10% uncertainty in the (1,1),



(2,2) and (3,3) elements of the inertia tensor will be implemented using the dissertation spacecraft parameters listed in Table 3.

Torque profiles were provided to the four reaction wheels to generate a response. These profiles are shown in Figure 30. Position error time history of the three-axis uncertainty 120 degree maneuver is shown in Figure 31. It is apparent that the open-loop attitude control system does a poor job of regulating the angle error to zero due to the uncertainty in the satellite inertia tensor. Angular rate error of the body axes time history is shown in Figure 32. It is evident that like the single axis uncertainty, the satellite body rates increase in variability over the simulation run time indicating cross-coupling in the open-loop dynamics.

The satellite body-frame momentum with three-axis uncertainty is shown in Figure 33. As seen in the single-axis uncertainty problem, the three-axis uncertainty reaction wheel momentum does not show any variation. This behavior happens for the same reason, that there is no error in the torque profile that is fed to the reaction wheels. The error exists in the inertia tensor and without closed-loop feedback, there is no method for that error to manifest in the spacecraft body momentum.

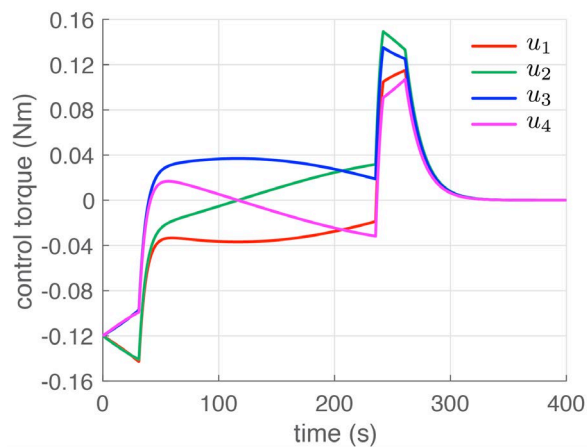


Figure 30. Open-Loop Reaction Wheel Torque Kinematic Maneuver for Three-Axis Uncertainty

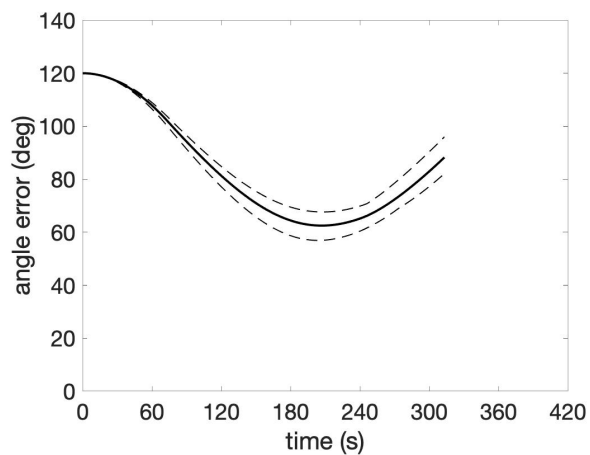


Figure 31. Open-Loop Kinematic Maneuver for Three-Axis Uncertainty Angle Error

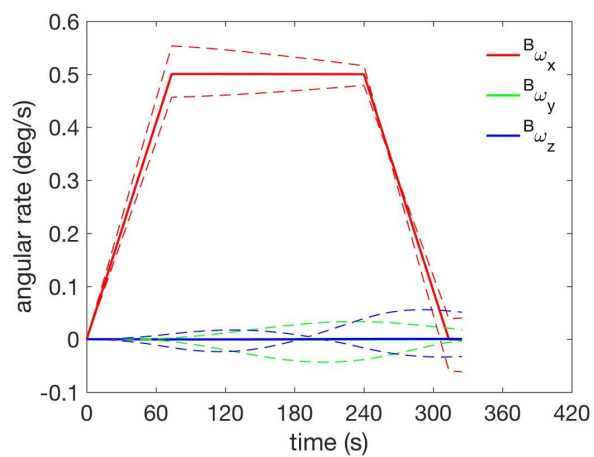


Figure 32. Open-Loop Kinematic Maneuver for Three-Axis Uncertainty Body-Frame Angular Rate

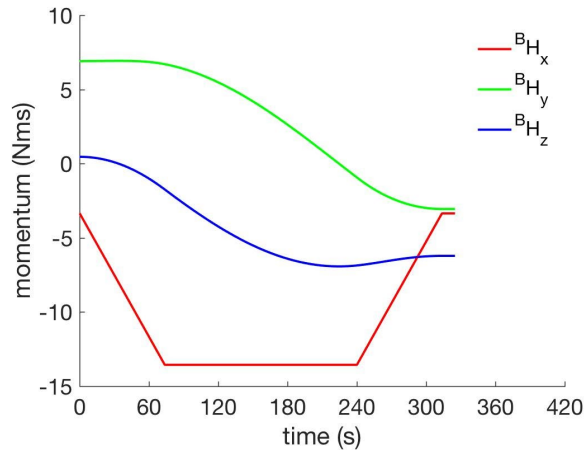


Figure 33. Open-Loop Kinematic Maneuver for Three-Axis Uncertainty Body-Frame Spacecraft Momentum

The average value of the three-axis uncertainty angle error corresponding to nominal inertia values was calculated to be 88.66 deg and the average value of the rate error was computed as 0.430 deg/sec at  $t = 313$  seconds. Reorienting the spacecraft in the open-loop can lead to large pointing errors, as was seen in both the single-axis and three-axis uncertainty results. It is obvious from the scale of these pointing errors, over 88 degrees of error for a 120-degree maneuver with three-axis error present, that open-loop methods for controlling spacecraft are not often used.

## H. CHAPTER SUMMARY

The purpose of this chapter was to discuss conventional reaction-wheel attitude control in both a closed and open-loop approach. A representative spacecraft for use in the dissertation examples was defined as a medium-sized spacecraft with a set of four reaction wheels. This type of spacecraft is quite common as discussed in the background section of this dissertation. Tools for use in building the dissertation MATLAB code such as definition of quaternions, equations of motion, and quaternion error feedback were described. The dissertation spacecraft definition was used with these tools to build an example closed-loop maneuver for which results were provided. Based on the closed-loop results, a set of position, rate and acceleration open-loop kinematic maneuver profiles were created to emulate the 120 degree closed-loop maneuver. These profiles were used to

maneuver the dissertation spacecraft in the open-loop with a single axis of inertia tensor uncertainty. As expected, position and rate of the open-loop maneuver exhibited more error than the comparable closed-loop system. The closed-loop maneuver had an average position error of less than 0.05 deg whereas the open-loop maneuver had an average position error of 5.50 deg. The closed-loop maneuver average rate error was 0.004 deg/sec whereas the open-loop was 0.034 deg/sec. The profiles were further used to maneuver the dissertation spacecraft in the open-loop with three axes of inertia tensor uncertainty. Results for the three-axis inertia uncertainty case were worse than the single-axis uncertainty case. The three-axis uncertainty case had an average position error of 88.66 deg where single-axis uncertainty was 5.50 deg and closed-loop maneuver was less than 0.05 deg. The three-axis uncertainty case had an average rate error of 0.430 deg/sec where single-axis uncertainty had 0.034 deg/sec and closed-loop was 0.004 deg/sec. The results of this chapter demonstrate why open-loop control is rarely used for spacecraft. Errors in the position and rate of the spacecraft are large enough to prevent hand-off to fine guidance sensors. Both the dissertation spacecraft and kinematic maneuver profiles defined in this chapter will be used later in open-loop scenarios of this dissertation.

THIS PAGE INTENTIONALLY LEFT BLANK

## IV. FORMULATION OF UNSCENTED REACTION WHEEL MANEUVER PROBLEM

This chapter sets up the equations necessary to formulate the unscented reaction wheel maneuver optimal control problem. The first step in this formulation is to define a cost functional. This specific cost functional is defined to mitigate the large amount of terminal error observed when closed-loop reaction wheel torque commands are implemented in the open-loop [156]. An unscented guidance problem formulation including sigma points is applied. Necessary conditions for optimality are derived for two versions of the problem. The first version of necessary conditions considers arbitrary momentum bias cases where a known value of momentum bias is provided to the system. The second version of necessary conditions considers the cases when momentum bias is unknown but assumed present, so its value is treated as another variable for which to solve. The unscented reaction wheel maneuver problem formulation is used in the following chapter to provide results of the maneuvering problem.

### A. COST FUNCTIONAL DEFINITION

To solve the unscented reaction wheel maneuver problem using optimal control, a cost functional must be defined that minimizes terminal error. Start by defining an error cost functional. The difference between actual position and desired position at final time gives an error term,  $e$ , as shown in equation (51):

$$J[\mathbf{x}(\cdot), \mathbf{u}(\cdot), t_f] := x(t_f) - x_d(t_f) = e \quad (51)$$

It is desirable to find both mean terminal error as close to zero as possible and variance between  $t_f$  measurements as small as possible. Minimizing the mean squared error of the system provides a measure for both desired qualities. It is also desirable to incorporate parameter uncertainty,  $\mathbf{p}$ . By including parameter uncertainty, the cost functional equation incorporates the distribution of error as a function of distribution of parameter uncertainty. The squared errors add to be the total system cost which is desired

to be as small as possible. The cost functional for mean squared error with parameter uncertainty is:

$$J[\mathbf{x}(\cdot, \cdot), \mathbf{u}(\cdot), t_f; \mathbf{p}] := \frac{1}{N} \sum_{j=1}^N e_j^2(t_f, \mathbf{p}); \mathbf{p}_j \quad (52)$$

This cost functional definition (52) is easily used by any sampling technique to develop a solution. For example, Monte Carlo can be used to sample the problem with  $N=1000$  or greater points. Other sampling techniques such as multidimensional approximation or unscented guidance can use  $N$  sampling points as small as three with similar statistical results.

## B. UNSCENTED REACTION WHEEL MANEUVER COST FUNCTIONAL

The mean squared error with parameter uncertainty cost functional (52) is changed to be the unscented reaction wheel maneuver cost functional used for analysis in this dissertation. The errors that are desired to be minimized are quaternion vector distance,  $v$ , and vehicle angular rate,  $\omega$ . The unscented guidance sampling weights,  $w_i$ , are applied to the squared sum of errors for the three quaternion vector quantities and three angular rate vectors. The fourth quaternion, a scalar  $s_e$ , is applied as a scaling function to the sum of vector quaternion errors. This unscented reaction wheel maneuver cost functional is:

$$J[\mathbf{x}_1(\cdot, \mathbf{p}), \dots, \mathbf{x}_n(\cdot, \mathbf{p}), \mathbf{u}(\cdot), t_f; \mathbf{p}] := \sum_{i=1}^n w_i \left( \kappa_1 \frac{1}{s_e} \sum_{j=1}^3 v_{e,j}^2(\mathbf{x}(\cdot, \mathbf{p}), \mathbf{u}(\cdot), t_f; \mathbf{p}_i) + \kappa_2 \frac{1}{s_e} \sum_{j=1}^3 \omega_{e,j}^2(\mathbf{x}(\cdot, \mathbf{p}), \mathbf{u}(\cdot), t_f; \mathbf{p}_i) \right) \quad (53)$$

where  $\kappa_1$  and  $\kappa_2$  are weights on the terminal attitude and rate errors, respectively. A solution to this problem (53) should minimize the variance of terminal pointing error for an open-loop slew in the presence of inertia tensor uncertainty.

In this dissertation, the focus is first to mitigate the effects of uniform uncertainty in the (1, 1) element of the inertia tensor. The standard uniform distribution  $\mathcal{U}(0,1)$  may be represented up to the third-order central moment using a set of only three spherical simplex sigma points [155]:

$$\chi_1 = 0, \quad \chi_2 = \frac{1}{\sqrt{2w_2}}, \quad \chi_3 = -\frac{1}{\sqrt{2w_3}}$$

with the weights:

$$w_1 = \frac{1}{4}, \quad w_2 = \frac{3}{8}, \quad w_3 = \frac{3}{8}$$

The sigma points so far derived are for standard distributions with zero mean and uniform covariance. To apply the sigma points' sampling to the uncertainty associated with the inertia tensor, the points need to be shifted and scaled to match the mean,  $\mathbf{J}_{nom}$ , and covariance,  $\mathbf{P}$ , of the problem data. The scaling is done by applying the following transform to get the inertia tensors for unscented guidance:

$$\mathbf{J}_i = \text{diag}\left(\mathbf{J}_{nom} + \sqrt{\mathbf{P}}\chi_i\right) \quad (54)$$

In the transform (54),  $i = 1, 2, \dots, N_p + 2$  (spherical simplex points) and  $\sqrt{\mathbf{P}}$  is the matrix square root of  $\mathbf{P}$ , which is computed as the Cholesky decomposition of  $\mathbf{P}$  (a symmetric positive definite matrix).

Now that the sigma points have been defined, the next step is to create an ensemble of models to form the unscented guidance problem that minimizes the cost functional. Since the cost functional utilizes quaternion error, the differential equations associated with quaternion error are utilized in lieu of quaternions. The quaternion error differential equations are:

$$\dot{\mathbf{q}}_e = \mathbf{q}^{-1} \otimes \dot{\mathbf{q}}_c + \dot{\mathbf{q}}^{-1} \otimes \mathbf{q}_c \quad (55)$$

This quaternion error differential equation (55) is simplified by noting that the commanded quaternion,  $\mathbf{q}_c$ , is constant for a reorientation maneuver:

$$\dot{\mathbf{q}}_e = \left[ \frac{1}{2} \mathbf{Q}(\omega) \mathbf{q}^{-1} \right] \otimes \mathbf{q}_c \quad (56)$$



Using this simplified quaternion error differential equation (56), the unscented reaction wheel maneuver problem that is time-free and uses three sigma points for sampling is formulated using (45) and (50). The quaternion error, vehicle rate and momentum bias terms are defined as  $\mathbf{q}_e$ ,  $\boldsymbol{\omega}$ , and  $\mathbf{h}$ . The  $\mathbf{q}_e$  vector has four terms in the body frame while the  $\boldsymbol{\omega}$  vector has three terms in the body frame. The  $\mathbf{h}$  vector has four terms in the wheel frame which is easily converted to the body frame by using the reaction wheel alignment matrix,  $\mathbf{Z}$ , to convert it to three terms. The total of vector terms for the unscented reaction wheel maneuver is eleven. These eleven terms exist at each of the three sigma points, giving a total of thirty-three differential equations which is the size of the real valued space for  $\mathbf{x}$ . The size of the control space,  $\mathbf{u}$ , is four, one for each of the wheel-frame  $\mathbf{h}$  terms as defined in the dynamics equations. Initial conditions are provided for  $\mathbf{q}_e$ ,  $\boldsymbol{\omega}$ , and  $\mathbf{h}$ . The quaternion error initial condition,  $\mathbf{q}_e$  at  $t_0$ , is the desired offset which for the examples within this dissertation is a 120 degree  $x$ -axis (roll) maneuver. The spacecraft body rate initial condition,  $\boldsymbol{\omega}$  at  $t_0$ , is zero degrees/second. The initial value of momentum bias,  $\mathbf{h}$  at  $t_0$ , is defined for the reaction wheels as  ${}^w\mathbf{h} = [1.72, -4.24, -4.64, 1.32]^T$  Nms which is chosen arbitrarily but within the capabilities of the spacecraft reaction wheels.

Final conditions are specified for a subset of the dynamics terms. The quaternion error final condition,  $\mathbf{q}_e$  at  $t_f$ , is specified for the first (nominal) sigma point only. Sigma points 2–3 are free to complete the maneuver within the statistically relevant space. Momentum at final time on the reaction wheels is defined to be the same as initial values, a requirement for this problem. It is not always a requirement that the initial and final momentum values be the same, as will be seen in the optimum momentum bias version of this problem. For this arbitrary momentum bias problem, the wheel momentum values at initial and final time are chosen to be the same. Spacecraft body rate at both initial and final time are zero since this is a rest-to-rest maneuver. The optimal control problem definition for an unscented reaction wheel maneuver with arbitrary momentum bias is shown as [156-157]:

$$\mathbf{x} := [(\mathbf{q}_1, \boldsymbol{\omega}_1, \mathbf{h}_1), (\mathbf{q}_2, \boldsymbol{\omega}_2, \mathbf{h}_2), (\mathbf{q}_3, \boldsymbol{\omega}_3, \mathbf{h}_3)] \in \mathbb{R}^{33}$$

$$\begin{aligned}
\mathbf{u} \in \mathbb{U} &:= \left\{ (u_1, u_2, u_3, u_4) \in \mathbb{R}^4 \right\} \\
(ZF_{arb}) \left\{ \begin{array}{ll} \text{Minimize} & J[\mathbf{x}_1(\cdot; \mathbf{p}), \dots, \mathbf{x}_n(\cdot; \mathbf{p}), \mathbf{u}(\cdot), t_f; \mathbf{p}] := \sum_{i=1}^n w_i \left( \kappa_1 \frac{1}{s_e} \sum_{j=1}^3 v_{e,j}^2(\mathbf{x}(\cdot; \mathbf{p}), \mathbf{u}(\cdot), t_f; \mathbf{p}_i) + \kappa_2 \frac{1}{s_e} \sum_{j=1}^3 \omega_{e,j}^2(\mathbf{x}(\cdot; \mathbf{p}), \mathbf{u}(\cdot), t_f; \mathbf{p}_i) \right) \\ \text{Subject to} & \begin{aligned} \dot{\mathbf{q}}_{e,1}(t, \mathbf{J}_1) &= \frac{1}{2} \mathbf{Q}(\omega_1) \mathbf{q}_1^{-1} \otimes \mathbf{q}_e \\ &\vdots \\ \dot{\mathbf{q}}_{e,n}(t, \mathbf{J}_n) &= \frac{1}{2} \mathbf{Q}(\omega_n) \mathbf{q}_n^{-1} \otimes \mathbf{q}_e \\ \dot{\omega}_1(t, \mathbf{J}_1) &= \mathbf{J}_1^{-1} (\omega_1 \times \mathbf{J}_1 \omega_1 - \omega_1 \times \mathbf{Z} \mathbf{h} - \mathbf{Z} \dot{\mathbf{h}}) \\ &\vdots \\ \dot{\omega}_n(t, \mathbf{J}_n) &= \mathbf{J}_n^{-1} (\omega_n \times \mathbf{J}_n \omega_n - \omega_n \times \mathbf{Z} \mathbf{h} - \mathbf{Z} \dot{\mathbf{h}}) \\ \dot{\mathbf{h}}(t) &= \mathbf{u} \\ (\mathbf{q}_i(t_0), \omega_i(t_0), \mathbf{h}(t_0)) &= (\mathbf{q}_e, \mathbf{0}_{3 \times 1}, {}^W \mathbf{h}^0) \\ \mathbf{q}_1(t_f) &= [0, 0, 0, 1]^T \\ (\omega_i(t_f), \mathbf{h}(t_f)) &= (\mathbf{0}_{3 \times 1}, {}^W \mathbf{h}^f) \\ |u_k| &\leq u_{\max} \quad \forall k = 1, 2, 3, 4 \\ \mathbf{J}_i &= \text{diag}(\mathbf{J}_{nom} + \sqrt{\mathbf{P}} \chi_i) \quad \forall i = 1, 2, 3 \\ \mathbf{p}_i &\in \text{supp}(\mathbf{p}) \quad \forall i = 1, 2, 3 \end{aligned} \end{aligned} \right.
\end{aligned} \tag{57}$$

In the unscented reaction wheel maneuver problem formulated here (57), we seek a control torque trajectory to drive the nominal plant to the desired quaternion subject to the torque capacity of the reaction wheel array. The absolute value of the torque is a path constraint on the control trajectory. Moreover, the average terminal offset error variance will be minimized over the considered uncertainty in the satellite inertia tensor. The final momenta of the reaction wheels are specified by considering the conservation of angular momentum in the inertial frame.

### C. NECESSARY CONDITIONS FOR ARBITRARY MOMENTUM BIAS

A set of necessary conditions that a candidate optimal control solution to the unscented reaction wheel maneuver with arbitrary momentum bias ( $ZF_{arb}$ ) problem must satisfy is found by developing Pontryagin's necessary conditions for optimality as outlined in the example Zermelo problems [164]. The necessary conditions are derived as follows:

1. Construct the Hamiltonian
2. Develop the Adjoint equations

3. Minimize the Hamiltonian
4. Construct the Endpoint Lagrangian
5. Determine transversality conditions
6. Evaluate the Hamiltonian value condition
7. Analyze the Hamiltonian evolution equation

### **Construct the Hamiltonian(s)**

The problem formulation defines:

$$\mathbf{x} = \begin{bmatrix} \mathbf{q} \\ \mathbf{\omega} \\ \mathbf{h} \end{bmatrix} \in \mathbb{R}^{33}$$

It follows that:

$$\boldsymbol{\lambda} \in \mathbb{R}^{33}$$

Due to the lengthy nature of these derivations, only a portion of them will be shown, specifically one set of eleven equations that describe the first sigma point. The process of deriving each set of equations will need to be repeated for the two following sigma points although those equations are not shown here.

The adjoint co-vectors for the first sigma point are defined as the following (58):

$$\lambda := \begin{bmatrix} \lambda_{q_1} \\ \lambda_{q_2} \\ \lambda_{q_3} \\ \lambda_{q_4} \\ \lambda_{\omega_1} \\ \lambda_{\omega_2} \\ \lambda_{\omega_3} \\ \lambda_{h_1} \\ \lambda_{h_2} \\ \lambda_{h_3} \\ \lambda_{h_4} \end{bmatrix}$$

(58)

The transpose of the co-vectors for the first sigma point is given by:

$$\lambda^T = \begin{bmatrix} \lambda_{q_1} & \lambda_{q_2} & \lambda_{q_3} & \lambda_{q_4} & \lambda_{\omega_1} & \lambda_{\omega_2} & \lambda_{\omega_3} & \lambda_{h_1} & \lambda_{h_2} & \lambda_{h_3} & \lambda_{h_4} \end{bmatrix}$$

The dynamics of  $ZF_{arb}$  for the first sigma point include initial momentum bias,  $H_0$ , reaction wheel momentum,  $h_B$ , and control torque,  $u_B$ , in the body frame and control torque,  $u_w$ , in the wheel frame as described by:

$$\mathbf{f} = \begin{bmatrix} \frac{1}{2}[\omega_3 q_2 - \omega_2 q_3 + \omega_1 q_4] \\ \frac{1}{2}[-\omega_3 q_1 + \omega_1 q_3 + \omega_2 q_4] \\ \frac{1}{2}[\omega_2 q_1 - \omega_1 q_2 + \omega_3 q_4] \\ \frac{1}{2}[-\omega_1 q_1 - \omega_2 q_2 - \omega_3 q_3] \\ \frac{1}{J_1}[J_2 \omega_2 \omega_3 - J_3 \omega_2 \omega_3 - \omega_2 h_{B3} + \omega_3 h_{B2} - u_{B1}] \\ \frac{1}{J_2}[J_3 \omega_3 \omega_1 - J_1 \omega_3 \omega_1 - \omega_3 h_{B1} + \omega_1 h_{B3} - u_{B2}] \\ \frac{1}{J_3}[J_1 \omega_1 \omega_2 - J_2 \omega_1 \omega_2 - \omega_1 h_{B2} + \omega_2 h_{B1} - u_{B3}] \\ \\ u_{w1} \\ u_{w2} \\ u_{w3} \\ u_{w4} \end{bmatrix}$$

The  $ZF_{arb}$  Hamiltonian equation for the first sigma point is given by (59):

$$H(\boldsymbol{\lambda}, \mathbf{x}, \mathbf{u}) = 0 + \begin{bmatrix} \lambda_{q_1} & \lambda_{q_2} & \lambda_{q_3} & \lambda_{q_4} & \lambda_{\omega_1} & \lambda_{\omega_2} & \lambda_{\omega_3} & \lambda_{h_1} & \lambda_{h_2} & \lambda_{h_3} & \lambda_{h_4} & \begin{bmatrix} \frac{1}{2}[\omega_3 q_2 - \omega_2 q_3 + \omega_1 q_4] \\ \frac{1}{2}[-\omega_3 q_1 + \omega_1 q_3 + \omega_2 q_4] \\ \frac{1}{2}[\omega_2 q_1 - \omega_1 q_2 + \omega_3 q_4] \\ \frac{1}{2}[-\omega_1 q_1 - \omega_2 q_2 - \omega_3 q_3] \\ \frac{1}{J_1}[J_2 \omega_2 \omega_3 - J_3 \omega_2 \omega_3 - \omega_2 h_{B3} + \omega_3 h_{B2} - u_{B1}] \\ \frac{1}{J_2}[J_3 \omega_3 \omega_1 - J_1 \omega_3 \omega_1 - \omega_3 h_{B1} + \omega_1 h_{B3} - u_{B2}] \\ \frac{1}{J_3}[J_1 \omega_1 \omega_2 - J_2 \omega_1 \omega_2 - \omega_1 h_{B2} + \omega_2 h_{B1} - u_{B3}] \\ u_{W1} \\ u_{W2} \\ u_{W3} \\ u_{W4} \end{bmatrix} \end{bmatrix} \quad (59)$$

Re-writing the  $ZF_{arb}$  Hamiltonian for the first sigma point is then (60):

$$\begin{aligned} H(\boldsymbol{\lambda}, \mathbf{x}, \mathbf{u}) &= \lambda_{q_1} \left[ \frac{1}{2}[\omega_3 q_2 - \omega_2 q_3 + \omega_1 q_4] \right] + \lambda_{q_2} \left[ \frac{1}{2}[-\omega_3 q_1 + \omega_1 q_3 + \omega_2 q_4] \right] + \dots \\ &\lambda_{q_3} \left[ \frac{1}{2}[\omega_2 q_1 - \omega_1 q_2 + \omega_3 q_4] \right] + \lambda_{q_4} \left[ \frac{1}{2}[-\omega_1 q_1 - \omega_2 q_2 - \omega_3 q_3] \right] + \dots \\ &\lambda_{\omega_1} \left[ \frac{1}{J_1}[J_2 \omega_2 \omega_3 - J_3 \omega_2 \omega_3 - \omega_2 h_{B3} + \omega_3 h_{B2} - u_{B1}] \right] + \dots \\ &\lambda_{\omega_2} \left[ \frac{1}{J_2}[J_3 \omega_3 \omega_1 - J_1 \omega_3 \omega_1 - \omega_3 h_{B1} + \omega_1 h_{B3} - u_{B2}] \right] + \dots \\ &\lambda_{\omega_3} \left[ \frac{1}{J_3}[J_1 \omega_1 \omega_2 - J_2 \omega_1 \omega_2 - \omega_1 h_{B2} + \omega_2 h_{B1} - u_{B3}] \right] + \dots \\ &\lambda_{h_1} [u_{W1}] + \lambda_{h_2} [u_{W2}] + \lambda_{h_3} [u_{W3}] + \lambda_{h_4} [u_{W4}] \end{aligned} \quad (60)$$

The  $ZF_{arb}$  problem constrains the control, so the Lagrangian of the Hamiltonian ( $\bar{H}$ ) for the first sigma point must be defined using (5):

$$\bar{H}(\boldsymbol{\mu}, \boldsymbol{\lambda}, \mathbf{x}, \mathbf{u}) := H(\boldsymbol{\lambda}, \mathbf{x}, \mathbf{u}) + \boldsymbol{\mu}^T \mathbf{h}(\mathbf{u})$$

A path co-vector ( $\mu$ ) is added to the original Hamiltonian for each control  $u$  which gives the Lagrangian of the Hamiltonian for the first sigma point of the arbitrary momentum bias problem as (61):

$$\begin{aligned} \bar{H}(\boldsymbol{\mu}, \boldsymbol{\lambda}, \mathbf{x}, \mathbf{u}) = & \lambda_{q_1} \left[ \frac{1}{2} [\omega_3 q_2 - \omega_2 q_3 + \omega_1 q_4] \right] + \lambda_{q_2} \left[ \frac{1}{2} [-\omega_3 q_1 + \omega_1 q_3 + \omega_2 q_4] \right] + \dots \\ & \lambda_{q_3} \left[ \frac{1}{2} [\omega_2 q_1 - \omega_1 q_2 + \omega_3 q_4] \right] + \lambda_{q_4} \left[ \frac{1}{2} [-\omega_1 q_1 - \omega_2 q_2 - \omega_3 q_3] \right] + \dots \\ & \lambda_{\omega_1} \left[ \frac{1}{J_1} [J_2 \omega_2 \omega_3 - J_3 \omega_2 \omega_3 - \omega_2 h_{B3} + \omega_3 h_{B2} - u_{B1}] \right] + \dots \\ & \lambda_{\omega_2} \left[ \frac{1}{J_2} [J_3 \omega_3 \omega_1 - J_1 \omega_3 \omega_1 - \omega_3 h_{B1} + \omega_1 h_{B3} - u_{B2}] \right] + \dots \\ & \lambda_{\omega_3} \left[ \frac{1}{J_3} [J_1 \omega_1 \omega_2 - J_2 \omega_1 \omega_2 - \omega_1 h_{B2} + \omega_2 h_{B1} - u_{B3}] \right] + \dots \\ & \lambda_{h_1} [u_{w1}] + \lambda_{h_2} [u_{w2}] + \lambda_{h_3} [u_{w3}] + \lambda_{h_4} [u_{w4}] + \dots \\ & \mu_{u_1} [u_{w1}] + \mu_{u_2} [u_{w2}] + \mu_{u_3} [u_{w3}] + \mu_{u_4} [u_{w4}] \end{aligned} \quad (61)$$

### Develop the adjoint equations

The adjoint equations are found by taking the partial derivative of the Hamiltonian with respect to  $\mathbf{q}$ ,  $\boldsymbol{\omega}$  and  $\mathbf{h}$ . To properly derive the adjoint equations for  $\mathbf{h}$ , the momentum terms must be re-written in the wheel frame using appropriate terms from the reaction wheel alignment matrix,  $\mathbf{Z}$ . This change affects the rate equations which can be re-written for the first sigma point as (62):

$$\begin{aligned}
& \lambda_{\omega_1} \left[ \frac{1}{J_1} [J_2 \omega_2 \omega_3 - J_3 \omega_2 \omega_3 - \omega_2 h_{B3} + \omega_3 h_{B2} - u_{B1}] \right] = \dots \\
& \lambda_{\omega_1} \left[ \frac{1}{J_1} [J_2 \omega_2 \omega_3 - J_3 \omega_2 \omega_3] \right] + \dots \\
& \lambda_{\omega_1} \left[ \frac{1}{J_1} [-\omega_2 (Z_{31} h_{W1} + Z_{32} h_{W2} + Z_{33} h_{W3} + Z_{34} h_{W4})] \right] + \dots \\
& \lambda_{\omega_1} \left[ \frac{1}{J_1} [\omega_3 (Z_{21} h_{W1} + Z_{22} h_{W2} + Z_{23} h_{W3} + Z_{24} h_{W4})] \right] + \dots \\
& \lambda_{\omega_1} \left[ \frac{1}{J_1} [- (Z_{11} \dot{h}_{W1} + Z_{12} \dot{h}_{W2} + Z_{13} \dot{h}_{W3} + Z_{14} \dot{h}_{W4})] \right] \\
\\
& \lambda_{\omega_2} \left[ \frac{1}{J_2} [J_3 \omega_3 \omega_1 - J_1 \omega_3 \omega_1 - \omega_3 h_{B1} + \omega_1 h_{B3} - u_{B2}] \right] = \dots \\
& \lambda_{\omega_2} \left[ \frac{1}{J_2} [J_3 \omega_3 \omega_1 - J_1 \omega_3 \omega_1] \right] + \dots \\
& \lambda_{\omega_2} \left[ \frac{1}{J_2} [-\omega_3 (Z_{11} h_{W1} + Z_{12} h_{W2} + Z_{13} h_{W3} + Z_{14} h_{W4})] \right] + \dots \\
& \lambda_{\omega_2} \left[ \frac{1}{J_2} [\omega_1 (Z_{31} h_{W1} + Z_{32} h_{W2} + Z_{33} h_{W3} + Z_{34} h_{W4})] \right] + \dots \\
& \lambda_{\omega_2} \left[ \frac{1}{J_2} [- (Z_{21} \dot{h}_{W1} + Z_{22} \dot{h}_{W2} + Z_{23} \dot{h}_{W3} + Z_{24} \dot{h}_{W4})] \right] \\
\\
& \lambda_{\omega_3} \left[ \frac{1}{J_3} [J_1 \omega_1 \omega_2 - J_2 \omega_1 \omega_2 - \omega_1 h_{B2} + \omega_2 h_{B1} - u_{B3}] \right] = \dots \\
& \lambda_{\omega_3} \left[ \frac{1}{J_3} [J_1 \omega_1 \omega_2 - J_2 \omega_1 \omega_2] \right] + \dots \\
& \lambda_{\omega_3} \left[ \frac{1}{J_3} [-\omega_1 (Z_{21} h_{W1} + Z_{22} h_{W2} + Z_{23} h_{W3} + Z_{24} h_{W4})] \right] + \dots \\
& \lambda_{\omega_3} \left[ \frac{1}{J_3} [\omega_2 (Z_{11} h_{W1} + Z_{12} h_{W2} + Z_{13} h_{W3} + Z_{14} h_{W4})] \right] + \dots \\
& \lambda_{\omega_3} \left[ \frac{1}{J_3} [- (Z_{31} \dot{h}_{W1} + Z_{32} \dot{h}_{W2} + Z_{33} \dot{h}_{W3} + Z_{34} \dot{h}_{W4})] \right]
\end{aligned}$$

(62)



The ZF<sub>arb</sub> adjoint equations for the first sigma point are thus (63):

$$\begin{aligned}
-\frac{\partial H}{\partial q_1} &= \dot{\lambda}_{q_1} = \frac{1}{2} \lambda_{q_2} \omega_3 - \frac{1}{2} \lambda_{q_3} \omega_2 + \frac{1}{2} \lambda_{q_4} \omega_1 \\
-\frac{\partial H}{\partial q_2} &= \dot{\lambda}_{q_2} = -\frac{1}{2} \lambda_{q_1} \omega_3 + \frac{1}{2} \lambda_{q_3} \omega_1 + \frac{1}{2} \lambda_{q_4} \omega_2 \\
-\frac{\partial H}{\partial q_3} &= \dot{\lambda}_{q_3} = \frac{1}{2} \lambda_{q_1} \omega_2 - \frac{1}{2} \lambda_{q_2} \omega_1 + \frac{1}{2} \lambda_{q_4} \omega_3 \\
-\frac{\partial H}{\partial q_4} &= \dot{\lambda}_{q_4} = -\frac{1}{2} \lambda_{q_1} \omega_1 - \frac{1}{2} \lambda_{q_2} \omega_2 - \frac{1}{2} \lambda_{q_3} \omega_3 \\
-\frac{\partial H}{\partial \omega_1} &= \dot{\lambda}_{\omega_1} = -\frac{1}{2} \lambda_{q_1} q_4 - \frac{1}{2} \lambda_{q_2} q_3 + \frac{1}{2} \lambda_{q_3} q_2 + \frac{1}{2} \lambda_{q_4} q_1 + \dots \\
&\lambda_{\omega_2} \left[ \frac{1}{J_2} [-J_3 \omega_3 + J_1 \omega_3 - h_{B3}] \right] + \lambda_{\omega_3} \left[ \frac{1}{J_3} [-J_1 \omega_2 + J_2 \omega_2 + h_{B2}] \right] \\
-\frac{\partial H}{\partial \omega_2} &= \dot{\lambda}_{\omega_2} = \frac{1}{2} \lambda_{q_1} q_3 - \frac{1}{2} \lambda_{q_2} q_4 - \frac{1}{2} \lambda_{q_3} q_1 + \frac{1}{2} \lambda_{q_4} q_2 + \dots \\
&\lambda_{\omega_1} \left[ \frac{1}{J_1} [-J_2 \omega_3 + J_3 \omega_3 + h_{B3}] \right] + \lambda_{\omega_3} \left[ \frac{1}{J_3} [-J_1 \omega_1 + J_2 \omega_2 - h_{B1}] \right] \\
-\frac{\partial H}{\partial \omega_3} &= \dot{\lambda}_{\omega_3} = -\frac{1}{2} \lambda_{q_1} q_2 + \frac{1}{2} \lambda_{q_2} q_1 - \frac{1}{2} \lambda_{q_3} q_4 + \frac{1}{2} \lambda_{q_4} q_3 + \dots \\
&\lambda_{\omega_1} \left[ \frac{1}{J_1} [-J_2 \omega_2 + J_3 \omega_2 - h_{B2}] \right] + \lambda_{\omega_2} \left[ \frac{1}{J_2} [-J_3 \omega_1 + J_1 \omega_1 + h_{B1}] \right] \\
-\frac{\partial H}{\partial h_1} &= \dot{\lambda}_{h_1} = \lambda_{\omega_1} \left[ \frac{1}{J_1} [-\omega_2 (2^* Z_{31}) + \omega_3 (2^* Z_{21}) - Z_{11} \ddot{h}_{w1}] \right] + \dots \\
&\lambda_{\omega_2} \left[ \frac{1}{J_2} [-\omega_3 (2^* Z_{11}) + \omega_1 (2^* Z_{31}) - Z_{21} \ddot{h}_{w1}] \right] + \dots \\
&\lambda_{\omega_3} \left[ \frac{1}{J_3} [-\omega_1 (2^* Z_{21}) + \omega_2 (2^* Z_{11}) - Z_{31} \ddot{h}_{w1}] \right] + \dots \\
&\lambda_{h_1} \ddot{h}_{w1}
\end{aligned}$$

$$\begin{aligned}
-\frac{\partial H}{\partial h_2} &= \dot{\lambda}_{h_2} = \lambda_{\omega_1} \left[ \frac{1}{J_1} \left[ -\omega_2 (2^* Z_{32}) + \omega_3 (2^* Z_{22}) - Z_{12} \ddot{h}_{w2} \right] \right] + \dots \\
&\lambda_{\omega_2} \left[ \frac{1}{J_2} \left[ -\omega_3 (2^* Z_{12}) + \omega_1 (2^* Z_{32}) - Z_{22} \ddot{h}_{w2} \right] \right] + \dots \\
&\lambda_{\omega_3} \left[ \frac{1}{J_3} \left[ -\omega_1 (2^* Z_{22}) + \omega_2 (2^* Z_{12}) - Z_{32} \ddot{h}_{w2} \right] \right] + \dots \\
&\lambda_{h_2} \ddot{h}_{w2} \\
\\
-\frac{\partial H}{\partial h_3} &= \dot{\lambda}_{h_3} = \lambda_{\omega_1} \left[ \frac{1}{J_1} \left[ -\omega_2 (2^* Z_{33}) + \omega_3 (2^* Z_{23}) - Z_{13} \ddot{h}_{w3} \right] \right] + \dots \\
&\lambda_{\omega_2} \left[ \frac{1}{J_2} \left[ -\omega_3 (2^* Z_{13}) + \omega_1 (2^* Z_{33}) - Z_{23} \ddot{h}_{w3} \right] \right] + \dots \\
&\lambda_{\omega_3} \left[ \frac{1}{J_3} \left[ -\omega_1 (2^* Z_{23}) + \omega_2 (2^* Z_{13}) - Z_{33} \ddot{h}_{w3} \right] \right] + \dots \\
&\lambda_{h_3} \ddot{h}_{w3} \\
\\
-\frac{\partial H}{\partial h_4} &= \dot{\lambda}_{h_4} = \lambda_{\omega_1} \left[ \frac{1}{J_1} \left[ -\omega_2 (2^* Z_{34}) + \omega_3 (2^* Z_{24}) - Z_{14} \ddot{h}_{w4} \right] \right] + \dots \\
&\lambda_{\omega_2} \left[ \frac{1}{J_2} \left[ -\omega_3 (2^* Z_{14}) + \omega_1 (2^* Z_{34}) - Z_{24} \ddot{h}_{w4} \right] \right] + \dots \\
&\lambda_{\omega_3} \left[ \frac{1}{J_3} \left[ -\omega_1 (2^* Z_{24}) + \omega_2 (2^* Z_{14}) - Z_{34} \ddot{h}_{w4} \right] \right] + \dots \\
&\lambda_{h_4} \ddot{h}_{w4}
\end{aligned} \tag{63}$$

### Minimize the Hamiltonian

Pontryagin's Principle requires that the Hamiltonian be minimized at each instant of time for the unscented reaction wheel maneuver problem's time-varying control space [164]. To meet this requirement, the problem must meet a combination of stationarity and complementarity conditions. The stationarity condition is (9):

$$\frac{\partial \bar{H}}{\partial \mathbf{u}} = \frac{\partial H}{\partial \mathbf{u}} + \left( \frac{\partial \mathbf{h}}{\partial \mathbf{u}} \right)^T \boldsymbol{\mu} = \mathbf{0}$$

The complementarity condition is (64):

$$\mu_{u_i} \left\{ \begin{array}{ll} \leq 0 & \text{if } u_i = -u_{\max} \\ = 0 & \text{if } -u_{\max} < u_i < u_{\max} \\ \geq 0 & \text{if } u_i = u_{\max} \\ \text{unrestricted} & \text{if } -u_{\max} = u_{\max} \end{array} \right\} \quad (64)$$

The stationarity condition is now applied to the unscented reaction wheel maneuver with arbitrary momentum bias problem such that the partial derivative of  $\bar{H}$  with respect to  $\mathbf{u}$  is set equal to zero (65):

$$\begin{aligned} \frac{\partial \bar{H}}{\partial u_1} &= \lambda_{\omega_1} \left[ \frac{1}{J_1} \right] + \lambda_{\omega_2} \left[ \frac{1}{J_2} \right] + \lambda_{\omega_3} \left[ \frac{1}{J_3} \right] + \lambda_{h_1} + \mu_{u_1} = 0 \\ \frac{\partial \bar{H}}{\partial u_2} &= \lambda_{\omega_1} \left[ \frac{1}{J_1} \right] + \lambda_{\omega_2} \left[ \frac{1}{J_2} \right] + \lambda_{\omega_3} \left[ \frac{1}{J_3} \right] + \lambda_{h_2} + \mu_{u_2} = 0 \\ \frac{\partial \bar{H}}{\partial u_3} &= \lambda_{\omega_1} \left[ \frac{1}{J_1} \right] + \lambda_{\omega_2} \left[ \frac{1}{J_2} \right] + \lambda_{\omega_3} \left[ \frac{1}{J_3} \right] + \lambda_{h_3} + \mu_{u_3} = 0 \\ \frac{\partial \bar{H}}{\partial u_4} &= \lambda_{\omega_1} \left[ \frac{1}{J_1} \right] + \lambda_{\omega_2} \left[ \frac{1}{J_2} \right] + \lambda_{\omega_3} \left[ \frac{1}{J_3} \right] + \lambda_{h_4} + \mu_{u_4} = 0 \end{aligned} \quad (65)$$

Then the complementarity condition is applied, which provides information about the behavior of the path co-vectors. Per the problem definition, the control torque must exist between positive and negative values of maximum torque. As the values of applied torque hit the bounds, this constraint results in  $\mu_u$  being unrestricted.

### Construct the Endpoint Lagrangian

The endpoint Lagrangian equation is constructed to evaluate the endpoint boundary conditions at final time. The transversality conditions, minimized Hamiltonian, the Hamiltonian value condition, and the Hamiltonian evolution equation use the endpoint Lagrangian for this evaluation. The endpoint Lagrangian equation is defined as (15):

$$\bar{E}(\mathbf{v}, \mathbf{x}_f, t_f) := E(\mathbf{x}_f, t_f) + \mathbf{v}^T \mathbf{e}(\mathbf{x}_f, t_f)$$

The equation partially depends on the endpoint function which is defined only for the nominal response as modeled by the first sigma point:

$$\mathbf{e}(\mathbf{x}_f, t_f) = \begin{bmatrix} \mathbf{q}_f \\ \boldsymbol{\omega}_f \\ \mathbf{h}_f \end{bmatrix}$$

The unscented reaction wheel maneuver arbitrary momentum bias endpoint Lagrangian equation is thus (66):

$$\bar{E}(\mathbf{v}, \mathbf{x}, t_f, \mathbf{p}) := \kappa_1 \frac{1}{S_\theta} \sum_{j=1}^3 v_{\theta j}^2(\mathbf{x}(\cdot, \mathbf{p}), \mathbf{u}(\cdot), t_f; \mathbf{p}) + \kappa_2 \sum_{j=1}^3 \omega_{\theta j}^2(\mathbf{x}(\cdot, \mathbf{p}), \mathbf{u}(\cdot), t_f; \mathbf{p}) + \mathbf{v}_q \mathbf{q}_f + \mathbf{v}_\omega \boldsymbol{\omega}_f + \mathbf{v}_h \mathbf{h}_f \quad (66)$$

### Determine the transversality conditions

Transversality conditions are found by taking the partial derivative of the endpoint Lagrangian ( $\bar{E}$ ) with respect to the final positions of the state vectors  $\mathbf{q}$ ,  $\boldsymbol{\omega}$ , and  $\mathbf{h}$ . The transversality conditions are in general not useful for verification and validation as they often provide unknowns in terms of other unknowns, as such they are not included in this analysis.

### Hamiltonian value condition

An endpoint cost is evaluated using the Hamiltonian value condition. The minimized Hamiltonian is called the lower Hamiltonian which is denoted by  $\mathcal{H}$ . The lower Hamiltonian at final time is equivalent to the negative of the partial derivative of the endpoint Lagrangian ( $\bar{E}$ ) taken with respect to final time. Evaluating this partial derivative is known as the Hamiltonian value condition. The unscented reaction wheel maneuver arbitrary momentum bias problem yields the following Hamiltonian value condition (67):

$$\mathcal{H}[\text{@}t_f] := -\frac{\partial \bar{E}}{\partial t_f} = 0 \quad (67)$$

that is standard for time-free problems.

### Hamiltonian evolution equation

Because

$$\frac{d\mathcal{H}}{dt} = \frac{\partial \bar{H}}{\partial t} = 0 \quad (68)$$

the minimized Hamiltonian is a constant in time.

## D. NECESSARY CONDITIONS FOR OPTIMUM MOMENTUM BIAS

The problem formulation for optimum momentum bias changes the formulation of the arbitrary bias problem in two ways related to the momentum requirements: one change is in the dynamics equations, the other is in the momentum bias specification. For the arbitrary problem, the derivative of reaction wheel momentum is equal to the candidate control solution and because both initial and final values of momentum bias are specified, the resulting momentum bias path is the same each time the control solution is integrated. For the optimum problem, a range of momentum bias is allowed which can influence the solution. In this way, the momentum bias becomes another variable to be optimized. The

optimal control problem definition for an unscented reaction wheel maneuver with optimum momentum bias is shown as (69) [156-157]:

$$\begin{aligned}
\mathbf{x} &:= [(q_1, \omega_1, h_1), (q_2, \omega_2, h_2), (q_3, \omega_3, h_3)] \in \mathbb{R}^{33} \\
\mathbf{u} &\in \mathbb{U} := \{(u_1, u_2, u_3, u_4) \in \mathbb{R}^4\} \\
\mathbf{h} &:= h_i^L \leq h_i(t) \leq h_i^U \\
\left( ZF_{opt} \right) & \left\{ \begin{array}{ll} \text{Minimize} & J[\mathbf{x}_1(\cdot; \mathbf{p}), \dots, \mathbf{x}_n(\cdot; \mathbf{p}), \mathbf{u}(\cdot; t_f; \mathbf{p})] \approx \sum_{i=1}^n w_i \left( \kappa_1 \frac{1}{s_e} \sum_{j=1}^3 v_{e,j}^2(\mathbf{x}(\cdot; \mathbf{p}), \mathbf{u}(\cdot; t_f; \mathbf{p}_i)) + \kappa_2 \frac{1}{s_e} \sum_{j=1}^3 \omega_{e,j}^2(\mathbf{x}(\cdot; \mathbf{p}), \mathbf{u}(\cdot; t_f; \mathbf{p}_i)) \right) \\ \text{Subject to} & \begin{array}{ll} \hat{\mathbf{q}}_{e,1}(t, \mathbf{J}_1) &= \frac{1}{2} \mathbf{Q}(\omega_1) \mathbf{q}_1^{-1} \otimes \mathbf{q}_e \\ \vdots & \vdots \\ \hat{\mathbf{q}}_{e,n}(t, \mathbf{J}_n) &= \frac{1}{2} \mathbf{Q}(\omega_n) \mathbf{q}_n^{-1} \otimes \mathbf{q}_e \\ \hat{\omega}_1(t, \mathbf{J}_1) &= \mathbf{J}_1^{-1} (\omega_1 \times \mathbf{J}_1 \omega_1 - \omega_1 \times \mathbf{Z} \mathbf{h} - \mathbf{Z} \dot{\mathbf{h}}) \\ \vdots & \vdots \\ \hat{\omega}_n(t, \mathbf{J}_n) &= \mathbf{J}_n^{-1} (\omega_n \times \mathbf{J}_n \omega_n - \omega_n \times \mathbf{Z} \mathbf{h} - \mathbf{Z} \dot{\mathbf{h}}) \\ \hat{\mathbf{h}}_1(t) &= \mathbf{u}_1 \\ \vdots & \vdots \\ \hat{\mathbf{h}}_n(t) &= \mathbf{u}_n \\ (\mathbf{q}_i(t_0), \omega_i(t_0), \mathbf{h}_i(t_0)) &= (\mathbf{q}_e, \mathbf{0}_{3 \times 1}, {}^w \mathbf{h}^0) \\ \mathbf{q}_1(t_f) &= [0, 0, 0, 1]^T \\ \omega_i(t_f) &= [\mathbf{0}_{3 \times 1}] \\ |u_k| &\leq u_{\max} \forall k = 1, 2, 3, 4 \\ \mathbf{J}_i &= \text{diag}(\mathbf{J}_{nom} + \sqrt{\mathbf{P}} \chi_i) \forall i = 1, 2, 3 \\ \mathbf{p}_i &\in \text{supp}(\mathbf{p}) \forall i = 1, 2, 3 \end{array} \end{array} \right. \quad (69)
\end{aligned}$$

A set of necessary conditions that a candidate optimal control solution to the unscented reaction wheel maneuver with optimum momentum bias ( $ZF_{opt}$ ) problem must satisfy is found by developing Pontryagin's necessary conditions for optimality [164]. These necessary conditions follow the framework that was developed for the arbitrary bias problem with differences occurring where momentum bias requirements are specified. The necessary conditions are derived as follows:

1. Construct the Hamiltonian
2. Develop the Adjoint equations

3. Minimize the Hamiltonian
4. Construct the Endpoint Lagrangian
5. Determine transversality conditions
6. Evaluate the Hamiltonian value condition
7. Analyze the Hamiltonian evolution equation

### Construct the Hamiltonian

The Hamiltonian formulation for the optimum momentum bias case is the same as the one for the arbitrary case. As in the arbitrary case, derivations shown here are for one sigma point. Derivations for sigma points two and three are not included for the sake of brevity. The  $ZF_{\text{opt}}$  Hamiltonian is (70):

$$\begin{aligned}
H(\lambda, \mathbf{x}, \mathbf{u}) = & \lambda_{q_1} \left[ \frac{1}{2} [\omega_3 q_2 - \omega_2 q_3 + \omega_1 q_4] \right] + \lambda_{q_2} \left[ \frac{1}{2} [-\omega_3 q_1 + \omega_1 q_3 + \omega_2 q_4] \right] + \dots \\
& \lambda_{q_3} \left[ \frac{1}{2} [\omega_2 q_1 - \omega_1 q_2 + \omega_3 q_4] \right] + \lambda_{q_4} \left[ \frac{1}{2} [-\omega_1 q_1 - \omega_2 q_2 - \omega_3 q_3] \right] + \dots \\
& \lambda_{\omega_1} \left[ \frac{1}{J_1} [J_2 \omega_2 \omega_3 - J_3 \omega_2 \omega_3 - \omega_2 h_{B3} + \omega_3 h_{B2} - u_{B1}] \right] + \dots \\
& \lambda_{\omega_2} \left[ \frac{1}{J_2} [J_3 \omega_3 \omega_1 - J_1 \omega_3 \omega_1 - \omega_3 h_{B1} + \omega_1 h_{B3} - u_{B2}] \right] + \dots \\
& \lambda_{\omega_3} \left[ \frac{1}{J_3} [J_1 \omega_1 \omega_2 - J_2 \omega_1 \omega_2 - \omega_1 h_{B2} + \omega_2 h_{B1} - u_{B3}] \right] + \dots \\
& \lambda_{h_1} [u_{W1}] + \lambda_{h_2} [u_{W2}] + \lambda_{h_3} [u_{W3}] + \lambda_{h_4} [u_{W4}]
\end{aligned} \tag{70}$$

The Lagrangian of the Hamiltonian ( $\bar{H}$ ) includes path co-vectors ( $\mu$ ) added to the original Hamiltonian for each control  $u$  and each momentum  $h$ . The Lagrangian of the

Hamiltonian for the first sigma point of the unscented reaction wheel maneuver optimum momentum bias problem is (71):

$$\begin{aligned}
\bar{H}(\boldsymbol{\mu}, \boldsymbol{\lambda}, \mathbf{x}, \mathbf{u}) = & \lambda_{q_1} \left[ \frac{1}{2} [\omega_3 q_2 - \omega_2 q_3 + \omega_1 q_4] \right] + \lambda_{q_2} \left[ \frac{1}{2} [-\omega_3 q_1 + \omega_1 q_3 + \omega_2 q_4] \right] + \dots \\
& \lambda_{q_3} \left[ \frac{1}{2} [\omega_2 q_1 - \omega_1 q_2 + \omega_3 q_4] \right] + \lambda_{q_4} \left[ \frac{1}{2} [-\omega_1 q_1 - \omega_2 q_2 - \omega_3 q_3] \right] + \dots \\
& \lambda_{\omega_1} \left[ \frac{1}{J_1} [J_2 \omega_2 \omega_3 - J_3 \omega_2 \omega_3 - \omega_2 h_{B3} + \omega_3 h_{B2} - u_{B1}] \right] + \dots \\
& \lambda_{\omega_2} \left[ \frac{1}{J_2} [J_3 \omega_3 \omega_1 - J_1 \omega_3 \omega_1 - \omega_3 h_{B1} + \omega_1 h_{B3} - u_{B2}] \right] + \dots \\
& \lambda_{\omega_3} \left[ \frac{1}{J_3} [J_1 \omega_1 \omega_2 - J_2 \omega_1 \omega_2 - \omega_1 h_{B2} + \omega_2 h_{B1} - u_{B3}] \right] + \dots \\
& \lambda_{h_1} [u_{w1}] + \lambda_{h_2} [u_{w2}] + \lambda_{h_3} [u_{w3}] + \lambda_{h_4} [u_{w4}] + \dots \\
& \mu_{u_1} [u_{w1}] + \mu_{u_2} [u_{w2}] + \mu_{u_3} [u_{w3}] + \mu_{u_4} [u_{w4}] + \dots \\
& \mu_{h_1} [h_{w1}] + \mu_{h_2} [h_{w2}] + \mu_{h_3} [h_{w3}] + \mu_{h_4} [h_{w4}]
\end{aligned} \tag{71}$$

### Develop the adjoint equations

The adjoint equations are found by taking the partial derivative of the Hamiltonian with respect to  $\mathbf{q}$ ,  $\boldsymbol{\omega}$  and  $\mathbf{h}$ . The adjoint equations for the optimum momentum bias case are nearly identical as found for the arbitrary bias case only with the addition of a  $\mu$  term associated with the wheel momentum. Please see the arbitrary bias case in the previous section for details.

### Minimize the Hamiltonian

To meet the requirement that the Hamiltonian be minimized at each instant of time [164], the problem must meet a combination of stationarity and complementarity conditions. The stationarity condition is (9):



$$\frac{\partial \bar{H}}{\partial \mathbf{u}} = \frac{\partial H}{\partial \mathbf{u}} + \left( \frac{\partial \mathbf{h}}{\partial \mathbf{u}} \right)^T \boldsymbol{\mu} = 0$$

The complementarity conditions for the control path and momentum path constraints for the first sigma point are (72) and (73):

$$\mu_{u_i} \left\{ \begin{array}{lll} \leq 0 & \text{if} & u_i = -u_{\max} \\ = 0 & \text{if} & -u_{\max} < u_i < u_{\max} \\ \geq 0 & \text{if} & u_i = u_{\max} \\ \text{unrestricted} & \text{if} & -u_{\max} = u_{\max} \end{array} \right\} \quad (72)$$

$$\mu_{h_i} \left\{ \begin{array}{lll} \leq 0 & \text{if} & h_i = -h_{\max} \\ = 0 & \text{if} & -h_{\max} < h_i < h_{\max} \\ \geq 0 & \text{if} & h_i = h_{\max} \\ \text{unrestricted} & \text{if} & -h_{\max} = h_{\max} \end{array} \right\} \quad (73)$$

The stationarity condition is now applied to the unscented reaction wheel maneuver with optimum momentum bias problem for the first sigma point such that the partial derivative of  $\bar{H}$  with respect to  $\mathbf{u}$  is set equal to zero (74):

$$\frac{\partial \bar{H}}{\partial u_1} = \lambda_{\omega_1} \left[ \frac{1}{J_1} \right] + \lambda_{\omega_2} \left[ \frac{1}{J_2} \right] + \lambda_{\omega_3} \left[ \frac{1}{J_3} \right] + \lambda_{h_1} + \mu_{u_1} = 0$$

$$\frac{\partial \bar{H}}{\partial u_2} = \lambda_{\omega_1} \left[ \frac{1}{J_1} \right] + \lambda_{\omega_2} \left[ \frac{1}{J_2} \right] + \lambda_{\omega_3} \left[ \frac{1}{J_3} \right] + \lambda_{h_2} + \mu_{u_2} = 0$$

$$\frac{\partial \bar{H}}{\partial u_3} = \lambda_{\omega_1} \left[ \frac{1}{J_1} \right] + \lambda_{\omega_2} \left[ \frac{1}{J_2} \right] + \lambda_{\omega_3} \left[ \frac{1}{J_3} \right] + \lambda_{h_3} + \mu_{u_3} = 0$$

$$\frac{\partial \bar{H}}{\partial u_4} = \lambda_{\omega_1} \left[ \frac{1}{J_1} \right] + \lambda_{\omega_2} \left[ \frac{1}{J_2} \right] + \lambda_{\omega_3} \left[ \frac{1}{J_3} \right] + \lambda_{h_4} + \mu_{u_4} = 0$$

(74)

Then the complementarity conditions are applied. Per the problem definition, the control torque must exist between positive and negative values of maximum torque. As the values of applied torque hit the bounds, this constraint results in  $\mu_u$  being unrestricted. The value of momentum is constrained to a range of values, but if the optimum bias value is not on the boundaries, then  $\mu_h$  is zero and the term drops.

### Construct the Endpoint Lagrangian

The endpoint Lagrangian equation is constructed to evaluate the endpoint boundary conditions at final time. The transversality conditions, minimized Hamiltonian, the Hamiltonian value condition, and the Hamiltonian evolution equation use the endpoint Lagrangian for this evaluation. The endpoint Lagrangian equation is defined as (14):

$$\bar{E}(\mathbf{v}, \mathbf{x}_f, t_f) := E(\mathbf{x}_f, t_f) + \mathbf{v}^T \mathbf{e}(\mathbf{x}_f, t_f)$$

The equation partially depends on the endpoint function. It should be noted that this optimum bias definition is different from the arbitrary bias problem in that there is now no specific value for the momentum bias at final time since it can be a within a range of values according to the path constraint. Therefore, there is no endpoint requirement for the value of the optimum momentum bias. The endpoint function for the optimum bias problem for the first sigma point (nominal response) is defined as the following:

$$\mathbf{e}(\mathbf{x}_f, t_f) = \begin{bmatrix} \mathbf{q}_f \\ \boldsymbol{\omega}_f \end{bmatrix}$$

The unscented reaction wheel maneuver optimum momentum bias endpoint Lagrangian equation for the first sigma point is thus (75):

$$\bar{E}(\mathbf{v}, \mathbf{x}, t_f, \mathbf{p}) := \kappa_1 \frac{1}{S_e} \sum_{j=1}^3 v_{e,j}^2(\mathbf{x}(\cdot, \mathbf{p}), \mathbf{u}(\cdot), t_f; \mathbf{p}) + \kappa_2 \sum_{j=1}^3 \omega_{e,j}^2(\mathbf{x}(\cdot, \mathbf{p}), \mathbf{u}(\cdot), t_f; \mathbf{p}) + \mathbf{v}_q \mathbf{q}_f + \mathbf{v}_\omega \boldsymbol{\omega}_f$$

(75)

### **Determine the transversality conditions**

Transversality conditions for the optimum momentum bias case are found by taking the partial derivative of the endpoint Lagrangian ( $\bar{E}$ ) with respect to the final positions of the state vectors  $\mathbf{q}$  and  $\mathbf{\omega}$ . Results for the transversality conditions associated with  $\mathbf{q}$  and  $\mathbf{\omega}$  are the same for the optimum case as for the arbitrary momentum bias case. For the optimal case, there are no requirements imposed on  $\mathbf{h}$  at final time, so there is no transversality condition associated with it, unlike with the arbitrary case. This means that the corresponding co-state values for  $\mathbf{h}$  will be zero at final time.

### **Hamiltonian value condition and Hamiltonian evolution equation**

The analysis for this problem produces the same results as before.

## **E. CHAPTER SUMMARY**

The purpose of this chapter was to formulate an unscented reaction wheel maneuver cost functional and use it to develop full problem descriptions with necessary conditions for both a version with arbitrary momentum bias and a version with optimum momentum bias. A cost functional was developed using mean squared error combined with uncertainty. This cost functional was then expanded to include terms of interest in the unscented reaction wheel maneuver, spacecraft position and rate. Using these variables with a mean squared error approach minimizes the variance of terminal pointing error which is the desired outcome. Three sigma points were defined for use with the arbitrary and optimum momentum bias problems. The unscented reaction wheel maneuver problem definition incorporates this information in the weighted sum term. A full problem definition was provided for the arbitrary momentum bias that included dynamics, initial and final time conditions for all state vectors,  $\mathbf{q}$ ,  $\mathbf{\omega}$ , and  $\mathbf{h}$ . For the full definition of the optimum momentum bias problem, additional dynamics terms were included for  $\mathbf{h}$  and a path constraint was added thereby allowing  $\mathbf{h}$  to become an optimizable variable. Necessary conditions were developed for both the arbitrary and optimum momentum bias problems.

The adjoint equations were nearly identical for both problems with extra terms for momentum in the optimum bias case. The Lagrangian of the Hamiltonian included additional terms for the optimum momentum bias path constraint,  $h$ . The endpoint Lagrangian differed in that the arbitrary problem included endpoint functions for all state vectors,  $\mathbf{q}$ ,  $\boldsymbol{\omega}$ , and  $\mathbf{h}$ , whereas the optimum problem included only  $\mathbf{q}$  and  $\boldsymbol{\omega}$ . This difference in the  $\mathbf{h}$  term appears in the transversality conditions, which are based on the endpoint Lagrangian, where the arbitrary case includes  $\mathbf{h}$ , and the optimum case does not. Results for the Hamiltonian value condition and Hamiltonian evolution equation were the same for both problems since they are both time-free problems. These necessary conditions provide a roadmap to evaluate the results of the unscented reaction wheel maneuver optimal control problems in the following chapter.

THIS PAGE INTENTIONALLY LEFT BLANK

## V. UNSCENTED REACTION WHEEL ATTITUDE MANEUVERS

This chapter of the dissertation solves an unscented reaction wheel maneuver optimal control problem with increasing levels of uncertainty. The arbitrary and optimum momentum bias problems from the previous chapter are solved with both single axis and three axes of uncertainty and results are provided. These results are compared against the necessary conditions that were developed in previous sections. It is shown that unscented guidance is a viable method for reduction of sensitivity to problem uncertainty thus allowing a spacecraft to perform a large angle unscented reaction wheel maneuver in the absence of feedback control. The results of this section were first published in [156-157].

### A. ARBITRARY MOMENTUM BIAS SOLUTIONS

#### 1. Single-Axis Inertia Uncertainty

A fundamental tenet of feedback systems is their ability to reduce the sensitivity of the system to variations in the parameters [151]. This perspective implies that open-loop sensitivity cannot be mitigated without feedback. It is reasonable, then, to question how a satellite might be accurately maneuvered in the presence of uncertainty in the mass properties, but in the absence of feedback. The mechanism for reducing open-loop sensitivity in reaction wheel attitude maneuvering relies on leveraging the non-linear coupling inherent to the rotational dynamics of the system. To help illustrate this cross-coupling, re-write Euler's equations in the body fixed frame. Note that in this frame,  $h$  has been transformed from the reaction wheel frame to the body fixed frame by applying the  $\mathbf{Z}$  matrix present in earlier problem formulations:

$$\dot{\omega} = \mathbf{J}^{-1} \left( -\omega \times (\mathbf{J}\omega + h) - u \right) \quad (76)$$

This expression (76) can be expanded for  $x$ ,  $y$ , and  $z$  axes with the following set of equations:

$$\begin{aligned}
\dot{\omega}_1 &= \frac{J_2 - J_3}{J_1} \omega_2 \omega_3 + \frac{\omega_3 h_{2_0} + \omega_2 h_{3_0}}{J_1} - \frac{u_1 + \omega_2 \int u_3 - \omega_3 \int u_2}{J_1} \\
\dot{\omega}_2 &= \frac{J_3 - J_1}{J_2} \omega_3 \omega_1 + \frac{\omega_1 h_{3_0} + \omega_3 h_{1_0}}{J_2} - \frac{u_2 + \omega_3 \int u_1 - \omega_1 \int u_3}{J_2} \\
\dot{\omega}_3 &= \underbrace{\frac{J_1 - J_2}{J_3} \omega_1 \omega_2 + \frac{\omega_2 h_{1_0} + \omega_1 h_{2_0}}{J_3}}_{\text{feedback}} - \underbrace{\frac{u_3 + \omega_1 \int u_2 - \omega_2 \int u_1}{J_3}}_{\text{feed-forward}}
\end{aligned} \tag{77}$$

where  $\mathbf{h}_0$  represents the initial momentum state of a reaction wheel array in the body frame. It is clear (and not surprising) from the equation expansion that rotational motion of the satellite is cross-coupled amongst the axes (77). This cross-coupling provides natural non-linear feedback paths that could be used to reduce the effects of inertia tensor uncertainties. In this sense, naturally occurring feedback as opposed to artificial feedback is relied upon to null-out the error. Thus, the open-loop guidance problem to be solved is one of finding the feed-forward reaction wheel command trajectories,  $\mathbf{u}(\cdot)$ , that achieve the specified terminal conditions as closely as possible in the presence of uncertainty via the suitable exploitation of the cross-coupling feedbacks.

Up to this point, no assumptions have been made on the initial momentum state of the satellite. Consider now the situation for the case of a zero-net bias system which is quite common for spacecraft control systems. In this case, we have  $\mathbf{J}\boldsymbol{\omega} + \mathbf{h} = \mathbf{0}$  during the timeframe of a maneuver due to the conservation of angular momentum. Thus, in a zero-net bias system, the natural non-linear feedback paths are all open meaning that their contribution does not enter the closed-loop system or is actively cancelled by the system. Consequently, in the absence of any appreciable momentum bias, the open-loop sensitivity cannot be managed. It will therefore not be possible to improve upon the open-loop performance of the baseline slew. A non-zero momentum bias is a necessary condition for an unscented reaction wheel maneuver.

Returning to the three-axis expansion of Euler's equation (77), it is evident in the case of a non-zero momentum bias that the naturally occurring feedback gains are fixed, with the values determined by the mass properties of the satellite and the magnitude of the momentum bias in the system. Momentum bias is altered by momentum loading or unloading. This relationship provides tuning knobs that can be used to affect the open-loop response. Finding the optimum tuning of these gains for a given unscented reaction wheel maneuver is part of the subject of this chapter.

A Monte Carlo simulation of the unscented reaction wheel maneuver solution for an arbitrary momentum bias,  ${}^B\mathbf{H}(t_0) = [-3.35, 6.91, 0.46]^T$ , is shown in Figures 34–36. The control history was obtained using DIDO, the MATLAB toolbox for solving optimal control problems [167]. The state trajectories were generated by 4<sup>th</sup>-order Runge-Kutta propagation (ode45 in MATLAB) using interpolated values of the DIDO controls and a 0.2 sec time step. This is the same type of interpolation and verification process described in [164] and used in practical flight implementations of optimal control [228].

Referring to Figures 34–36, it is seen that the unscented reaction wheel maneuver can control the angle error nearly as well as quaternion error feedback as seen in “Example Closed-Loop Slew,” even though the control is implemented as open-loop. The uncertainty associated with the inertia tensor is mitigated in the open-loop by following the nominal angular rate profile shown as the solid lines in Figure 35. Comparing Figure 35 with the open-loop angular rates (Figure 27), it is apparent that the unscented reaction wheel maneuver utilizes motion about all three body axes to mitigate the effects of the uncertainty. Figure 35 also shows the uncertainty tubes as shaded areas around the nominal curves, although the uncertainty tubes for this case tightly follow the nominal curves which makes them difficult to see. The small width of the uncertainty tubes show that the unscented reaction wheel maneuver can find a profile that is robust against the uncertainty. The angular momentum of the reaction wheels expressed in the body frame is shown in Figure 36. Comparing Figure 36 with Figure 28 it is seen that the momentum profile for unscented reaction wheel maneuver is quite different than its open-loop counterpart as the momentum adjusts with the changes in the angular rate to minimize open-loop error. Nonetheless, application of the momentum profile obtained from the unscented reaction



wheel maneuver solution enables the satellite to be quite accurately reoriented in the open-loop.

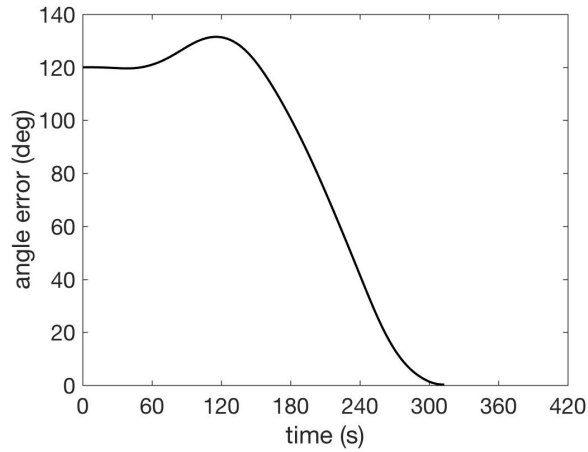


Figure 34. Unscented Reaction Wheel Maneuver Single-Axis Uncertainty Angle Error with Arbitrary Momentum Bias

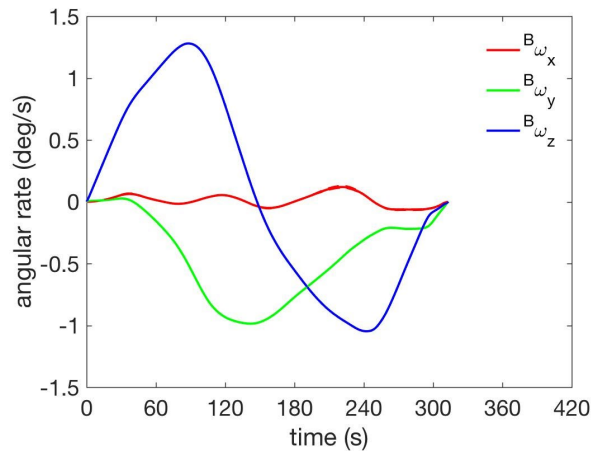


Figure 35. Unscented Reaction Wheel Maneuver Single-Axis Uncertainty Body-Frame Angular Rate with Arbitrary Momentum Bias

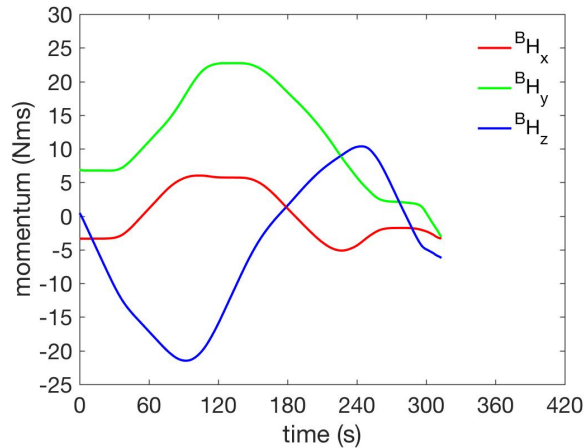


Figure 36. Unscented Reaction Wheel Maneuver Single-Axis Uncertainty Body-Frame Reaction Wheel Momentum with Arbitrary Momentum Bias

Statistics are evaluated for the unscented reaction wheel maneuver with arbitrary momentum bias. The terminal pointing errors are measured at  $t = 313$  seconds and are shown in Figure 37 superimposed on the open-loop results from Figure 29 and includes the  $3\sigma$  error ellipse. The average angle error is 0.21 degrees and average rate error is 0.0011 deg/sec. As seen in Figure 37 (inset), the unscented reaction wheel maneuver solution reduces the terminal error by over an order of magnitude in comparison with the baseline open-loop attitude control.

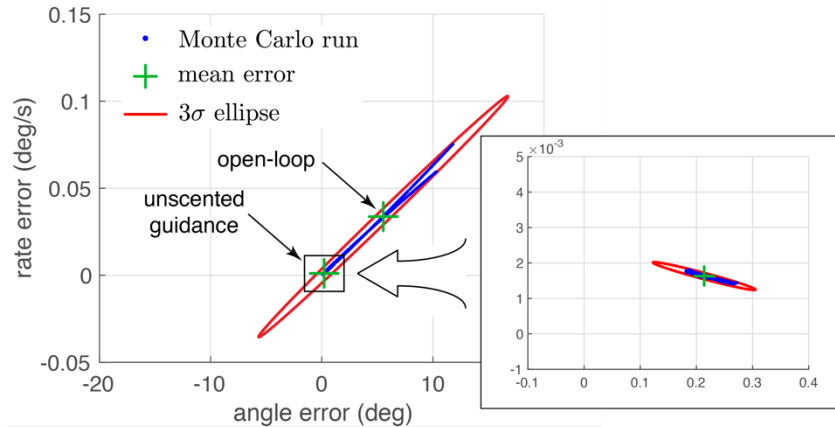


Figure 37. Monte Carlo Simulation Results of Unscented Reaction Wheel Maneuver Arbitrary Momentum Bias with Single-Axis Uncertainty: Terminal Pointing Errors

### Review of Necessary Conditions

For these unscented guidance optimal control problems with uncertainty and arbitrary momentum, Pontryagin's necessary conditions for solution accuracy are reviewed. Details of the necessary conditions can be found in the previous chapter. The Lagrangian of the Hamiltonian captured the control,  $u$ , path constraint. The complementarity condition for the single-axis and three-axis uncertainty problems indicated that  $\mu$  was unrestricted in its value due to the control path constraint. The Hamiltonian value condition and Hamiltonian evolution equation stipulated that the value of the lower Hamiltonian be zero and that the value be a constant (67) and (68). This constant zero value is consistent with the literature regarding time-free problems.

Figure 38 shows the four candidate control torque solution profiles,  $u_1$ ,  $u_2$ ,  $u_3$ , and  $u_4$ , one for each of the four reaction wheels, for the unscented reaction wheel maneuver arbitrary momentum bias single-axis uncertainty solution. These control paths show the wheel torques switching between positive maximum and negative maximum wheel limits which were expected due to the results from the complementarity condition indicating that  $\mu$  was unrestricted. Evaluation of the Hamiltonian value condition stipulated that the lower Hamiltonian would be a constant close to zero which is consistent with a time-free problem.

As seen in Figure 39, the lower Hamiltonian maintains a value close to zero for the full time of the maneuver.

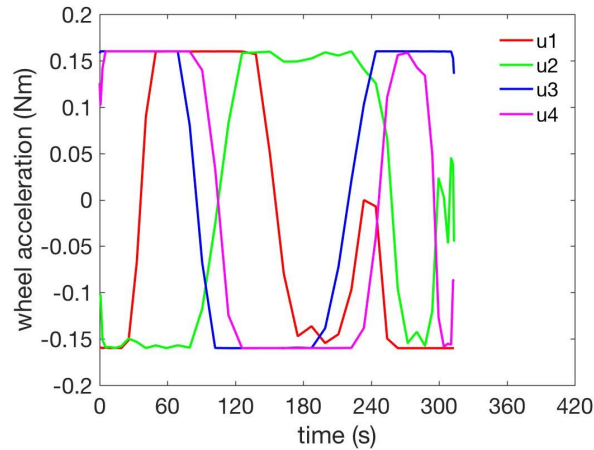


Figure 38. Solution of the Unscented Reaction Wheel Maneuver Arbitrary Momentum Bias Problem with Single-Axis Uncertainty: Optimal Control Versus Time

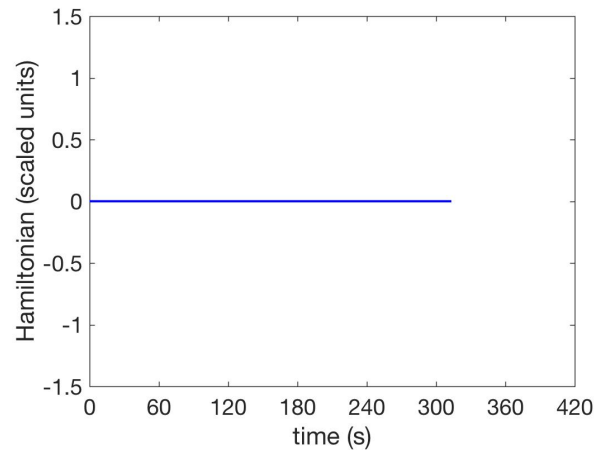


Figure 39. Solution of the Unscented Reaction Wheel Maneuver Arbitrary Momentum Bias Problem with Single-Axis Uncertainty: Optimal Hamiltonian Versus Time

The functions seen in Figures 40–42 for the co-state trajectories show that the quaternion, rate and momentum co-states are close to, but not exactly zero.

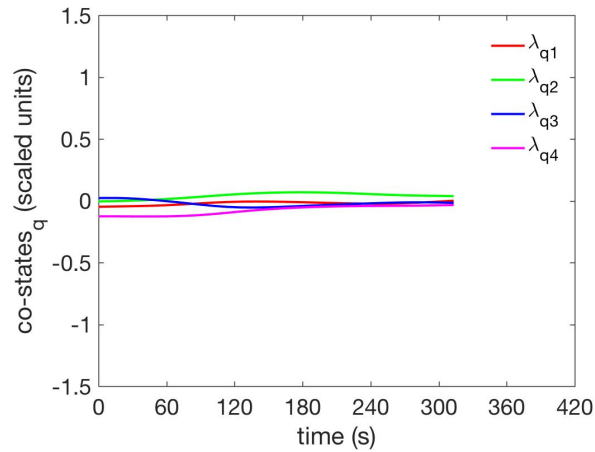


Figure 40. Solution of the Unscented Reaction Wheel Maneuver Arbitrary Momentum Bias Problem with Single-Axis Uncertainty: Co-States  $\lambda_q$  Versus Time

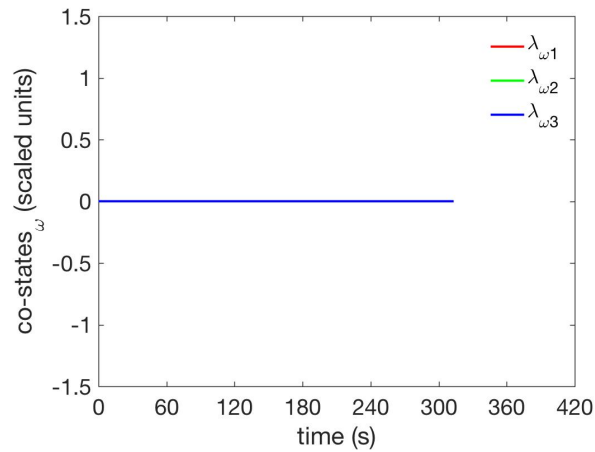


Figure 41. Solution of the Unscented Reaction Wheel Maneuver Arbitrary Momentum Bias Problem with Single-Axis Uncertainty: Co-States  $\lambda_\omega$  Versus Time

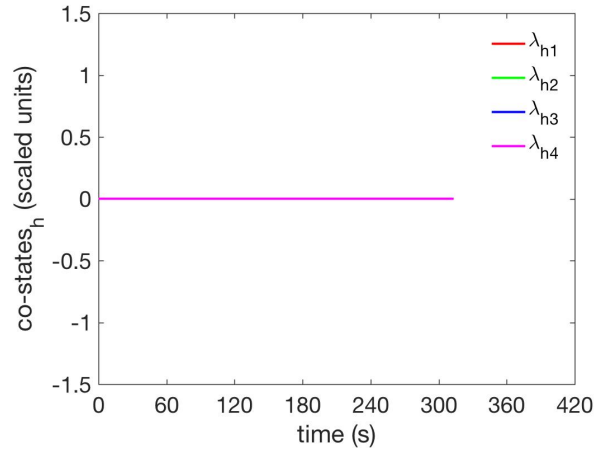


Figure 42. Solution of the Unscented Reaction Wheel Maneuver  
Arbitrary Momentum Bias Problem with Single-Axis  
Uncertainty: Co-States  $\lambda_h$  Versus Time

Path constraints were imposed on this problem as limits on the control,  $u$ . Initial and final values of momentum were specified as  ${}^b\mathbf{H}(t_0) = [-3.35, 6.91, 0.46]^T$  Nms. Figure 43 shows that the conservation of angular momentum holds for the values of the paths as they match the specified initial and final momentum values. Due to the predicted Hamiltonian, co-states and path constraint results meeting expected results, this candidate optimal control solution is considered an optimal solution to the  $ZF_{arb}$  problem.

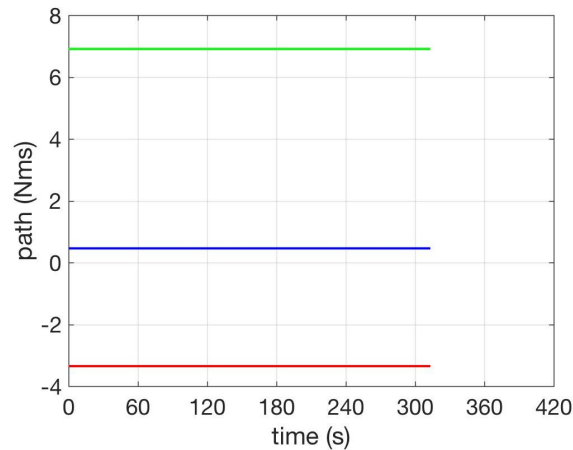


Figure 43. Solution of the Unscented Reaction Wheel Maneuver Arbitrary Momentum Bias Problem with Single-Axis Uncertainty: Conservation of Angular Momentum

## 2. Three-Axis Inertia Uncertainty

The previous unscented reaction wheel maneuver solution accounts for uncertainty in only one axis. This uncertainty exists solely in the  $x$ -axis. Although it is apparent that the parametric uncertainty is managed in the open-loop by the unscented reaction wheel algorithm, it remains to be seen what effect most realistic uncertainty in all three axes has on the solution. The unscented reaction wheel maneuver using arbitrary momentum bias is solved for three-axis uncertainty to understand these effects. The optimum momentum bias cases follow. A Monte Carlo simulation of the three-axis-uncertainty arbitrary momentum bias is shown in Figures 44–47.

The three-axis uncertainty solutions are run using the same time frame as their respective single-axis solutions, that is 313 seconds. Referring to Figures 44–47, it is seen that uncertainty in all three axes produces remarkably different response trajectories for position, angular rate and momentum as compared to the single-axis-uncertainty unscented reaction wheel solutions (see Figures 34–36), as the shape and mass of the satellite are taken into full account. The Monte Carlo error results show this increase in fidelity comes with an increase in error, as expected.

The terminal pointing errors for the three-axis uncertainty with arbitrary momentum bias solution is shown in Figure 47 along with the associated  $3\sigma$  error ellipse. Figure 47 shows very clearly that the pointing errors are less than half the amount that was seen in the open-loop but ten times greater than the errors that were seen with single-axis uncertainty solutions.

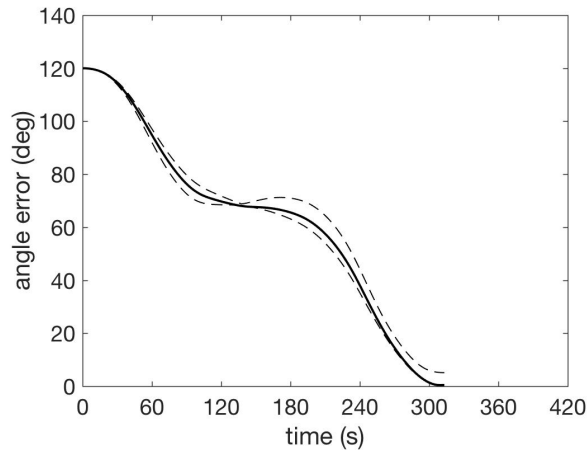


Figure 44. Unscented Reaction Wheel Maneuver Three-Axis Uncertainty Angle Error with Arbitrary Momentum Bias

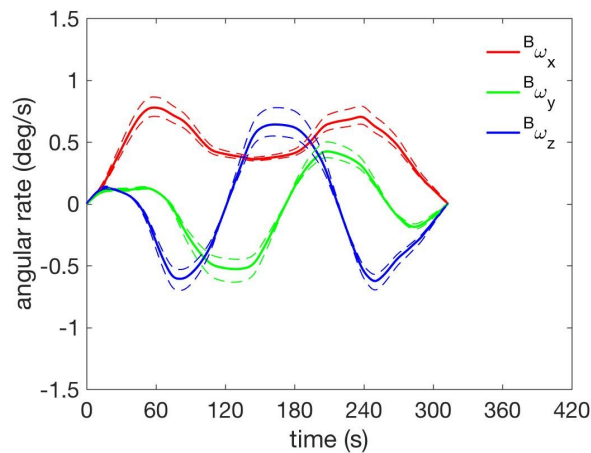


Figure 45. Unscented Reaction Wheel Maneuver Three-Axis Uncertainty Body-Frame Angular Rate with Arbitrary Momentum Bias



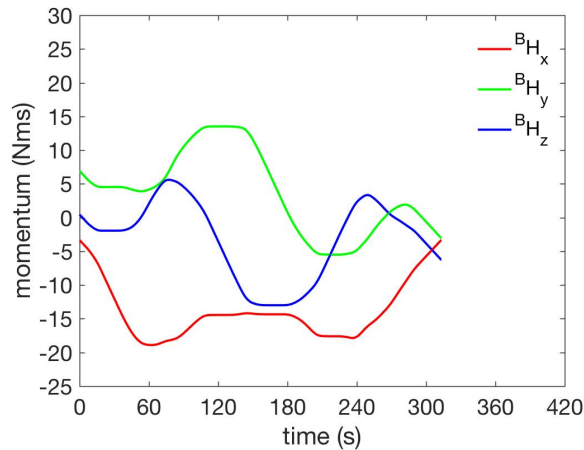


Figure 46. Unscented Reaction Wheel Maneuver Three-Axis Uncertainty Body-Frame Reaction Wheel Momentum with Arbitrary Momentum Bias

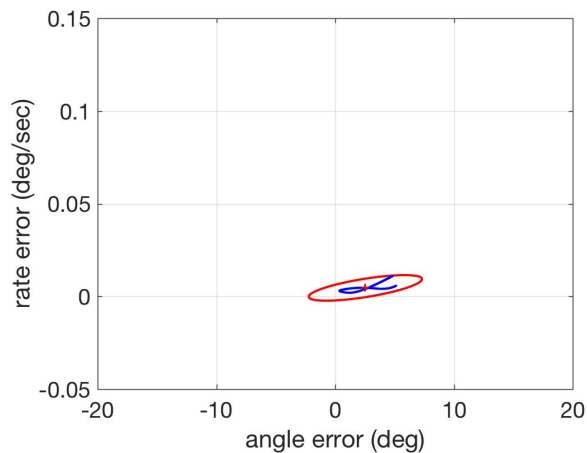


Figure 47. Monte Carlo Simulation Results of Unscented Reaction Wheel Maneuver Arbitrary Momentum Bias with Three-Axis Uncertainty: Terminal Pointing Errors

For the unscented reaction wheel maneuver arbitrary momentum three-axis uncertainty case, Figure 48 shows the four candidate control torque solution profiles,  $u_1$ ,  $u_2$ ,  $u_3$ , and  $u_4$ , one for each of the four reaction wheels. These profiles are similar to the single-axis uncertainty case in that they exhibit bang-bang response but are dissimilar in that the control torques switch more often due to the additional error present in the three-axis case. The three-axis uncertainty case has the same Hamiltonian value condition

stipulation as the single-axis case, that the lower Hamiltonian would be a constant close to zero which is consistent with a time-free problem. As seen in Figure 49, the lower Hamiltonian maintains a value close to zero for the full time of the maneuver, however there is some variability in the response which indicates this solution could be improved.

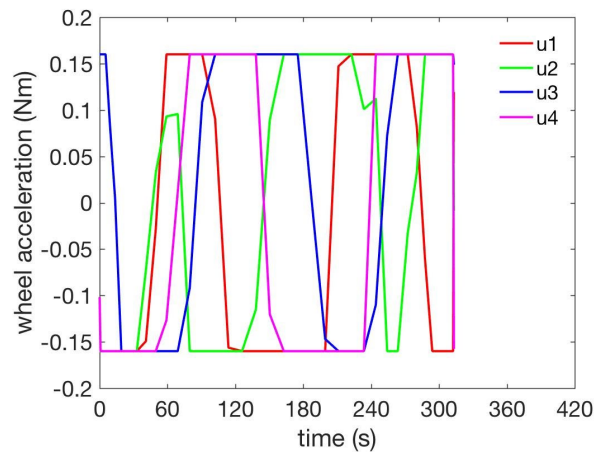


Figure 48. Solution of the Unscented Reaction Wheel Maneuver Arbitrary Momentum Bias Problem with Three-Axis Uncertainty: Optimal Control Versus Time

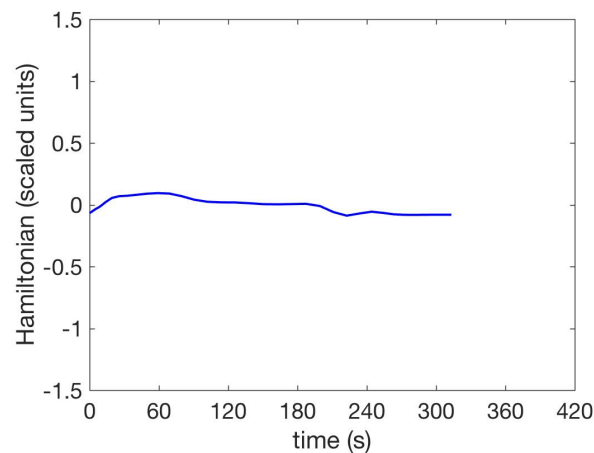


Figure 49. Solution of the Unscented Reaction Wheel Maneuver Arbitrary Momentum Bias Problem with Three-Axis Uncertainty: Optimal Hamiltonian Versus Time

Just the same as in the single-axis arbitrary momentum bias problem, the three-axis problem had path constraints imposed on it as limits on the control,  $u$ . Initial and final values of momentum were specified as  ${}^B\mathbf{H}(t_0) = [-3.35, 6.91, 0.46]^T$  Nms. Figure 50 shows that the conservation of angular momentum holds for the paths as the values of the paths match the specified initial and final momentum values. The necessary conditions analysis meets expected results; thus, the candidate optimal control solution is considered an optimal solution to the  $ZF_{arb}$  problem.

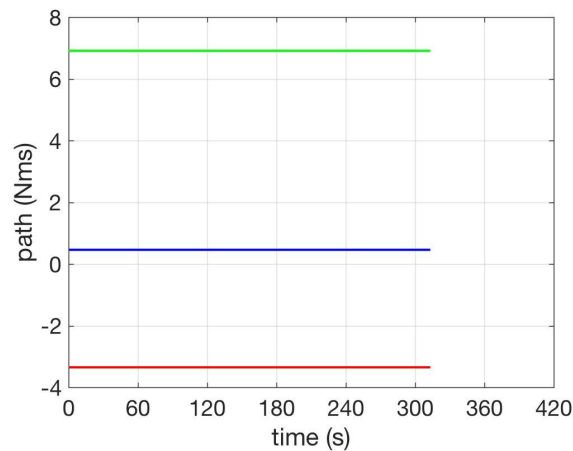


Figure 50. Solution of the Unscented Reaction Wheel Maneuver Arbitrary Momentum Bias Problem with Three-Axis Uncertainty: Conservation of Angular Momentum

## B. OPTIMUM MOMENTUM BIAS SOLUTIONS

### 1. Single-Axis Inertia Uncertainty

It is apparent from the unscented reaction wheel maneuver with arbitrary momentum bias results that unscented guidance allows the effects of parametric uncertainty to be managed in the open-loop. These unscented reaction wheel maneuver with arbitrary momentum bias problems are changed in their momentum related conditions and re-solved to find the optimum momentum bias with the goal of further reducing the terminal error. This was accomplished by modeling the bias momentum as an uncertain event that changes the necessary conditions and is optimized alongside the unscented

maneuver profile. The optimum bias for the large-angle maneuver was determined to be  ${}^B\mathbf{H}(t_0) = [-1.53, 3.92, 0.73]^T$ . A Monte Carlo simulation of the optimum bias solution is shown in Figures 51–55. The results of this section were first published in [157].

Referring to Figures 51–53, it is seen that optimum bias solution is qualitatively similar to the solutions for arbitrary momentum bias. Note that the angle error profile has a small error tube width. The rate error tube widths are also small and adhere tightly to the shape of the rate profile with most of the error concentrated in the peaks and valleys of the x-axis. The subtle changes in the momentum profile do, however, improve the overall performance of the open-loop system albeit at a cost of an additional 94 seconds to complete the maneuver. This aspect is best seen in the statistics associated with the terminal pointing error. The terminal pointing errors for both the arbitrary and optimum bias solutions are shown in Figures 54 and 55 along with their associated  $3\sigma$  error ellipses. Figures 54 and 55 show very clearly that the optimum bias solution does a superior job of reducing the terminal error. The optimum bias solution reduces the terminal error by an order of magnitude compared with an unscented reaction wheel maneuver solution for an arbitrary momentum bias.

The optimum bias solution drives the average terminal pointing error for the large 120 deg slew to less than 0.1 deg and 0.002 deg/sec. This is similar to the performance of a closed-loop attitude control system prior to settling. Thus, the error tolerances achieved using the optimum bias solution should be sufficiently small to enable handover to a science-mode pointing controller, which is used to enable data collection operations.

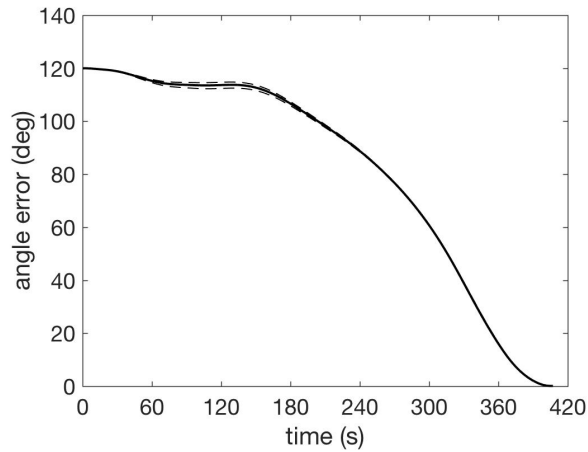


Figure 51. Unscented Reaction Wheel Maneuver Single-Axis Uncertainty Angle Error with Optimum Momentum Bias

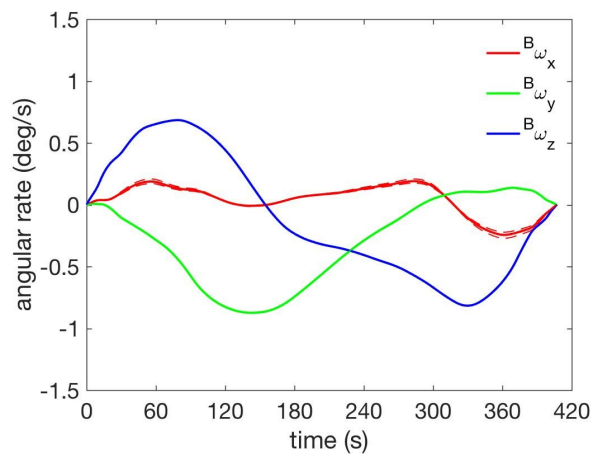


Figure 52. Unscented Reaction Wheel Maneuver Single-Axis Uncertainty Body-Frame Angular Rate with Optimum Momentum Bias

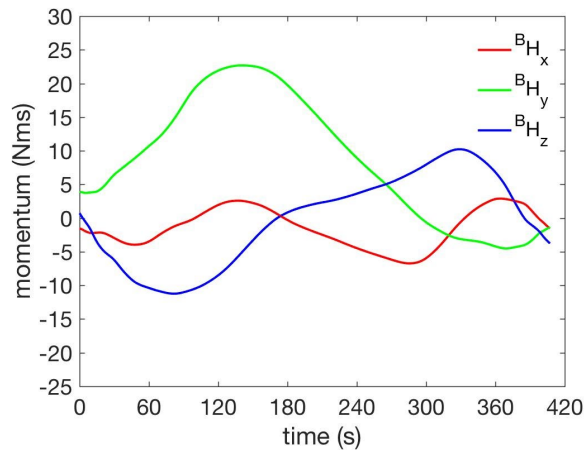


Figure 53. Unscented Reaction Wheel Maneuver Single-Axis Uncertainty Body-Frame Reaction Wheel Momentum with Optimum Momentum Bias

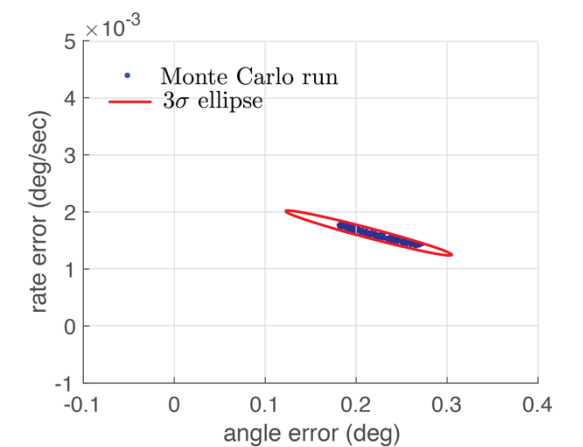


Figure 54. Monte Carlo Simulation Results of Unscented Reaction Wheel Maneuver Arbitrary Momentum Bias with Single-Axis Uncertainty: Terminal Pointing Errors

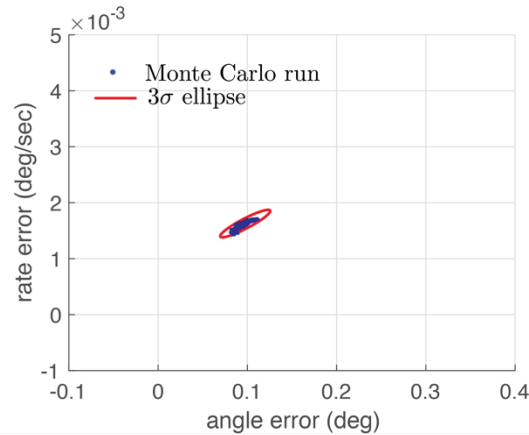


Figure 55. Monte Carlo Simulation Results of Unscented Reaction Wheel Maneuver Optimum Momentum Bias with Single-Axis Uncertainty: Terminal Pointing Errors

### Review of Necessary Conditions

Pontryagin's necessary conditions for solution accuracy are reviewed for the unscented guidance problems with optimum momentum. Details of the necessary conditions can be found in previous chapters of this dissertation. The Lagrangian of the Hamiltonian captured the path constraints,  $u$ , and  $h$ . The complementarity condition for the optimum momentum bias problems indicated that  $\mu$  was zero in its value due to the momentum path constraint. Co-state values of  $h$  were zero for both the single-axis and the three-axis cases. Transversality conditions were evaluated, but no new information was provided as equations generated more unknowns in terms of existing unknowns. The Hamiltonian value condition and Hamiltonian evolution equation stipulated that the value of the lower Hamiltonian be zero and that the value be a constant. This constant zero value is consistent with the literature regarding time-free problems.

Figure 56 shows the four candidate control torque solution profiles,  $u_1$ ,  $u_2$ ,  $u_3$ , and  $u_4$ , one for each of the four reaction wheels, for the unscented reaction wheel maneuver optimum momentum bias single-axis uncertainty solution. Compared to the arbitrary momentum bias solutions, these profiles contain more variability and less bang-bang behavior due to the influence of the optimum momentum adjustments. Evaluation of the Hamiltonian value condition stipulated that the lower Hamiltonian would be a constant

close to zero which is consistent with a time-free problem. As seen in Figure 57, the lower Hamiltonian maintains a value close to zero for the full time of the maneuver.

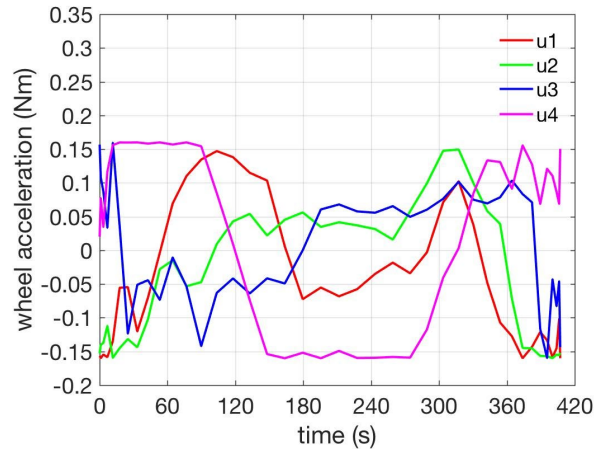


Figure 56. Solution of the Unscented Reaction Wheel Maneuver Optimum Momentum Bias Problem with Single-Axis Uncertainty: Optimal Control Versus Time

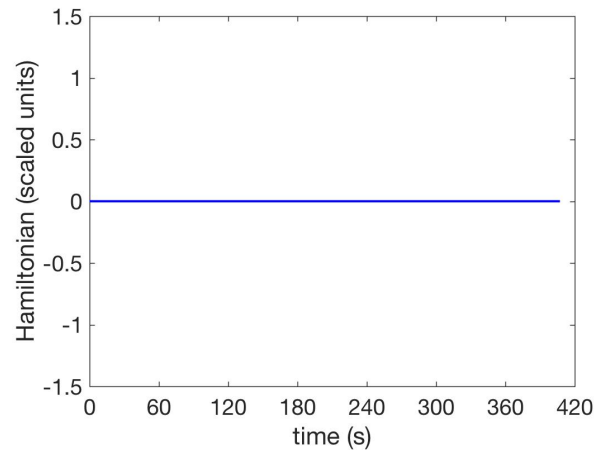


Figure 57. Solution of the Unscented Reaction Wheel Maneuver Optimum Momentum Bias Problem with Single-Axis Uncertainty: Optimal Hamiltonian Versus Time

The momentum co-state trajectories seen in Figure 58 are zero for the entire maneuver time. Co-state trajectories for the arbitrary bias cases were not as well behaved as the ones seen here which means that this solution is well balanced. The stationarity



condition (74) for the optimum momentum bias cases includes an additional path constraint, momentum, that was not present for the arbitrary cases.

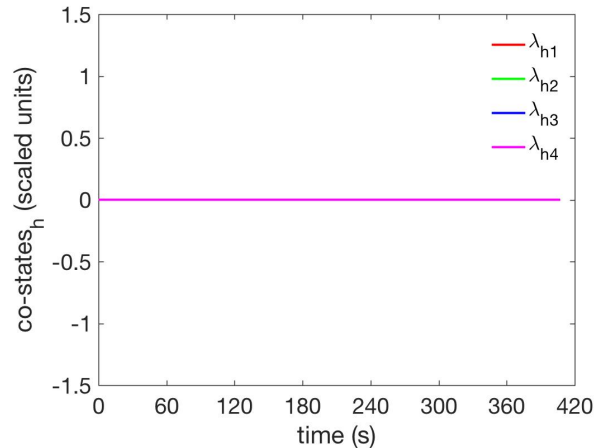


Figure 58. Solution of the Unscented Reaction Wheel Maneuver Optimum Momentum Bias Problem with Single-Axis Uncertainty: Co-States  $\lambda_h$  Versus Time

Due to the constancy of the lower Hamiltonian and momentum co-state trajectories meeting expected results, this candidate optimal control solution is considered an optimal solution to the  $ZF_{opt}$  problem.

## 2. Three-Axis Inertia Uncertainty

To further examine the three-axis uncertainty problem, an unscented reaction wheel maneuver using optimum momentum bias is solved for three-axis uncertainty. Previous results for three-axis uncertainty with arbitrary momentum bias suggested that better solutions to the problem exist. In this section, we find an improved solution to the problem. A Monte Carlo simulation of the three-axis-uncertainty optimum momentum bias is shown in Figures 59–63.

These solutions are run using the same time frame as their respective single-axis solutions, that is 407 seconds for optimum momentum bias. Referring to Figures 59–61, it is seen that uncertainty in all three axes produces different response paths for position, angular rate and momentum as compared to the three-axis uncertainty with arbitrary

momentum bias unscented reaction wheel maneuver solution and improves error statistics. The error results show this increase in fidelity with a decrease in error when compared to the three-axis uncertainty arbitrary momentum bias case and an increase in error when compared to the single-axis uncertainty optimum momentum bias case.

Both the arbitrary and optimum bias three-axis uncertainty terminal pointing errors are shown in Figures 62 and 63 along with their associated  $3\sigma$  error ellipses. Figures 62 and 63 show very clearly that the average pointing errors for the optimum bias case are less than half the amount that was seen in the arbitrary bias case but ten times greater than the errors that were seen with the optimum single-axis uncertainty case. The three-axis uncertainty optimum bias solution drives the average terminal pointing error for the large 120 deg slew to about 1.0 deg and 0.006 deg/sec. These errors are greater than the comparable closed-loop solution, but sufficiently small to enable handover to a science-mode pointing controller.

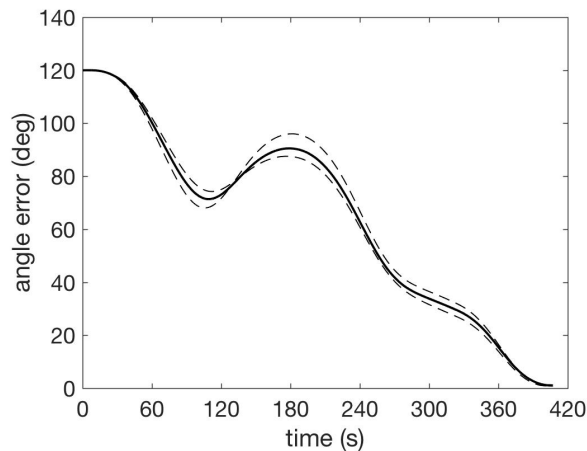


Figure 59. Unscented Reaction Wheel Maneuver Three-Axis Uncertainty Angle Error with Optimum Momentum Bias

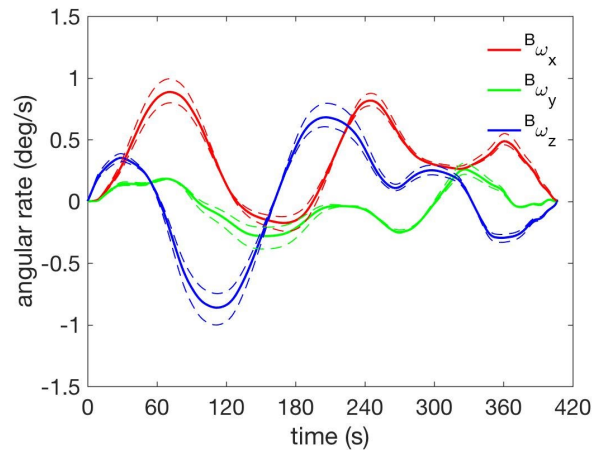


Figure 60. Unscented Reaction Wheel Maneuver Three-Axis Uncertainty Body-Frame Angular Rate with Optimum Momentum Bias

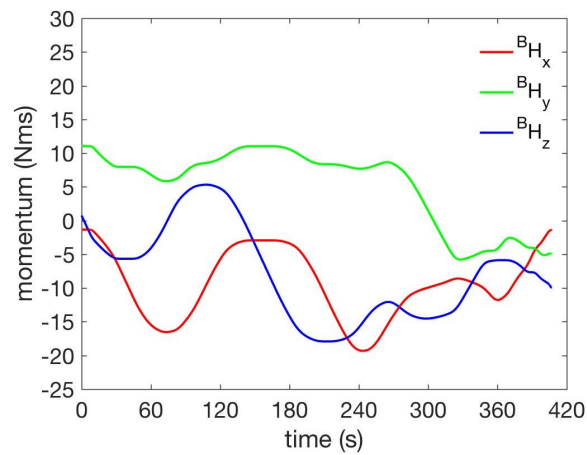


Figure 61. Unscented Reaction Wheel Maneuver Three-Axis Uncertainty Body-Frame Reaction Wheel Momentum with Optimum Momentum Bias

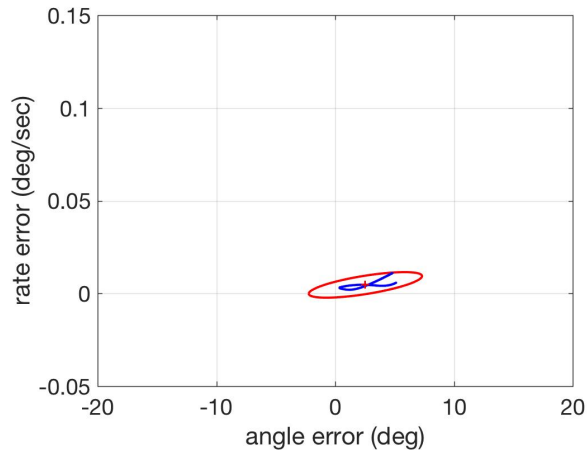


Figure 62. Monte Carlo Simulation Results of Unscented Reaction Wheel Maneuver Arbitrary Momentum Bias with Three-Axis Uncertainty: Terminal Pointing Errors

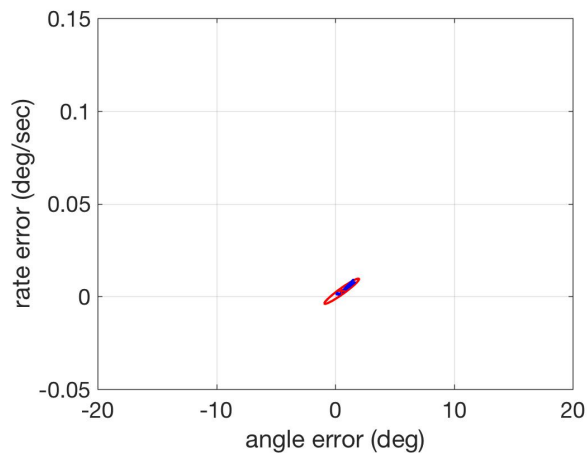


Figure 63. Monte Carlo Simulation Results of Unscented Reaction Wheel Maneuver Optimum Momentum Bias with Three-Axis Uncertainty: Terminal Pointing Errors

The four candidate control torque solution profiles,  $u_1$ ,  $u_2$ ,  $u_3$ , and  $u_4$ , one for each of the four reaction wheels are shown for the unscented reaction wheel maneuver optimum momentum three-axis uncertainty case in Figure 64. These profiles are more similar to the single-axis and three-axis uncertainty cases for arbitrary bias in that they exhibit obvious bang-bang behavior compared to the single-axis optimum bias case. This three-axis uncertainty case has the same Hamiltonian value condition stipulation as the single-axis

case, that the minimized Hamiltonian would be a constant close to zero which is consistent with a time-free problem. Figure 65 shows that the minimized Hamiltonian maintains a value close to zero for the full time of the maneuver.

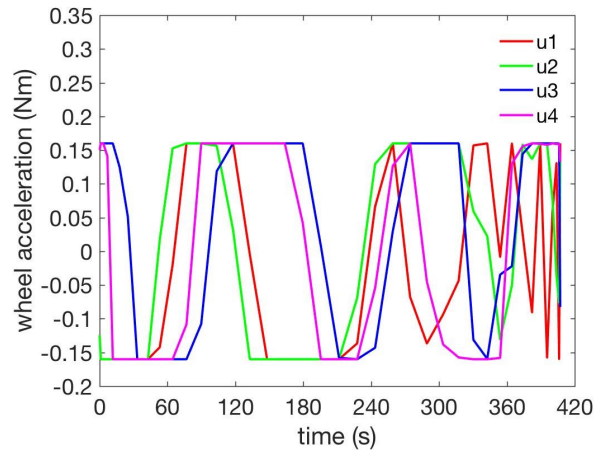


Figure 64. Solution of the Unscented Reaction Wheel Maneuver Optimum Momentum Bias Problem with Three-Axis Uncertainty: Optimal Control Versus Time

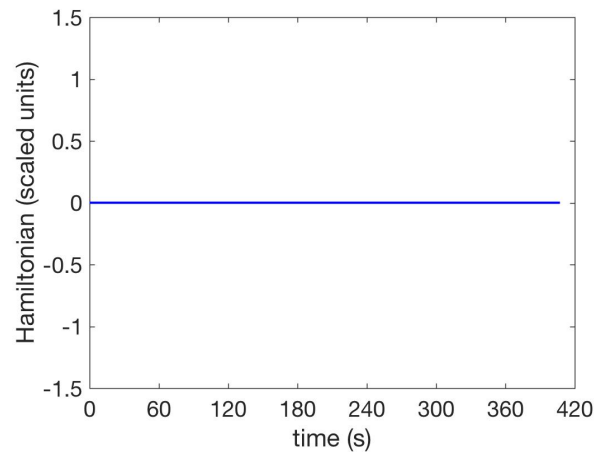


Figure 65. Solution of the Unscented Reaction Wheel Maneuver Optimum Momentum Bias Problem with Three-Axis Uncertainty: Optimal Hamiltonian Versus Time

Due to the predicted Hamiltonian meeting expected results, this candidate optimal control solution is considered an optimal solution to the  $ZF_{opt}$  problem.

### C. SUMMARY OF RESULTS

Unscented reaction wheel maneuver optimal control using unscented guidance provides terminal error statistics that are over sixty times better than comparable open-loop maneuver results. Baseline open-loop maneuvers for single-axis inertia tensor uncertainty and three-axis uncertainty were 5.50 degrees and 88.66 degrees, respectively. Unscented reaction wheel maneuver optimal control using an arbitrary momentum bias resulted in average angle error of 0.21 degrees for single-axis uncertainty and 2.47 degrees of average angle error for three-axis uncertainty, respectively. Additional average error reduction was achieved by optimizing the momentum bias as part of the control solution. This improvement was brought about through the natural feedback paths that exist in the open-loop control environment. Optimum momentum bias with single-axis uncertainty resulted in average angle error of 0.09 degrees of error while three-axis uncertainty resulted in 1.00 degree of average angle error. Table 4 summarizes these results. These results show that unscented reaction wheel maneuver optimal control is a valid method for managing open-loop uncertainty for large-angle spacecraft maneuvers.

Table 4. Statistical Performance of Unscented Reaction Wheel Maneuvering

| Control Mode<br>120 deg roll   | Average Angle<br>Error (deg) | Average Rate<br>Error (deg/sec) | Error Covariance   |
|--|------------------------------|---------------------------------|--|
| open-loop,<br>arbitrary bias,<br>1-axis error                            | 5.50                         | 0.0340                          | $\begin{bmatrix} 1.0 \times 10^1 & 6.3 \times 10^{-2} \\ 6.3 \times 10^{-2} & 3.8 \times 10^{-4} \end{bmatrix}$      |
| unscented reaction<br>wheel maneuver,<br>arbitrary bias,<br>1-axis error | 0.21                         | 0.0011                          | $\begin{bmatrix} 6.9 \times 10^{-4} & -2.2 \times 10^{-6} \\ -2.2 \times 10^{-6} & 6.9 \times 10^{-9} \end{bmatrix}$ |
| unscented reaction<br>wheel maneuver,<br>optimized bias,<br>1-axis error | 0.09                         | 0.0016                          | $\begin{bmatrix} 6.9 \times 10^{-5} & 5.8 \times 10^{-7} \\ 5.8 \times 10^{-7} & 5.9 \times 10^{-9} \end{bmatrix}$   |
| open-loop,<br>arbitrary bias,<br>3-axis error                            | 88.66                        | 0.4300                          | $\begin{bmatrix} 1.0 \times 10^1 & 6.7 \times 10^{-2} \\ 6.7 \times 10^{-2} & 4.2 \times 10^{-4} \end{bmatrix}$      |
| unscented reaction<br>wheel maneuver,<br>arbitrary bias,<br>3-axis error | 2.47                         | 0.0046                          | $\begin{bmatrix} 1.9 \times 10^0 & 1.9 \times 10^{-3} \\ 1.9 \times 10^{-3} & 3.4 \times 10^{-6} \end{bmatrix}$      |
| unscented reaction<br>wheel maneuver,<br>optimized bias,<br>3-axis error | 1.00                         | 0.0058                          | $\begin{bmatrix} 2.3 \times 10^{-2} & 2.2 \times 10^{-4} \\ 2.2 \times 10^{-4} & 2.8 \times 10^{-6} \end{bmatrix}$   |

#### D. CHAPTER SUMMARY

The purpose of this chapter was to show results of unscented reaction wheel maneuver problems with both arbitrary and optimum momentum bias and compare the approaches. The necessary conditions were used to determine if the candidate control profiles were viable solutions to the problem. Arbitrary momentum bias problems were solved exploring both single-axis and three-axis uncertainty in the inertia tensor. A Monte Carlo analysis was performed on the terminal angle and terminal rate errors to provide statistical comparison with the open-loop solution. Both average angle and average rate errors showed improvement in the arbitrary bias cases over the open-loop performance. Necessary conditions analysis was performed on both the single-axis and three-axis error candidate solutions to the arbitrary bias problem. Both solutions met the necessary

conditions for optimality. Optimum momentum bias problems were also solved for cases using both single-axis and three-axis uncertainty. Like the arbitrary bias problems, Monte Carlo analyses were performed to provide data comparison. This data showed improvement in both average angle and average rate errors compared to open-loop and arbitrary bias cases. This statistical information is summarized in Table 4. For the optimum bias cases, wheel momentum,  $\mathbf{h}(t_0)$ , was an optimizable variable, unlike previous problems. This allowed for improvement in the terminal error statistics over the arbitrary results. Necessary conditions analysis was performed on both the single-axis and three-axis error candidate solutions to the optimum bias problem and both solutions met the necessary conditions for optimality. These results show that unscented guidance is a viable approach to solving optimal control problems with inertia tensor uncertainty for reaction wheel based spacecraft.



THIS PAGE INTENTIONALLY LEFT BLANK

## VI. CONCLUSIONS AND FUTURE WORK

Failure of a satellite's attitude control feedback sensors can be mission ending unless an alternative control mode is implemented. In this dissertation, reaction wheel maneuver solutions using unscented guidance were presented to facilitate a large angle open-loop maneuver between two attitudes. Cases for both arbitrary and optimum momentum bias were studied. It was shown that natural feedback paths, which exist in the dynamics, influence the outcome of an open-loop maneuver. These paths were exploited in the optimum momentum bias cases where  $\mathbf{h}(t_0)$  was defined as an optimizable variable. The unscented reaction wheel maneuvers were shown to achieve terminal errors comparable to conventional closed-loop control, with the optimized bias solutions performing better. An unscented reaction wheel maneuver with single axis uncertainty average angle error was 0.09 degrees and three-axis error was 1.00 degree compared to comparable closed-loop average error of 0.05 degrees. An unscented reaction wheel maneuver with single axis uncertainty average rate error was 0.0016 degrees/sec and three-axis error was 0.0058 degrees/sec compared to comparable closed-loop average error of 0.0036 degrees/sec. Thus, handover to a science-mode pointing controller that uses other sensors (e.g., star-trackers or fine guidance sensors) should be possible even if further reduction in the pointing error is required for science collection. This contribution allows satellite operators another control method to extend the life of hardware compromised spacecraft.

This research suggests several paths of follow-on work for the methodology such as extension to other momentum-exchange devices e.g., control-moment-gyro (CMG) spacecraft, testing on an actual spacecraft, or exploration of spacecraft size and capability that could benefit from this methodology. Research on whether the three-axis errors seen in this dissertation can be further reduced is another topic for future work. Applications of this research to spacecraft with changing inertia tensors such as through spacecraft breakup, separation or docking are also rich areas of exploration. A formal concept of operations for using the new ideas as part of a practical mission should also be developed.

THIS PAGE INTENTIONALLY LEFT BLANK

## LIST OF REFERENCES

- [1] NASA. (2018). Kepler and K2. [https://www.nasa.gov/mission\\_pages/kepler/launch/index.html](https://www.nasa.gov/mission_pages/kepler/launch/index.html)
- [2] NASA. (2018). Kepler and K2. <https://www.nasa.gov/press-release/nasa-retires-kepler-space-telescope-passes-planet-hunting-torch>
- [3] NASA. (2018). Lunar Reconnaissance Orbiter. [https://www.nasa.gov/mission\\_pages/LRO/main/index.html](https://www.nasa.gov/mission_pages/LRO/main/index.html)
- [4] NASA. (2018). Hubble Space Telescope. [https://www.nasa.gov/mission\\_pages/hubble/story/index.html](https://www.nasa.gov/mission_pages/hubble/story/index.html)
- [5] Greenhouse, M., “The James Webb Space Telescope: Mission Overview and Status,” *AIAA SPACE 2012 Conference & Exposition*, Paper number 2012–5100, Pasadena, CA, 2012.
- [6] Spaceflight Now. (2018). Webb’s launch delayed to 2021 at an extra cost of nearly \$1 billion. <https://spaceflightnow.com/2018/06/27/webbs-launch-delayed-to-2021-at-a-cost-of-nearly-1-billion>
- [7] Meza, L., Tung, F., Anandakrishnan, S., “Line of Sight Stabilization of James Webb Space Telescope,” *Proceedings of the Twenty-Seventh American Astronautical Society Guidance and Control Conference*, AAS Paper 05–002, Breckenridge, CO, 2005.
- [8] Tate, Vincent, “Introduction to Attitude Control,” in *Spacecraft Attitude Determination and Control*, J. R. Wertz, Ed., Dordrecht, Holland: Reidel Publishing Company, 1978, pp. 502–509.
- [9] Sidi, M. J., *Spacecraft Dynamics and Control: A Practical Engineering Approach*. Cambridge University Press, NY, 2000.
- [10] Wertz, James, “Methods of Attitude Determination and Control,” in *Spacecraft Attitude Determination and Control*, J. R. Wertz, Ed., Dordrecht, Holland: Reidel Publishing Company, 1978, pp. 16–18.
- [11] DeBra, D. B., “Evolving Spacecraft Control,” *International Federation of Automatic Control (IFAC) Control Science and Technology (Eighth Triennial World Congress)*, Kyoto, Japan, 1981.
- [12] Perkel, H., “Stabilite – A Three-Axis Attitude Control System Using a Single Reaction Wheel,” *AIAA Communications Satellite Systems Conference*, Paper number 66–307, Washington, D.C., 1966.

- [13] Gunter's Space Page. (2020). TIROS. [https://space.skyrocket.de/doc\\_sdat/tiros.htm](https://space.skyrocket.de/doc_sdat/tiros.htm)
- [14] Michelson, L., "The History of Nimbus I at General Electric," *Proceedings of the AIAA Unmanned Spacecraft Meeting*, Los Angeles, CA, 1965, pp. 306–313. <https://doi.org/10.2514/6.1965-1429>
- [15] Haas, I. S., and Shapiro, R., "The Nimbus Satellite System: Remote Sensing R&D Platform of the 1970s," *AIAA Monitoring Earth's Ocean, Land and Atmosphere from Space-Sensors, Systems, and Applications*, 1985, pp. 71–95. <https://doi.org/10.2514/4.865725>
- [16] Siegel, S. H., and Das, A., "Unusual Maneuvers on Nimbus and Landsat Spacecraft," *Journal of Guidance, Control, and Dynamics*, Vol. 1, No. 1, 1978, pp. 95–96. <https://doi.org/10.2514/3.55749>
- [17] Gunter's space page. (2020). Orbiting Geophysical Observatory. [https://space.skyrocket.de/doc\\_sdat/ogo.htm](https://space.skyrocket.de/doc_sdat/ogo.htm)
- [18] TechCrunch. (2019). SpaceX reveals more Starlink info after launch of first 60 satellites. <https://techcrunch.com/2019/05/24/spacex-reveals-more-starlink-info-after-launch-of-first-60-satellites>
- [19] Union of Concerned Scientists. (2022). "UCS Satellite Database," updated December 31, 2021. <https://www.ucsusa.org/resources/satellite-database>
- [20] Hedrick, Dale, "Momentum and Reaction Wheels," in *Spacecraft Attitude Determination and Control*, J. R. Wertz, Ed., Dordrecht, Holland: Reidel Publishing Company, 1978, pp. 201–203.
- [21] Griffin, Michael D., and French, James R., *Space Vehicle Design*, AIAA Education Series, J. S. Przemieniecki, Series Editor-in-Chief, Washington, D.C.: AIAA, 1991.
- [22] Markley, F. L., and Crassidis, J. L., *Fundamentals of Spacecraft Attitude Determination and Control*. Springer, NY, 2014.
- [23] Blair, W. P., Kruk, J. W., Moos, H. W., and Oegerle, W. R., "Operations with the FUSE Observatory," *Future EUV/UV and Visible Space Astrophysics Missions and Instrumentation*, Proceedings of SPIE, Vol. 4854, Feb. 2003, pp. 241–250. <https://doi.org/10.1117/12.459814>
- [24] Moos, H. W., Cash, W. C., Cowie, L. L. et al., "Overview of the Far Ultraviolet Spectroscopic Explorer Mission," *The Astrophysical Journal*, Vol. 538, July 2000, pp. L1–L6.

- [25] Kruk, J. W., Class, B. F., Rovner, D., Westphal, J., Ake, T. B., Moos, H. W., Roberts, B. A., and Fisher, L., “FUSE In-Orbit Attitude Control with Two Reaction Wheels and No Gyroscopes,” *Future EUV/UV and Visible Space Astrophysics Missions and Instrumentation*, Proceedings of SPIE, Vol. 4854, Feb. 2003, pp. 274–285. <https://doi.org/10.1117/12.459948>
- [26] Class, B. F., Kruk, J. W., White, M., Ake, T. B., Rovner, D., and Abate, M., “FUSE – Emergency Operations and One Wheel Gyroless Fine Pointing Control,” *Proceedings of the Thirtieth American Astronautical Society Guidance and Control Conference*, AAS Paper 07–005, Breckenridge, CO, 2007.
- [27] Vanelli, C. A., Swenka, D., and Smith, B., “Verification of Pointing Constraints for the Dawn Spacecraft,” *Proceedings of the AAS/AIAA Astrodynamics Specialist Conference*, AIAA Paper 2008–7085, Honolulu, HI, 2008. <https://doi.org/10.2514/6.2008-7085>
- [28] Thomas, V. C., Makowski, J. M., Brown, G. M., McCarthy, J. F., Bruno, D., Cardoso, J. C., Chiville, W. M., Meyer, T. F., Nelson, K. E., Pavri, B. E., Termohlen, D. A., Violet, M. D., and Williams, J. B., “The Dawn Spacecraft,” *Space Science Review*, Springer Science+Business Media B. V., 2011. <https://doi.org/10.1007/s11214-011-9852-2>
- [29] Anderson, G. C., Quinn, D. A., Beals, G. A., Nelson, J. D., and Nurre G. S., “An Overview of the Hubble Space Telescope Pointing Control System Design and Operation,” *AIAA Guidance, Navigation and Control Conference*, Paper number 92–4616, Hilton Head Island, SC, 1992. <https://doi.org/10.2514/6.1992-4616>
- [30] O’Donnell, Jr., J. R., and Hoffman, H. C., “Zero-Gyro Control of the International Ultraviolet Explorer,” *AIAA Guidance, Navigation and Control Conference*, Paper number 93–3760, Monterey, CA, 1993. <https://doi.org/10.2514/6.1993-3760>
- [31] Calhoun, P. C., and Garrick, J. C., “Observing Mode Attitude Controller for the Lunar Reconnaissance Orbiter,” *Proceedings of the Twentieth International Symposium on Space Flight Dynamics*, Annapolis, MD, 2007.
- [32] Simpson, J., Badgley, J., McCaughey, K., Brown, K., Calhoun, P., Davis, E., Garrick, J., Gill, N., Hsu, O., Jones, N., Ortiz-Cruz, G., Raymond, J., Roder, R., Shah, N., and Wilson, J., “Integration and Testing of the Lunar Reconnaissance Orbiter Attitude Control System,” *IEEE Aerospace Conference*, Big Sky, MT, 2011. <https://doi.org/10.1109/AERO.2011.5747274>
- [33] Domingo, V., Fleck B., and Poland, A. I., “The SOHO Mission: An Overview,” *Solar Physics*, Kluwer Academic Publishers provided by the NASA Astrophysics Data System, Vol. 162, 1995, pp. 1–37; [http://articles.adsabs.harvard.edu/cgi-bin/nph-iarticle\\_query?1995SoPh..162....1D&defaultprint=YES&filetype=.pdf](http://articles.adsabs.harvard.edu/cgi-bin/nph-iarticle_query?1995SoPh..162....1D&defaultprint=YES&filetype=.pdf)

- [34] Dellinger W. F., and Shapiro, H. S., “Attitude Control on Two Wheels and No Gyros – The Past, Present and Future of the TIMED Spacecraft,” *Proceedings of the AAS/AIAA Astrodynamics Specialist Conference*, AIAA Paper 2008–6258, Honolulu, HI, 2008. <https://doi.org/10.2514/6.2008-6258>
- [35] Durham, D., and Itchkawich, T., “The Story of Glory: Earth and Solar Science on One Unique Satellite,” *IEEE Aerospace Conference*, Big Sky, MT, 2005. <https://doi.org/10.1109/AERO.2005.1559334>
- [36] NASA, “Press Kit/June 2009 LRO/LCROSS,” National Aeronautics and Space Administration, NP-2009-05-98-MSFC, Huntsville, AL, June 2009; <https://www.nasa.gov/>
- [37] Halverson, J., Calhoun, P., Hsu, O., Dongmo, J.-E., Besser, R., Ellis, B., DeHart, R., Tesla, Y., Rosen, S., and Snell, S., “Testing of the Lunar Reconnaissance Orbiter Attitude Control System Re-Design Without a Gyro,” *Proceedings of the Forty-Second American Astronautical Society Guidance and Control Conference*, AAS Paper 19–108, Breckenridge, CO, 2019.
- [38] Bruno, D., Class, B. F., and Keller, B., “Lessons Learned: A Review of NESC GN&C Best Practices as Pertaining to Commercial and Scientific Satellite Development,” *AIAA Guidance, Navigation and Control Conference*, Paper number 2007–6337, Hilton Head Island, SC, 2007. <https://doi.org/10.2514/6.2007-6337>
- [39] Janson, S. W., “Micro/Nanotechnology for the Satellite World,” *MEMS Components and Applications for Industry, Automobiles, Aerospace, and Communication II*, Proceedings of SPIE, Vol. 4981, Jan. 2003, pp. 95–106. <https://doi.org/10.1117/12.476315>
- [40] Honeywell Aerospace, “HG4930 MEMS Inertial Measurement Unit,” Honeywell International, Inc., N61-1523-000-012I, Minneapolis, MN, Oct. 2019; <https://aerospace.honeywell.com/en/learn/products/sensors/hg4930-mems-inertial-measurement-unit>
- [41] Fallon III, Lawrence, “Gyroscopes,” in *Spacecraft Attitude Determination and Control*, J. R. Wertz, Ed., Dordrecht, Holland: Reidel Publishing Company, 1978, pp. 199.
- [42] Agasid, E., Burton, R., Carlino, R. Defouw, G., Dono-Perez, A., Goktug-Karacalioglu, A., Klamm, B., Rademacher, A., Schalkwyck, J., Shimmin, R., Tilles, J., and Weston, S., “Small Spacecraft Technology State of the Art,” NASA TP-20018-220027, Dec. 2018.
- [43] Space Micro, “MSS-01, 02 Medium Sun Sensors,” Space Micro, Medium Sun Sensors Data Sheet, San Diego, CA, Dec. 2015.

- [44] Adcole Space, “Digital Sun Sensor (+/-64 deg),” Adcole Space, Digital Sun Sensor Specifications Sheet, Marlborough, MA, Sep. 2020.
- [45] Janson, S. W., “25 Years of Small Satellites,” *Twenty-fifth Annual AIAA/USU Conference on Small Satellites*, Paper number SSC11-III-1, Logan UT, 2011.
- [46] Lerner, Gerald M., “Sun Sensors” in *Spacecraft Attitude Determination and Control*, J. R. Wertz, Ed., Dordrecht, Holland: Reidel Publishing Company, 1978, pp. 157.
- [47] Fossum, E. R., “CMOS Image Sensors: Electronic Camera on a Chip,” *IEEE Transactions on Electron Devices*, Vol. 44, No. 10, 1997, pp. 1.3.1-1.3.9.
- [48] Janson, S. W., “Micro/Nanotechnology for Micro/Nano/Picosatellites,” *AIAA SPACE 2003 Conference & Exposition*, Paper number 2003-6269, Long Beach, CA, 2003.
- [49] Marin, M., and Bang, H., “High Update Rate Star Tracker for Gyroless Spacecraft Operation,” *2018 Fifth IEEE International Workshop on Metrology for AeroSpace (MetroAeroSpace)*, Rome, Italy, 2018. <https://doi.org/10.1109/MetroAeroSpace.2018.8453507>
- [50] Hoffman, Jr., H. C., “Lessons Learned from Six Decades of Spacecraft Guidance and Control Experiences,” *AIAA Guidance, Navigation and Control Conference*, Paper number 2007-6333, Hilton Head Island, SC, 2007. <https://doi.org/10.2514/6.2007-6333>
- [51] Stoneking, E., and Lebsock, K., “Pointing and Maneuvering a Spacecraft with a Rank-Deficient Reaction Wheel Complement,” *Proceedings of the Thirty-Seventh American Astronautical Society Guidance and Control Conference*, AAS Paper 14-103, Breckenridge, CO, 2014.
- [52] Karpenko, M., Kang, W., Proulx, R., and Ross, I.M., “Precision Pointing for a Skewed 2-Reaction Wheel Control System,” *Proceedings of the Thirty-Seventh American Astronautical Society Guidance and Control Conference*, AAS Paper 14-104, Breckenridge, CO, 2014.
- [53] Femiano, M. D., “Inflight Redesign of the IUE Attitude Control System,” *AIAA Space Systems Technology Conference*, Paper number 1986-1193, San Diego, CA, 1986. <https://doi.org/10.2514/6.1986-1193>
- [54] NASA. (2018). Hubble Space Telescope. <https://www.nasa.gov/content/the-hubble-story>



- [55] Clapp, B. R., Ramsey, P. R., Wirzburger, J. H., Smith, D. C., and Van Arsdall, J. C., “Hubble Space Telescope Reduced-Gyro Control Law Design, Implementation, and On-Orbit Performance,” *Proceedings of the Eighteenth Annual AAS/AIAA Spaceflight Mechanics Meeting*, AAS Paper 08–278, Galveston, TX, 2008.
- [56] Clapp, B. R., “Hubble Space Telescope Reduced-Gyro Control System,” *Journal of the Astronautical Sciences*, Vol. 57, No. 1–2, 2009, pp. 419–456.
- [57] Carmi, A. and Oshman, Y., “Vector Observations-Based Gyroless Spacecraft Attitude/Angular Rate Estimation Using Particle Filtering,” *AIAA Guidance, Navigation and Control Conference*, Paper number 2006–6597, Keystone, CO, 2006. <https://doi.org/10.2514/6.2006-6597>
- [58] Bruno, D., Class, B. F., Rovner, D., Baird, G., Groszkiewicz, J., Lebsock, K., and Kruk, J., “A Comparison of Gyroless Implementations of Scientific Spacecraft,” *AIAA Guidance, Navigation and Control Conference*, Paper number 2009–5942, Chicago, IL, 2009. <https://doi.org/10.2514/6.2009-5942>
- [59] Bowles, T. and Croft, J., “Analytical Derivation and Verification of Zero-Gyro Control for the IUE Satellite,” *NASA Technical Memorandum 100748*, 1989.
- [60] Markley, F. L. and Nelson, J. D., “A Zero-Gyro Safemode Controller for HST,” *AIAA Guidance, Navigation and Control Conference*, Paper number 92–4613, Hilton Head Island, SC, 1992. <https://doi.org/10.2514/6.1992-4613>
- [61] Markley, F. L., Anderson, G. C., and Nelson, J. D., “On-Orbit Test of the HST Zero-Gyro Safemode Controller,” *AIAA Guidance, Navigation and Control Conference*, Paper number 1993–3831, Monterey, CA, 1993. <https://doi.org/10.2514/6.1993-3831>
- [63] Pepe, J. and Myslinski, M., “Evolution of the Hubble Space Telescope Safing System,” *AIAA SpaceOps 2006 Conference*, Paper number 2006–5937, Rome, Italy, 2006. <https://doi.org/10.2514/6.2006-5937>
- [63] Podgorski, W. A., Lemos, L. K., Cheng, J., and Daly, K. C., “Gyroless Attitude Determination and Control System for Advanced Environmental Satellites,” *AIAA Guidance and Control Conference*, Paper number 1982–1614, San Diego, CA, 1982. <https://doi.org/10.2514/6.1982-1614>
- [64] Bauer, F. H. and Dellinger, W., “Gyroless Fine Pointing on Small Explorer Spacecraft,” *AIAA Guidance, Navigation and Control Conference*, Paper number 1993–3756, Monterey, CA, 1993. <https://doi.org/10.2514/6.1993-3756>
- [65] Rao, G. N., Alex, T. K., and Bhat, M. S., “Incremental-Angle and Angular Velocity Estimation Using a Star Sensor,” *Journal of Guidance, Control, and Dynamics*, Vol. 25, No. 3, 2002, pp. 433–441. <https://doi.org/10.2514/2.4928>

- [66] Calabrese, D., Nicito, A., Viscio, M. A., Ricci, C., De Luca, G. F., and Fasano, L., Nirchio, F., “COSMO-SkyMed Full Gyroless Operative Modes: Verification Results,” *AIAA SpaceOps 2018 Conference*, Paper number 2018–2307, Marseille, France, 2018. <https://doi.org/10.2514/6.2018-2307>
- [67] Gai, E., Daly, K., Harrison, J., Lemos, L., “Star-Sensor-Based Satellite Attitude/Attitude Rate Estimator,” *Journal of Guidance, Control, and Dynamics*, Vol. 8, No. 5, 1985, pp. 560–565. <https://doi.org/10.2514/3.56393>
- [68] Grewal, M. S. and Shiva, M., “Application of Kalman Filtering to Gyroless Attitude Determination and Control System for Environmental Satellites,” *IEEE Proceedings of the Thirty-Fourth Conference on Decision & Control*, New Orleans, LA, 1995, pp. 1544–1552.
- [69] Liebe, C. C., “Star Trackers for Attitude Determination,” *IEEE AES Systems Magazine*, June 1995, pp.10-16.
- [70] Crassidis, J. L., “Angular Velocity Determination Directly from Star Tracker Measurements,” *Journal of Guidance, Control, and Dynamics*, Vol. 25, No. 6, 2002, pp. 1165–1168. <https://doi.org/10.2514/2.4999>
- [71] Fisher, J. and Vadali, S. R., “Gyroless Attitude Control of Multi-Body Satellites Using an Unscented Kalman Filter,” *Proceedings of the AAS/AIAA Astrodynamics Specialist Conference*, AIAA Paper 2006–6163, Keystone, CO, 2006 <https://doi.org/10.2514/6.2006-6163>
- [72] Liu, D. and Chiang, R., “Spacecraft Acquisition Maneuvers Using Position Based Gyroless Control,” *AIAA Guidance, Navigation and Control Conference*, Paper number 2009–5945, Chicago, IL, 2009. <https://doi.org/10.2514/6.2009-5945>
- [73] Mushaweh, N., Jenkins, B., Castelli D. A., and Thein, M.-W. L., “A Comparative Analysis of Body-Rate Estimation Techniques for the NASA Magnetospheric Multiscale (MMS) Mission Spacecraft,” *AIAA Guidance, Navigation and Control Conference*, Paper number 2009–5949, Chicago, IL, 2009. <https://doi.org/10.2514/6.2009-5949>
- [74] Bae, J., Kim, Y., and Kim, H. S., “Satellite Attitude Determination and Estimation Using Two Star Trackers,” *AIAA Guidance, Navigation and Control Conference*, Paper number 2010–8447, Toronto, Ontario, Canada, 2010. <https://doi.org/10.2514/6.2010-8447>
- [75] Yafei, Y. and Jianguo, L., “Particle Filtering for Gyroless Attitude/Angular Rate Estimation Algorithm,” *IEEE Proceedings of the 2010 First International Conference on Pervasive Computing, Signal Processing and Applications*, Mannheim, Germany, 2010, pp. 1188–1191.

- [76] Thienel, J. K. and Markley, F. L., “Comparison of Angular Velocity Estimation Methods for Spinning Spacecraft,” *AIAA Guidance, Navigation and Control Conference*, Paper number 2011–6432, Portland, OR, 2011. <https://doi.org/10.2514/6.2011-6432>
- [77] Chiang, R. Y. and Tsao, T., “Star Tracker Rate Estimation with Kalman Filter Enhancement,” *AIAA Guidance, Navigation and Control Conference*, Paper number 2013–5024, Boston, MA, 2013. <https://doi.org/10.2514/6.2013-5024>
- [78] Jo, S., Choi, Y. and Bang, H., “Optimal Angular Velocity Estimation of Spacecraft Using Only Star Tracker Measurements,” *Journal of Guidance, Control, and Dynamics*, Vol. 38, No. 2, 2015, pp. 342–346 <https://doi.org/10.2514/1.G000739>
- [79] Kazemi, L., Enright, J., Dzamba, T., and Raahemifar, K., “Satellite Angular Velocity Estimation Based on Optical Flow Techniques,” *AIAA SciTech Forum at the AIAA Guidance, Navigation and Control Conference*, Paper number 2015–1335, Kissimmee, FL, 2015. <https://doi.org/10.2514/6.2015-1335>
- [80] De Luca, G. F., Fasano, L., Cardone, M., Loizzo, R., Carpentiero, R., De Angelis, L., Nicito, A., Anania, M., and Cascone, D., “Pseudo and Full-Gyroless Operative Modes on Board of COSMO-SkyMed Mission,” *AIAA SpaceOps 2016 Conference*, Paper number 2016–2469, Daejeon, South Korea, 2016. <https://doi.org/10.2514/6.2016-2469>
- [81] Leeghim, H., Bang, H. and Lee, C.-Y., “Angular Rate and Alignment Estimation for Gyroless Spacecraft by Only Star Trackers,” *International Journal of Control, Automation and Systems*, 2018. <http://dx.doi.org/10.1007/s12555-017-0750-6>
- [82] Rankin, K., Stochaj, S., Krizmanic, J., Shah, N., and Naseri, A., “Virtual Telescope for X-Ray Observations,” *Thirty-Third Annual AIAA/USU Conference on Small Satellites*, Paper number SSC19-WKVII-09, Logan, UT, 2019.
- [83] Capello, E. and Fujisaki, Y., “Robust Consensus of Second-Order Heterogeneous Multi-Agent Systems via Dynamic Interaction,” *2020 Fifty-Ninth IEEE Conference on Decision and Control (CDC)*, Jeju Island, South Korea, 2020, pp. 524–529.
- [84] Yoon, H., Riesing, K. M., and Cahoy, K., “Kalman Filtering for Attitude and Parameter Estimation of Nanosatellites Without Gyroscopes,” *Journal of Guidance, Control and Dynamics* Vol. 40, No.9, 2017, pp. 2272–2288. <https://doi.org/10.2514/1.G002649>
- [85] Bar-Itzhack, I. Y., “Classification of Algorithms for Angular Velocity Estimation,” *Journal of Guidance, Control and Dynamics*, Vol. 24, No. 2, 2001, pp. 214–218. <https://doi.org/10.2514/2.4731>

- [86] Harman, R. R. and Bar-Itzhack, I. Y., “The Use of Pseudo-Linear and SDARE Filtering for Satellite Angular-Rate Estimation,” *AIAA Guidance, Navigation and Control Conference*, Paper number 1998–4312, Boston, MA, 1998. <https://doi.org/10.2514/6.1998-4312>
- [87] Challa, M., Kotaru, S., and Natanson, G., “Magnetometer-Only Attitude and Rate Estimates During the Earth Radiation Budget Satellite 1987 Control Anomaly,” *AIAA Guidance, Navigation and Control Conference*, Paper number 1997–3615, New Orleans, LA, 1997. <https://doi.org/10.2514/6.1997-3615>
- [88] Lerner, G. M. and Shuster, M. D., “Magnetometer Bias Determination and Attitude Determination for Near-Earth Spacecraft,” *AIAA Guidance and Control Conference*, Paper number 1979–1695, Boulder, CO, 1979. <https://doi.org/10.2514/6.1979-1695>
- [89] Psiaki, M. L., Martel, F., and Pal, P. K., “Three-Axis Attitude Determination via Kalman Filtering of Magnetometer Data,” *Journal of Guidance, Control and Dynamics*, Vol. 13, No. 3, 1989, pp. 506–514. <https://doi.org/10.2514/3.25364>
- [90] Flatley, T. W., Forden, J. K., Henretty, D. A., Lightsey, E. G., and Markley, F. L., “On-Board Attitude Determination and Control Algorithms for SAMPEX,” *Proceedings of the 1990 Flight Mechanics/Estimation Theory Symposium*, NASA - Goddard Space Flight Center, 1990, pp. 379–398.
- [91] Polites, M. E. and Lightsey, W. D., “A Nonlinear Estimator for Reconstructing the Angular Velocity of a Spacecraft Without Rate Gyros,” *NASA Technical Paper 3178*, 1991.
- [92] Natanson, G., “A Deterministic Method for Estimating Attitude from Magnetometer Data Only,” *Proceedings of the Forty-Third IFA Congress*, Paper number IFA-92-0036, Washington, DC, 1992.
- [93] Natanson, G. A., Challa, M. S., Deutschmann, J., and Baker, D. F., “Magnetometer-Only Attitude and Rate Determination for a Gyroless Spacecraft,” *Proceedings of the Third International Symposium on Space Mission Operations and Ground Data Systems*, NASA Conference Publication 3281, Greenbelt, MD, 1994, pp. 791–798.
- [94] Challa, M., Natanson, G., Deutschmann, J., and Galal, K., “A PC-Based Magnetometer-Only Attitude and Rate Determination System for Gyroless Spacecraft,” *Proceedings of the 1995 Flight Mechanics/Estimation Theory Symposium*, NASA - Goddard Space Flight Center, 1995, pp. 83–96.
- [95] Azor, R., Bar-Itzhack, I. Y., and Harman, R. P., “Satellite Angular Rate Estimation from Vector Measurements,” *AIAA Guidance, Navigation and Control Conference*, AIAA Paper 1996–3751, San Diego, CA, 1996. <https://doi.org/10.2514/6.1996-3751>

- [96] Challa, M., Natanson, G., Wheeler, C., “Simultaneous Determination of Spacecraft Attitude and Rates Using Only a Magnetometer,” *Proceedings of the AAS/AIAA Astrodynamics Specialist Conference*, AIAA Paper 1996–3630, San Diego, CA, 1996. <https://doi.org/10.2514/6.1996-3630>
- [97] Challa, M., Kotaru, S., and Natanson, G., “Magnetometer-Only Attitude and Rate Estimates During the Earth Radiation Budget Satellite 1987 Control Anomaly,” *AIAA Guidance, Navigation and Control Conference*, Paper number 1997–3615, New Orleans, LA, 1997. <https://doi.org/10.2514/6.1997-3615>
- [98] Azor, R., Bar-Itzhack, I. Y., Deutschmann, J. K., and Harman, R. R., “Angular-Rate Estimation Using Delayed Quaternion Measurements,” *AIAA Guidance, Navigation and Control Conference and Exhibit*, Paper number 1999–3972, Portland, OR, 1999. <https://doi.org/10.2514/6.1999-3972>
- [99] Harman, R. R. and Bar-Itzhack, I. Y., “Pseudolinear and State-Dependent Riccati Equation Filters for Angular Rate Estimation,” *Journal of Guidance, Control and Dynamics*, Vol. 22, No. 5, 1999, pp. 723–725. <https://doi.org/10.2514/2.4442>
- [100] Challa, M., Natanson, G., and Ottenstein, N., “Magnetometer-Only Attitude and Rate Estimates for Spinning Spacecraft,” *Proceedings of the AAS/AIAA Astrodynamics Specialist Conference*, AIAA Paper 2000–4241, Denver, CO, 2000. <https://doi.org/10.2514/6.2000-4241>
- [101] Tortora, P. and Oshman, Y., “Spacecraft Angular Rate Estimation from Magnetometer Data Only,” *Proceedings of the AAS/AIAA Astrodynamics Specialist Conference*, AIAA Paper 2000–4240, Denver, CO, 2000. <https://doi.org/10.2514/6.2000-4240>
- [102] Bar-Itzhack, I. Y. and Harman, R. R., “The Effect of Sensor Failure on the Attitude and Rate Estimation of the MAP Spacecraft,” *AIAA Guidance, Navigation and Control Conference and Exhibit*, Paper number 2003–5485, Austin, TX, 2003. <https://doi.org/10.2514/6.2003-5485>
- [103] Psiaki, M. L., “Global Magnetometer-Based Spacecraft Attitude and Rate Estimation,” *AIAA Guidance, Navigation and Control Conference and Exhibit*, Paper number 2003–5561, Austin, TX, 2003. <https://doi.org/10.2514/6.2003-5561>
- [104] Baird, G. C. and Groszkiewicz, J. E., “Gyroless Attitude Control for the SORCE Spacecraft,” *Proceedings of the Twenty-Seventh Annual AAS Guidance and Control Conference*, AAS Paper number 04–076, Breckenridge, CO, 2004.
- [105] Ahn, H.-S., Lee, S.-H., “Gyroless Attitude Estimation of Sun-Pointing Satellites Using Magnetometers,” *IEEE Geoscience and Remote Sensing Letters*, Vol. 2, No. 1, 2005, pp. 8–12.

- [106] Carmi, A. and Oshman, Y., “Robust Spacecraft Angular-Rate Estimation from Vector Observations Using Fast Interlaced Particle Filtering,” *AIAA Guidance, Navigation and Control Conference and Exhibit*, Paper number 2005–6399, San Francisco, CA, 2005. <https://doi.org/10.2514/6.2005-6399>
- [107] Stoneking, E., and Lebsock, K., “A Gyroless Safehold Control Law Using Angular Momentum as an Inertial Reference Vector,” *AIAA Guidance, Navigation and Control Conference and Exhibit*, Paper number 2008–7016, Honolulu, HI, 2008. <https://doi.org/10.2514/2008-7016>
- [108] Cheon, Y.-J., Lee, S.-H., and Kim, J.-H., “Fully Magnetic Devices-Based Control for Gyroless Target Pointing of a Spinning Spacecraft,” *IEEE Transactions on Aerospace and Electronic Systems*, Vol. 46, No. 3, 2010, pp. 1484–1491.
- [109] Pong, C. M., Knutson, M. W., Miller, D. W., Seager, S., Lim, S., Henderson, T. C., and Murphy, S. D., “High-Precision Pointing and Attitude Determination and Control on ExoplanetSat,” *AIAA Guidance, Navigation and Control Conference and Exhibit*, Paper number 2012–4783, Minneapolis, MN, 2012. <https://doi.org/10.2514/6.2012-4783>
- [110] Tsao, T. and Chiang, R. Y., “Gyroless 3-Axis Sun Acquisition via Sun Sensors Only Unscented Kalman Filter Estimation,” *AIAA Guidance, Navigation and Control Conference and Exhibit*, Paper number 2013–5025, Boston, MA, 2013. <https://doi.org/10.2514/6.2013-5025>
- [111] Robinson, J. B. and Richie, D. J., “Stabilization and Attitude Determination Methods for FalconSAT-3,” *Journal of Spacecraft and Rockets*, Vol. 53, No. 3, 2016, pp. 507–519. <https://doi.org/10.2514/1.A3362>
- [112] Sugimura, N., Kuwahara, T., and Yoshida, K., “Attitude Determination and Control System for Nadir Pointing Using Magnetorquer and Magnetometer,” *Proceedings of the IEEE 2016 Conference on Aerospace*, Big Sky, MT, 2016.
- [113] Challa, M. S., “Simultaneous Estimation of Attitude and Markov-Modeled Rate Corrections of Gyroless Spacecraft,” *Journal of Guidance, Control and Dynamics*, Vol. 40, No. 9, 2017, pp. 2381–2387. <https://doi.org/10.2514/1.G002718>
- [114] Axelrad, P. and Chesley, B. C., “Performance Testing of a GPS Based Attitude Determination System,” *AIAA Guidance, Navigation and Control Conference*, Paper number 93–3787, Monterey, CA, 1993. <https://doi.org/10.2514/6.1993-3787>
- [115] Fujikawa, S. J. and Zimelman, D. F., “Spacecraft Attitude Determination by Kalman Filtering of Global Positioning System Signals,” *Journal of Guidance, Control and Dynamics*, Vol. 18, No. 6, 1995, pp. 1365–1371. <https://doi.org/10.2514/3.21554>



- [116] Axelrad, P. and Ward, L. M., “Spacecraft Attitude Estimation Using the Global Positioning System: Methodology and Results for RADCAL,” *Journal of Guidance, Control and Dynamics*, Vol. 19, No. 6, 1996, pp. 1201–1209. <https://doi.org/10.2514/3.21772>
- [117] Crassidis, J. L. and Markley, F. L., “Attitude Determination Using Global Positioning Signals,” *AIAA Guidance, Navigation and Control Conference*, Paper number 1997–3452, New Orleans, LA, 1997. <https://doi.org/10.2514/6.1997-3452>
- [118] Crassidis, J. L., Lightsey, E. G., and Markley, F. L., “Efficient and Optimal Attitude Determination Using Recursive Global Positioning System Signal Operations,” *AIAA Guidance, Navigation and Control Conference and Exhibit*, Paper number 1998–4496, Boston, MA, 1998. <https://doi.org/10.2514/6.1998-4496>
- [119] Axelrad, P. and Behre, C. P., “Satellite Attitude Determination Based on GPS Signal-to-Noise Ratio,” *Proceedings of the IEEE*, Vol. 87, No. 1, 1999, pp. 133–144.
- [120] Crassidis, J. L. and Lightsey, E. G., “Attitude Determination Using Combined GPS and Three-Axis Magnetometer Data,” *Space Technology: Journal of the International Forum on Automatic Control*, Vol. 20, No. 4, 2001, pp. 147–156.
- [121] Lightsey, E. G. and Madsen, J., “Three-Axis Attitude Determination Using Global Positioning System Signal Strength Measurements,” *Journal of Guidance, Control and Dynamics*, Vol. 26, No. 2, 2003, pp. 304–310. <https://doi.org/10.2514/2.5047>
- [122] Madsen, J. and Lightsey, E. G., “Robust Spacecraft Attitude Determination Using Global Positioning System Receivers,” *Journal of Spacecraft and Rockets*, Vol. 41, No. 4, 2004, pp. 635–643. <https://doi.org/10.2514/1.1324>
- [123] Wahba, G., “A Least Squares Estimate of Satellite Attitude,” *SIAM Review*, Vol. 7, No. 3, 1965, pp. 409.
- [124] Shuster, M. D. and Oh, S. D., “Three-Axis Attitude Determination From Vector Observations,” *Journal of Guidance and Control*, Vol. 4, No.1, 1981, pp. 70–77. <https://doi.org/10.2514/3.19717>
- [125] Lefferts, E. J., Markley, F. L., and Shuster, M. D., “Kalman Filtering for Spacecraft Attitude Estimation,” *AIAA Twentieth Aerospace Sciences Meeting*, Paper number 1982–0070, Orlando, FL, 1982. <https://doi.org/10.2514/6.1982-70>
- [126] Mook, D. J. and Junkins, J. L., “Minimum Model Error Estimation for Poorly Modeled Dynamic Systems,” *AIAA Twenty-Fifth Aerospace Sciences Meeting*, Paper number 1987–0173, Reno, NV, 1987. <https://doi.org/10.2514/6.1987-173>

- [127] Markley, F. L., “Attitude Determination and Parameter Estimation Using Vector Observations,” *AIAA Astrodynamics Conference*, Paper number 1988–4225, Minneapolis, MN, 1988. <https://doi.org/10.2514/6.1988-4225>
- [128] De Pena, J., Crassidis, J. L., McPartland, M. D., Meyer, T. J., and Mook, D. J., “MME-Based Attitude Dynamics Identification and Estimation for SAMPEX,” *Proceedings of the 1994 Flight Mechanics/Estimation Theory Symposium*, NASA - Goddard Space Flight Center, 1994, pp. 497–511.
- [129] Crassidis, J. L. and Markley, F. L., “A Minimum Model Error Approach for Attitude Estimation,” *AIAA Guidance, Navigation and Control Conference*, Baltimore, MD, 1995. <https://doi.org/10.2514/6.1995-3276>
- [130] Crassidis, J. L. and Markley, F. L., “Predictive Filtering for Attitude Estimation Without Rate Sensors,” *Journal of Guidance, Control and Dynamics* Vol. 20, No.3, 1997, pp. 522–527. <https://doi.org/10.2514/2.4071>
- [131] Oshman, Y. and Markley, F. L., “Sequential Gyroless Attitude/Attitude-Rate Estimation Using Integrated-Rate Parameters,” *AIAA Guidance, Navigation and Control Conference and Exhibit*, Paper number 1998–4508, Boston, MA, 1998. <https://doi.org/10.2514/6.1998-4508>
- [132] Shuster, M. D., “A Broad Look at Deterministic Three-Axis Attitude Determination,” *Proceedings of the AAS/AIAA Astrodynamics Specialist Conference*, AIAA Paper 2000–4239, Denver, CO, 2000. <https://doi.org/10.2514/6.2000-4239>
- [133] Bar-Itzhack, I. Y., Harman, R. R., and Choukroun, D., “State-Dependent Pseudo-Linear Filters for Spacecraft Attitude and Rate Estimation,” *AIAA Guidance, Navigation and Control Conference and Exhibit*, Paper number 2002–4461, Monterey, CA, 2002. <https://doi.org/10.2514/6.2002-4661>
- [134] Kim, I., Kim, J., and Kim, Y., “Angular Rate Estimator Using Disturbance Accommodation Technique,” *Proceedings of the AAS/AIAA Astrodynamics Specialist Conference*, AIAA Paper 2002–4829, Monterey, CA, 2002. <https://doi.org/10.2514/6.2002-4829>
- [135] Bar-Itzhack, I. Y., Harman, R. R., and Thienel, J. K., “A Feedback Approach to Spacecraft Angular Rate Estimation,” *AIAA Guidance, Navigation and Control Conference and Exhibit*, Paper number 2006–6807, Keystone, CO, 2006. <https://doi.org/10.2514/6.2006-6807>
- [136] Harman, R. R., “An Empirical Comparison Between Two Recursive Filters for Attitude and Rate Estimation of Spinning Spacecraft,” *AIAA Guidance, Navigation and Control Conference and Exhibit*, Paper number 2006–6158, Keystone, CO, 2006. <https://doi.org/10.2514/5.2006-6158>



- [137] Marschke, J. M., Crassidis, J. L. and Lam, Q. M., “Attitude Estimation Without Rate Gyros Using Generalized Multiple Model Adaptive Estimation,” *AIAA Guidance, Navigation and Control Conference*, Paper number 2009–5946, Chicago, IL, 2009. <https://doi.org/10.2514/6.2009-5946>
- [138] Mok, S.-H., Byeon, S. Y., Bang, H., and Choi, Y., “Attitude Dynamics Model-Based Gyroless Attitude Estimation for Agile Spacecraft,” *Proceedings of the IEEE 2018 Eighteenth International Conference on Control Automation and Systems (ICCAS 2018)*, PyeongChang, South Korea, 2018, pp. 1429–1434.
- [139] Chu, D., Glickman, J., and Harvie, E., “Improvements in ERBS Attitude Determination Without Gyros,” *Proceedings of the 1992 Flight Mechanics/Estimation Theory Symposium*, NASA - Goddard Space Flight Center, 1992, pp. 227–242.
- [140] Agrawal, B. and Palermo, W. J., “Angular Rate Estimation for Gyroless Satellite Attitude Control,” *AIAA Guidance, Navigation and Control Conference and Exhibit*, Paper number 2002–4463, Monterey, CA, 2002. <https://doi.org/10.2514/6.2002-4463>
- [141] Ivanov, D., Ovchinnikov, M., Roldugin, D., “Three-Axis Attitude Determination Using Magnetorquers,” *Journal of Guidance, Control and Dynamics*, Vol. 41, No. 11, 2018, pp. 2454–2461. <https://doi.org/10.2514/1.G003698>
- [142] Oshman, Y. and Dellus, F., “Fast Estimation of Spacecraft Angular Velocity from Sequential Geomagnetic Field Observations,” *Proceedings of the AAS/AIAA Astrodynamics Specialist Conference*, AIAA Paper number 2000–4242, Denver, CO, 2000. <https://doi.org/10.2514/6.2000-4242>
- [143] Oshman, Y. and Dellus, F., “Spacecraft Angular Velocity Estimation Using Sequential Observations of a Single Directional Vector,” *Journal of Spacecraft and Rockets*, Vol. 40, No. 2, 2003, pp. 237–247. <https://doi.org/10.2514/2.3938>
- [144] Psiaki, M. L. and Oshman, Y., “Spacecraft Attitude Rate Estimation from Geomagnetic Field Measurements,” *Proceedings of the AAS/AIAA Astrodynamics Specialist Conference*, AIAA Paper number 2002–4828, Monterey, CA, 2002. <https://doi.org/10.2514/6.2002-4828>
- [145] Cheon, Y.-J., “Spin-Axis Stabilization of Gyroless and Underactuated Rigid Spacecraft Using Modified Rodrigues Parameters,” *Proceedings of the SICE Annual Conference 2010*, Taipei, Taiwan, 2010, pp. 492–496.
- [146] Zhang, L., Zhang, S., and Qian, S., “Federated Nonlinear Predictive Filtering for the Gyroless Attitude Determination System with Multiple Sensors,” *IEEE 2011 International Workshop on Multi-Platform/Multi-Sensor Remote Sensing and Mapping*, Xiamen, China, 2011.

- [147] Hajiyeve, C., Çilden, D., and Somov, Y., “Gyroless Attitude and Rate Estimation of Small Satellites Using Singular Value Decomposition and Extended Kalman Filter,” *Proceedings of the IEEE 2015 Sixteenth International Carpathian Control Conference (ICCC)*, Szilvasvarad, Hungary, 2015.
- [148] Lippman, T., Kaufman, J. M., and Karpenko, M., “Autonomous Planning of Constrained Spacecraft Reorientation Maneuvers,” *Proceedings of the AAS/AIAA Astrodynamics Specialist Conference*, AAS Paper 17–676, Stevenson, WA, 2017.
- [149] Blackmore, L., Murray, E., Scharf, D.P., Aung, M., Bayard, D., Brugarolas, P., Hadaegh, F., Kang, B., Lee, A., Milman, M., and Sirlin, S., “Instrument Pointing Capabilities: Past, Present and Future,” *Proceedings of the Thirty-Fourth American Astronautical Society Guidance and Control Conference*, AAS Paper 11–091, Breckenridge, CO, 2011.
- [150] Pong, C. M., “On-Orbit Performance & Operation of the Attitude & Pointing Control Subsystems on ASTERIA,” *Thirty-Second Annual AIAA/USU Conference on Small Satellites*, Paper number SSC18-PI-34, Logan, UT, 2018.
- [151] Horowitz, I. M., *Synthesis of Feedback Systems*. Academic Press, NY, 1963.
- [152] Ross, I. M., Proulx, R. J., and Karpenko, M., “Unscented Optimal Control for Space Flight,” *Proceedings of the Twenty-Fourth International Symposium on Space Flight Dynamics (ISSFD)*, Laurel, MD, 2014.
- [153] Ross, I. M., Proulx, R. J., and Karpenko, M., “Unscented Guidance,” *Proceedings of the American Control Conference*, Chicago, IL, 2015, pp. 5605–5610.
- [154] Julier, S. J., Uhlmann, J. K., and Durrant-Whyte, H. F., “A New Approach for Filtering Nonlinear Systems,” *Proceedings of the American Control Conference*, Seattle, WA, 1995, pp.1628-1632.
- [155] Julier, S. J., “The Spherical Simplex Unscented Transformation,” *IEEE Proceedings of the American Control Conference*, Denver, CO, 2003, pp. 2430–2434.
- [156] Magallanes, L. C., and Karpenko, M., “Unscented Guidance for Zero-Feedback Reaction Wheel Slews,” *Proceedings of the Twenty-Ninth Annual AAS/AIAA Spaceflight Mechanics Meeting*, AAS Paper 19–207, Ka’anapali, Maui, HI, 2019.
- [157] Magallanes, L. C., and Karpenko, M., “Optimum Momentum Bias for Zero-Feedback Reaction Wheel Slews,” *Proceedings of the AAS/AIAA Astrodynamics Specialist Conference*, AAS Paper 19–741, Portland, ME, 2019.
- [158] Phelps, C., Gong, Q., Royset, J. O., Walton, C., and Kaminer, I., “Consistent Approximation of a Nonlinear Optimal Control Problem with Uncertain Parameters,” *Automatica*, Vol. 50, No. 12, 2014, pp. 2987–2997.

- [159] Zermelo, Ernst, “Über die Navigation in der Luft als Problem der Variationsrechnung 1930c,” in *Collected Works Vol. II Calculus of Variations, Applied Mathematics, and Physics*, H.-D. Ebbinghaus and A. Kanamori, Eds., Berlin Heidelberg, Germany: Springer-Verlag, 2013, pp. 672–721.
- [160] Kirk, D. E., *Optimal Control Theory An Introduction*. Dover Publications, Inc., NY, 1970.
- [161] Pinch, E., *Optimal Control and the Calculus of Variations*. Oxford University Press, 1993.
- [162] Shuster, M., “A Survey of Attitude Representations,” *Journal of the Astronautical Sciences*, Vol. 41, No. 4, 1993, pp. 439–517.
- [163] Longuski, J. M., and Prussing, J. E., *Optimal Control with Aerospace Applications*. Microcosm Press and Springer, NY, 2014.
- [164] Ross, I. M., *A Primer on Pontryagin’s Principle in Optimal Control*, Second Edition, Collegiate Publishers, San Francisco, CA, 2015.
- [165] Serres, U., “On Zermelo-Like Problems: Gauss-Bonnet Inequality and E. Hopf Theorem,” *Journal of Dynamical and Control Systems*, Vol. 15, No. 1, 2009, pp. 99–131.
- [166] Bryson, A. E., and Ho, Y. C., *Applied Optimal Control*. Hemisphere, NY, 1975.
- [167] Ross, I. M., “Enhancements to the DIDO<sup>®</sup> Optimal Control Toolbox,” arXiv, 20004.13112v2, June 2020. <https://arxiv.org/pdf/2004.13112.pdf>
- [168] Phelps, C., Royset, J. O., and Gong, Q., “Sample Average Approximations in Optimal Control of Uncertain Systems,” *Fifty-Second IEEE Conference on Decision and Control*, Florence, Italy, Dec. 2013.
- [169] Zabarankin, M., Uryasev, S. and Pardalos, P., “Optimal Risk Path Algorithms,” *Applied Optimization*, Vol. 66, 2002, pp. 273–296.
- [170] Washburn, A. R., and Kress, M., *Combat Modelling*. Springer, NY, 2009.
- [171] Charnes, A., and Cooper, W. W., “Chance-Constrained Programming,” *Management Science*, Vol. 6, No. 1, 1959, pp. 73–79.
- [172] Ross, I. M., Proulx, R. J., and Karpenko, M., “Unscented Optimal Control for Orbital and Proximity Operations in an Uncertain Environment: A New Zermelo Problem,” *AIAA Space and Astronautics Forum and Exposition: AAS/AIAA Astrodynamics Specialist Conference*, San Diego, CA, 2014.
- [173] Vinter, R. B., *Optimal Control*, Birkhauser, Boston, MA, 2000.

- [174] Ross, I. M., Proulx, R. J., Karpenko, M., and Gong, Q., “Reimann-Stieltjes Optimal Control Problems for Uncertain Dynamic Systems,” *Journal of Guidance, Control, and Dynamics*, Vol. 38, No. 7, 2015, pp. 1251–1263.
- [175] Ross, I. M., Proulx, R. J., and Karpenko, M., “A Lebesgue-Stieltjes Framework for Optimal Control and Allocation,” *Proceedings of the American Control Conference*, Chicago, IL, 2015, pp. 5599–5604.
- [176] Sidi, M., *Design of Robust Control Systems*, Krieger, Malabar, FL, 2001.
- [177] Trefethen, L. N., *Spectral methods in MATLAB*, SIAM, Philadelphia, PA, 2000.
- [178] Boyd, J., *Chebyshev and Fourier Spectral Methods*, Dover Publications, Inc., Mineola, NY, 2001.
- [179] Darlington, J., Pantelides, C. C., Rustem, B., and Tanyi, B. A., “Decreasing the Sensitivity of Open-Loop Optimal Solutions in Decision Making Under Uncertainty,” *European Journal of Operational Research*, Vol. 121, 2000, pp. 343–362.
- [180] Hover, F. S., and Triantafyllou, M.S., “Application of Polynomial Chaos in Stability and Control,” *Automatica*, Vol. 42, 2006, pp. 789–795.
- [181] Hover, F. S., “Gradient Dynamic Optimization with Legendre Chaos,” *Automatica*, Vol. 44, 2008, pp. 135–140.
- [182] Fisher, J., and Bhattacharya, R., “Optimal Trajectory Generation with Probabilistic System Uncertainty Using Polynomial Chaos,” *Journal of Dynamic Systems, Measurement and Control*, Vol. 133, 2011.
- [183] Schwartz, A., and Polak, E., “Consistent Approximations for Optimal Control Problems Based on Runge-Kutta Integration,” *Journal of Control and Optimization*, Vol. 34, No. 4, 1995, pp. 1235–1269.
- [184] Phelps, C., Gong, Q., Royset, J. O., and Kaminer, I., “Consistent Approximations of an Optimal Search Problem,” *Fifty-First IEEE Conference on Decision and Control*, Maui, Hawaii, USA, Dec. 2012.
- [185] Elnagar, G., Kazemi, M. A., and Razzaghi, M., “The Pseudospectral Legendre Method for Discretizing Optimal Control Problems,” *IEEE Transactions on Automatic Control*, Vol. 40, No. 10, 1995, pp. 1793–1796.
- [186] Gong, Q., Kang, W., Bedrossian, N. S., Fahroo, F., Sekhavat, P., and Bollino, K., “Pseudospectral Optimal Control for Military and Industrial Applications,” *Forty-Sixth IEEE Conference on Decision and Control*, New Orleans, LA, USA, Dec. 2007.

- [187] Ruths, J., and Li, J. S., “Optimal Control of Inhomogeneous Ensembles,” *IEEE Transactions on Automatic Control*, Vol. 57, No. 8, 2012, pp. 2021–2032.
- [188] Walton, C., *The Design and Implementation of Motion Planning Problems Given Parameter Uncertainty*, Ph.D. thesis, University of California Santa Cruz, Dec. 2015.
- [189] Walton, C., Phelps, C., Gong, Q., and Kaminer, I., “A Numerical Algorithm for Optimal Control of Systems with Parameter Uncertainty,” *Tenth IFAC Symposium on Nonlinear Control Systems NOLCOS 2016*, Vol. 49, No. 18, 2016, pp. 468–475. <https://doi.org/10.1016/j.ifacol.2016.10.209>
- [190] Walton, C. L., Gong, Q., Kaminer, I., and Royset, J., “Optimal Motion Planning for Searching for Uncertain Targets,” *Proceedings of the Nineteenth World Congress for the International Federation of Automatic Control*, Cape Town, South Africa, Aug. 2014.
- [191] Crassidis, J. L., Markley, F. L., and Cheng, Y., “Survey of Nonlinear Attitude Estimation Methods,” *Journal of Guidance, Control, and Dynamics*, Vol. 30, No. 1, 2007, pp. 12–28. <https://doi.org/10.2514/1.22452>
- [192] NASA. (2022). Monte Carlo Simulation. [https://www.nasa.gov/centers/ivv/jstar/monte\\_carlo.html](https://www.nasa.gov/centers/ivv/jstar/monte_carlo.html)
- [193] Meester, R., *A Natural Introduction to Probability Theory*, Second Edition, Birkhauser Verlag, Basel, Switzerland, 2008.
- [194] Kragelund, S., *Optimal Sensor-Based Motion Planning for Autonomous Vehicle Teams*, Ph.D. thesis, Naval Postgraduate School, Mar. 2017.
- [195] Ruths, J., and Li, J. S., “A Multidimensional Pseudospectral Method for Optimal Control of Quantum Ensembles,” *Journal of Chemical Physics*, Vol. 134, 2011, pp. 044128. <https://doi.org/10.1063/1.3541253>
- [196] Gill, P. E., Murray, W., and Saunders, M. A., “SNOPT: An SQP Algorithm for Large-Scale Constrained Optimization,” *SIAM Review*, Vol. 47, No. 1, 2005, pp. 99–131.
- [197] Cools, R., Mysovskikh, I. P., and Schmid, H. J., “Cubature Formulae and Orthogonal Polynomials,” *Journal of Computational and Applied Mathematics*, Vol. 127, 2001, pp. 121–152.
- [198] Julier, S. J., and Uhlmann, J. K., “A New Extension of the Kalman Filter to Nonlinear Systems,” *Signal Processing, Sensor Fusion, and Target Recognition VI*, Proceedings of SPIE, Vol. 3068, Jul. 1997. <https://doi.org/10.1117/12/280797>

- [199] Julier, S. J., and Uhlmann, J. K., “Reduced Sigma Point Filters for the Propagation of Means and Covariances Through Nonlinear Transformations,” *Proceedings of the American Control Conference*, Anchorage, AK, 2002, pp. 887–892.
- [200] Julier, S. J., and Uhlmann, J. K., “Unscented Filtering and Nonlinear Estimation,” *Proceedings of the IEEE*, Vol. 92, No. 3, 2004, pp. 401–422.
- [201] Crassidis, J., L., and Markley, F. L., “Unscented Filtering for Spacecraft Attitude Estimation,” *AIAA Guidance, Navigation and Control Conference and Exhibit*, Paper number 2003–5484, Austin, TX, 2003.
- [202] Hongmei, Z., and Zhenglong, D., “UKF-based Attitude Determination Method for Gyroless Satellite,” *IEEE Journal of Systems Engineering and Electronics*, Vol. 15, No. 2, 2004, pp. 105–109.
- [203] Julier, S. J., and Durrant-Whyte, H. F., “Process Models for the High-Speed Navigation of Road Vehicles,” *IEEE International Conference on Robotics and Automation*, Nagoya, Japan, 1995, pp. 101–105.
- [204] Julier, S. J., *Comprehensive Process Models for High-Speed Navigation*, Ph.D. thesis, University of Oxford, October 1997.
- [205] Uhlmann, J. K., *Dynamic Map Building and Localization for Autonomous Vehicles*, Ph.D. thesis, University of Oxford, 1995.
- [206] Julier, S. J., Uhlmann, J. K., and Durrant-Whyte, H. F., “A New Method for the Nonlinear Transformation of Means and Covariances in Filters and Estimators,” *IEEE Transactions on Automatic Control*, Vol. 45, No. 3, 2000, pp. 477–482.
- [207] Ross, I. M., Proulx, R. J., and Karpenko, M., “Unscented Control for Uncertain Dynamical Systems,” U.S. Patent US9727034 B1, issued Aug. 8, 2017.
- [208] Ross, I. M., Proulx, R. J., and Karpenko, M., “Monte Rey Methods for Unscented Optimization,” *AIAA SciTech Forum at the AIAA Guidance, Navigation and Control Conference*, Paper number 2016–0871, San Diego, CA, 2016.  
<https://doi.org/10.2514/6.2016-0871>
- [209] Ross, I. M., Karpenko, M., and Proulx, R. J., “Path Constraints in Tychastic and Unscented Optimal Control: Theory, Application and Experimental Results,” *Proceedings of the American Control Conference*, Boston, MA, 2016, pp. 2918–2923.
- [210] Karpenko, M., and Proulx, R. J., “Experimental Implementation of Riemann-Stieltjes Optimal Control for Agile CMG Maneuvering,” *Proceedings of the Twenty-Fifth Annual AAS/AIAA Spaceflight Mechanics Meeting*, AAS Paper 15–288, Williamsburg, VA, 2015.



- [211] Ross, I. M., Karpenko, M., and Proulx, R. J., “Method and Apparatus for State Space Trajectory Control of Uncertain Dynamical Systems,” U.S. Patent US9849785 B1, issued Dec. 26, 2017.
- [212] Dougherty, H., Tompetrini, K., Levinthal, J., and Nurre, G., “Space Telescope Pointing Control System,” *AIAA Guidance and Control Conference*, Paper number 80–1784, Danvers, MA, 1980.
- [213] Beals, G. A., Crum, R. C., Dougherty, H. J., Hegel, D. K., Kelley, J. L., and Rodden, J. J., “Hubble Space Telescope Precision Pointing Control System,” *AIAA Guidance, Navigation and Control Conference*, Paper number 86–1981, Williamsburg, VA, 1986.
- [214] Sharkey, J. P., Nurre, G. S., Beals, G. A., and Nelson, J. D., “A Chronology of the On-Orbit Pointing Control System Changes on the Hubble Space Telescope and Associated Pointing Improvements,” *AIAA Guidance, Navigation and Control Conference*, Paper number 92–4618, Hilton Head Island, SC, 1992.
- [215] Balas, M., Lee, Y. J., and Robertson, L., “Hubble, Bubble, Toil and Trouble,” *Proceedings of the Sixteenth Annual American Astronautical Society Guidance and Control Conference*, AAS Paper 93–006, Keystone, CO, 1993.
- [216] Collins, E., Jr., and Richter, S., “Linear-Quadratic-Gaussian-Based Controller Design for the Hubble Space Telescope,” *Journal of Guidance, Control, and Dynamics*, Vol. 18, No. 2, 1995, pp. 208–213.
- [217] Irwin, D., Lawrence, D. and Glen, R., “H-Infinity Control Design Specifications Applied to the HST,” *Proceedings of the Sixteenth Annual American Astronautical Society Guidance and Control Conference*, AAS Paper 93–003, Keystone, CO, 1993.
- [218] Zhu, G., Grigoriadis, K. M., and Skelton, R. E., “Covariance Control Design for Hubble Space Telescope,” *Journal of Guidance, Control and Dynamics*, Vol. 18, No. 2, 1995, pp. 230–236.
- [219] Addington, S. I., and Johnson, C. D., “Dual-Mode Disturbance-Accommodating Pointing Controller for Hubble Space Telescope,” *Journal of Guidance, Control and Dynamics*, Vol. 18, No. 2, 1995, pp. 200–207.
- [220] Markley, F. L., and Nelson, J. D., “Zero-Gyro Safemode Controller for the Hubble Space Telescope,” *Journal of Guidance, Control, and Dynamics*, Vol. 17, No. 4, 1994, pp. 815–822.
- [221] Bukley, A. P., “Hubble Space Telescope Pointing Control System Design Improvement Study Results,” *Journal of Guidance, Control, and Dynamics*, Vol. 18, No. 2, 1995, pp. 194–199.

- [222] Prior, M., and Dunham, L., “System Design and Performance of the Two-Gyro Science Mode for the Hubble Space Telescope,” *Acta Astronautica*, Vol. 61, 2007, pp. 1010–1018.
- [223] Halverson, J., Hsu, O., Calhoun, P., and Tedla, Y., “Performance Improvements for the Lunar Reconnaissance Orbiter Gyroless Extended Kalman Filter,” *AAS/AIAA Astrodynamics Specialist Conference*, AAS Paper 19–615, Portland, ME, 2019.
- [224] Lefferts, E. J., Markley, F. L., and Shuster, M. D., “Kalman Filtering for Spacecraft Attitude Estimation,” *Journal of Guidance, Control, and Dynamics*, Vol. 5, No. 5, 1982, pp. 417–429.
- [225] Wie, B., *Space Vehicle Dynamics and Control*, AIAA, Reston, VA, 1998.
- [226] Schaub, H., and Junkins, J. L., *Analytical Mechanics of Space Systems*, 2<sup>nd</sup> ed., AIAA, Reston, VA, 2009.
- [227] Karpenko, M., King, J. T., Dennehy, C. J., and Ross, I. M., “Agility Analysis of the James Webb Space Telescope,” *Journal of Guidance, Control, and Dynamics*, Vol. 42, No. 4, 2019, pp. 810–821. <https://doi.org/10.2514/1.G003816>
- [228] Ross, I. M., and Karpenko, M., “A Review of Pseudospectral Optimal Control: From Theory to Flight,” *Annual Reviews in Control*, Vol. 36, No. 2, 2012, pp. 182–197.



THIS PAGE INTENTIONALLY LEFT BLANK

## INITIAL DISTRIBUTION LIST

1. Defense Technical Information Center  
Ft. Belvoir, Virginia
2. Dudley Knox Library  
Naval Postgraduate School  
Monterey, California



## DUDLEY KNOX LIBRARY

NAVAL POSTGRADUATE SCHOOL

[WWW.NPS.EDU](http://WWW.NPS.EDU)

---

WHERE SCIENCE MEETS THE ART OF WARFARE